4 Influence of Composition on the Electric Field-Induced Properties

4.1 Introduction

The aim of this chapter is to elucidate the field- and composition-dependent behavior of BNT-based piezoceramics. In BNT-6BT-100yKNN, a peculiarly high field-induced strain is observed for small KNN contents. In order to identify the underlying physical mechanism, the KNN content y is varied from 0.01 to 0.18. A small y yields typical ferroelectric-like characteristics but the field-dependent behavior is notably altered for $y \geq 0.03$ as the remanent strain and polarization are largely decreased. In addition, sizable piezoelectric activity is obtained only under high electric fields. It is hypothesized that these effects are associated with an enhanced disorder rather than the chemical properties of the endmember KNN. In order to prove this assumption, the constitutive large- and small-signal behavior of the novel BNT-100xBKT-100yBZT material system is studied as a function of BZT content. Despite different chemistry, it is found that BNT-BKT-BZT shows remarkable similarity with the model system BNT-6BT-100yKNN. Therefore, the effect of large strain and low remanence is indeed a generally observable feature in this class of BNT-based piezoceramics. It will be shown by means of additional structural and microstructural investigations that a field-induced phase transition from a RF to a FE phase may take place at large enough electric fields. The stability of this induced phase, however, depends on the concentration of the ternary endmember y.

4.2 Experimental Methodology

4.2.1 Powder Processing and Sample Preparation

The first step in producing ceramic specimens was the fabrication of a powder of given stoichiometry. From the powder, a dense and solid sample is made by shaping and subsequent sintering at high temperatures.

The ceramic powders were made by means of a mixed oxide route using reagent grade oxides and carbonates of the respective elements. The raw powders (all Alfa Aesar GmbH, Karlsruhe, Germany) Bi_2O_3 (99.975 % purity), Na_2CO_3 (99.5 %), $BaCO_3$ (99.8 %), K_2CO_3 (99.0 %), ZnO_2 (99.99 %), Nb_2O_5 (99.9 %), and TiO_2 (99.9 %) were weighed according to the respective stoichiometric formula using a precision balance (TE214S, Sartorius AG, Göttingen, Germany). The first material system analyzed in this work is (1-y)(0.94$Bi_{1/2}Na_{1/2}TiO_3$–0.06$BaTiO_3$)–$y$$K_{1/2}Na_{1/2}NbO_{1/2}$, referred to as BNT-6BT-100yKNN, with y={0; 0.01; 0.02; 0.03; 0.09; 0.12; 0.15; 0.18}. The second material system is (1-y)[(1-x)$Bi_{1/2}Na_{1/2}TiO_3$–$x$$Bi_{1/2}K_{1/2}TiO_3$]–

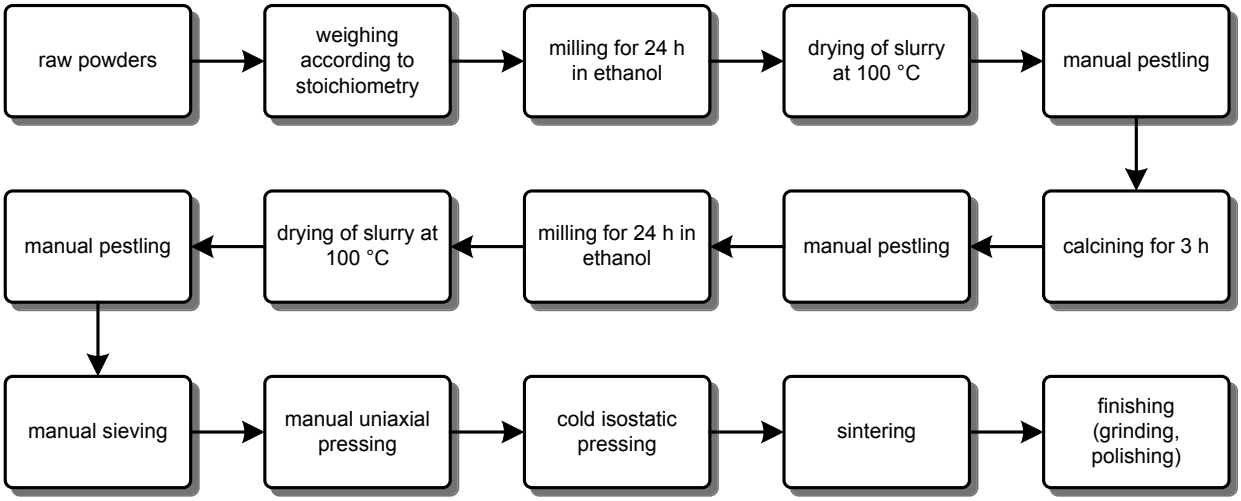

Figure 4.1: Schematic of the complete powder processing route including shaping of samples.

yBiZn$_{1/2}$Ti$_{1/2}$O$_3$, referred to as BNT-100xBKT-100yBZT, with x={0.19; 0.20}and y={0; 0.02; 0.03; 0.04; 0.06}. Subsequent mixing was performed in a planetary mill (Pulverisette 5, Fritsch GmbH, Idar-Oberstein, Germany) with custom-made polyamide containers and zirconia milling balls (Mühlheimer GmbH, Bärnau, Germany). The milling was done 24 h at 250 min^{-1} using ethanol as a milling medium. In the next step, the slurries were dried in an oven (Memmert GmbH + Co. KG, Schwabach, Germany) at 100 °C. After subsequent pestling the powders were calcined in covered alumina crucibles (Morgan Technical Ceramics W. HALDENWANGER Technische Keramik GmbH & Co. KG, Waldkraiburg, Germany) using a box furnace (L9/KM, Nabertherm GmbH, Lilienthal, Germany) with a dwell time of 3 h at temperatures between 800 °C and 900 °C. After another milling and drying step, the powders were manually sieved through a polymer sieve (LINKER Industrie-Technik GmbH, Kassel, Germany) with a mesh size of 160 µm. A schematic of the complete powder processing and shaping route is provided by Figure 4.1.

The approximate sample shape was produced by manually pressing the processed powder in a custom-made steel die. The majority of the testing was conducted on disc-shaped samples made from a die with an inner diameter of 10 mm. Bar-type samples for neutron diffraction and elastic measurements were shaped by a die with a 4x40 mm^2 cavity. In the next step, the samples were put into a rubber sheath that was subsequently evacuated with a water jet pump. The sheaths were tied with a string and compacted at 300 MPa in a cold isostatic press (KIP 100E, Paul-Otto Weber GmbH, Remshalden, Germany) filled with hydraulic oil. Finally, the samples were sintered in covered alumina crucibles for 3 h at temperatures from 1100 °C to 1150 °C using a box furnace (L16/14, Nabertherm GmbH, Lilienthal, Germany). In order to minimize the evaporation of volatile elements, the samples were partially covered in powder of the respective composition. By subsequent grinding with grinding discs of the grit sizes 220, 600 and 1200 (MD Piano, STRUERS GmbH, Willich, Germany) the sample geometry was adjusted and a surface layer of at least 200 µm was removed. Bar-type samples were machined to a cross section of approximately 3x3 mm^2, while disc-shaped samples for PFM experiments were ground down to a thickness of approximately 250 µm. The cylindrical specimens for mechanical testing under uniaxial

pressure were ground and lapped to 6 mm height and the cylindrical periphery was adjusted to a diameter of 5.9 mm by means of round grinding (WEILER Werkzeugmaschinen GmbH, Emskirchen/Mausdorf, Germany). For electrical measurements the surface finish was conducted by fine grinding with silicon carbide abrasive paper that had a grit size of 4000 (STRUERS GmbH, Willich, Germany). Samples for microscopy experiments were polished to mirror finish quality on a semi-automatic polishing machine (Phoenix 4000, Jean-Wirtz GmbH & Co. KG, Düsseldorf, Germany) using diamond paste with an abrasive particle size of 15 µm, 6 µm, 3 µm, 1 µm and 0.25 µm (DP Paste, STRUERS GmbH, Willich, Germany) on polishing cloth (DP-DUR, STRUERS GmbH, Willich, Germany). The finishing was done in a last polishing step of 15 min with a colloidal silica polishing suspension (Buehler Mastermet, Buehler GmbH, Düsseldorf, Germany).

For the majority of the electrical measurements, electrodes were applied on both faces by silver paint (Gwent Electronic Materials Ltd, Pontypool, UK) with subsequent burn-in at 400 °C for 2 h. This treatment further minimized internal stresses stemming from prior machining. PFM samples were electroded on only one side, while samples for diffraction measurements received no electrode but were annealed at 400 °C to release mechanically induced residual stress. For high-energy *in situ* XRD studies bars of 1x1x7 mm^3 size were cut from electroded pellets by a precision wire saw (model 4240, well Diamantdrahtsägen GmbH, Mannheim, Germany) with subsequent annealing at 400 °C for 30 min.

4.2.2 Electrical Large-Signal Measurements

The large-signal parameters strain and polarization are the two most fundamental values in the description of the electromechanical properties under high electric fields.

The principle setup for the electrical measurements under high electric fields was based on the Sawyer-Tower circuit illustrated by Figure 4.2. A signal generator (Agilent 33220A, Agilent Technologies Deutschland GmbH, Böblingen, Germany) supplied a signal with the desired polarity, frequency, and amplitude to a voltage source (20/20C, TREK, Inc., Medina, NY, USA). The waveform was triangular to allow for a constant rate of field change dE/dt, which is especially important for frequency-dependent measurements. The field-induced polarization change P of the sample can be measured by determining the change of charge Q. To do so, a measurement capacitor C_m was connected in series with the sample, represented by an ideal capacitor C_s in Figure 4.2. For such a serial connection of capacitors $Q = Q_s = Q_m$. Since charge and capacitance are interrelated via the voltage U according to $Q = C \cdot U$, the charge of the sample capacitor is accessible by measurement of the voltage drop U_m across the known capacitance C_m. Knowing the electroded area A of the sample, the polarization was calculated according to the following equation.

$$P = \frac{C_m \cdot U_m}{A} \tag{4.1}$$

With a sample capacitance well below 10 nF, the measurement capacitance was in the range between 10 µF and 15 µF. Therefore, by choosing $C_m \gg C_s$, the voltage drop across the measurement

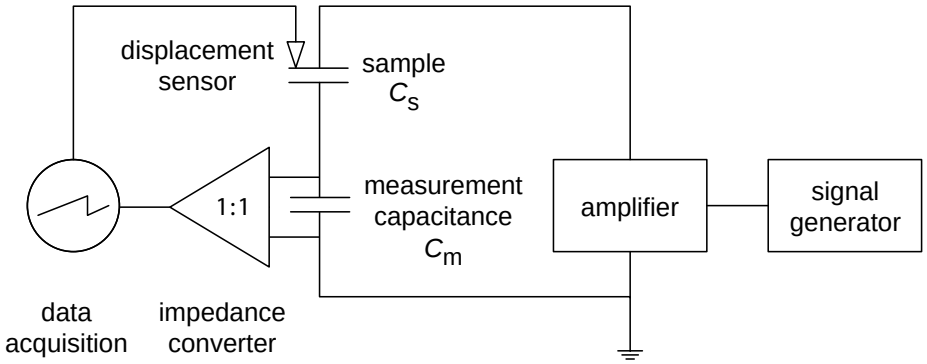

Figure 4.2: Schematic of the Sawyer-Tower setup for the measurement of large-signal parameters $P(E)$ and $S(E)$.

capacitor was negligible and the majority of the voltage dropped across the sample. An operational amplifier was connected as presented in Figure 4.2 to increase the input resistance of the data acquisition device, a four-channel oscilloscope (DSO6014A, Agilent Technologies, Santa Clara, USA) and to protect the electrical measurement equipment in case of an electrical breakdown. All disc-shaped samples had a thickness to diameter ratio equal to or less than 1:10 in order to minimize edge effects of the electric field.

The sample was submerged in a polytetrafluoroethylene (PTFE) container, which was filled with silicone oil (AK35 or AK200, Wacker Chemie GmbH, Munich, Germany) to allow for the application of electric fields up to 12 $kV \cdot mm^{-1}$. Electric contact was established by a bottom and a top point contact.

Strain S was measured simultaneously with an optical sensor (D63, Philtec, Inc., Annapolis, MD, USA) that monitored the displacement by detecting the intensity of reflected light. The reflection of the light, which was fed in through a glass fiber, took place at the flat and polished metal top face of the upper point contact as presented in Figure 4.3. Vertical translation of the upper electrode was enabled by a special bearing using a bow spring. This setup allowed for a precise measurement of the sample strain for frequencies up to several hundred Hz. The amplification electronics were the limiting factor for higher frequencies. At 100 Hz, the resolution of the optical sensor is given with 4 nm, while typical maximum displacements were in the µm-range.

4.2.3 Electrical Small-Signal Measurements as a Function of Bias Field

The piezoelectric coefficient d_{33} and the permittivity $\varepsilon_{r,33}$ describe the material's behavior under small excitation fields. Both are useful parameters in the discussion of the polarization state and domain processes, which are naturally influenced by a superimposed bias electric field.

The relative permittivity $\varepsilon_{r,33}$ and piezoelectric coefficient d_{33} have been measured as a function of bias field by superimposing a small AC signal to a large-signal waveform. Two setups were available for this measurement: first, a custom-made setup and, second, a commercially available

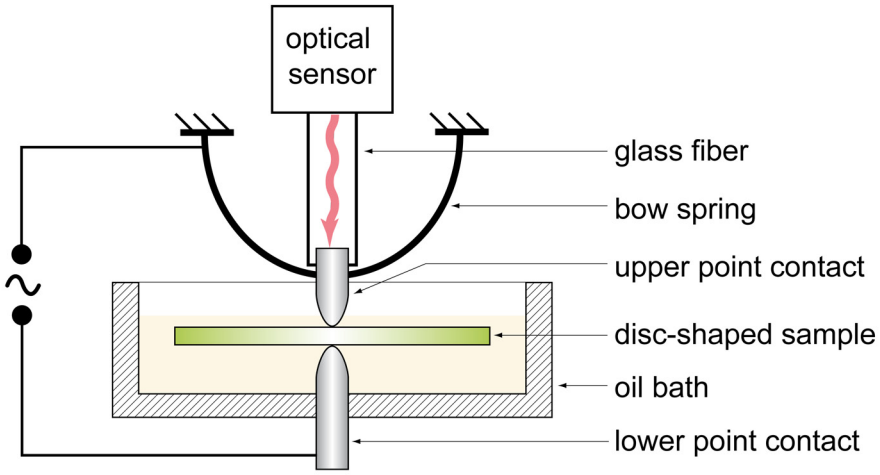

Figure 4.3: Schematic on the optical measurement of field-induced strain $S(E)$.

system. The latter has the advantage of faster data acquisition, while the former simultaneously records also strain and polarization.

The first measuring setup employed the above-mentioned optical sensor (Figure 4.4) and a LabVIEW (National Instruments Germany GmbH, Munich, Germany) program by Nina Balke. A step-like large-signal waveform was supplied to an amplifier (20/20C, TREK, Inc., Medina, NY, USA) by means of an analog-digital-converter (PCI-6221, National Instruments Corporation, Austin, TX, USA). The step time was 5.5 s with an incremental increase of 100 V_{DC} per step to a maximum of up to 4 kV, resulting in an equivalent frequency of approximately 1 mHz. A first lock-in amplifier (SR830, Scientific Instruments, West Palm Beach, FL, USA) was used to generate the sinusoidal AC small-signal with a frequency of 1 kHz and an amplitude of 7.07 V (5 V_{rms}). A mixing unit combined both waveforms, which were then supplied to the sample, as shown in Figure 4.4. The strain and polarization response were analyzed by the two lock-in amplifiers with the AC outgoing signal of the first lock-in amplifier being the reference signal. The relative permittivity $\varepsilon_{r,33}$ could be determined from the field-dependent change of polarization according to the following equation, assuming $\chi \approx \varepsilon$

$$\frac{\Delta P_3}{\Delta E_3} = \varepsilon_{33} = \varepsilon_0 \cdot \varepsilon_{r,33}. \tag{4.2}$$

The inverse piezoelectric coefficient was calculated accordingly from the change of strain

$$\frac{\Delta S_3}{\Delta E_3} = d_{33}. \tag{4.3}$$

This setup was used to characterize samples of the compositions BNT-6BT-100yKNN with y={0; 0.01; 0.03; 0.09; 0.18}.

The second setup was the commercially available aixPES system (aixACCT Systems GmbH, Aachen, Germany). The basic concept of measuring the small-signal parameters $d_{33}(E)$ and $\varepsilon_{33}(E)$ was the same as in the custom-built apparatus, *i.e.*, superimposing a sinusoidal AC small-signal to a large-signal. Here, the large-signal was a triangular waveform with a frequency of

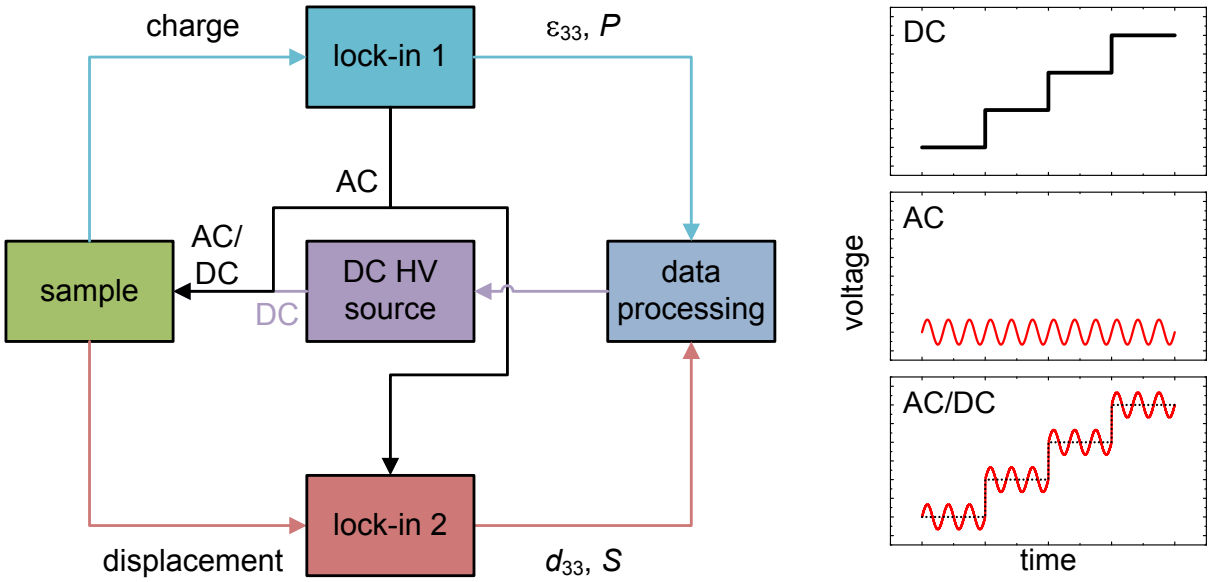

Figure 4.4: Schematic of the custom-built setup for the measurement of $d_{33}(E)$, $\varepsilon_{33}(E)$, $S(E)$, and $P(E)$ by means of an optical sensor and two lock-in amplifiers.

50 mHz modulated by a small-signal of 1 kHz with an amplitude of 10 V. Polarization was assessed by means of the virtual ground method, employing an operational amplifier with a feedback resistor. Strain was measured interferometrically with a He-Ne-Laser of 633 nm wavelength, offering a maximum resolution of approximately 1.2 nm. A mirror was in contact with the sample surface via a membrane spring. This spring contacted the upper electrode and allowed a free displacement of the sample and the measurement thereof by providing the reflectivity that was required for interferometry. This commercial setup was used to characterize samples of the BNT-20BKT-100yBZT material system with y={0; 0.02; 0.04; 0.06}.

4.2.4 *In situ* X-Ray Diffraction as a Function of Electric Field

In situ *X-ray diffraction (XRD) is a powerful technique that allows the tracking of structural changes upon application of an electric field.*

The experiments for the high-energy *in situ* XRD studies under electric field were conducted at beamline ID15B at the European Synchrotron Radiation Facility (ESRF, Grenoble, France). A monochromatic beam of 87.2 keV was obtained through a silicon bent Laue monochromator. Due to the high beam energy and the accordingly short wavelength of λ=0.0142 nm the measurement could be performed in transmission geometry as presented in Figure 4.5. This geometry allowed collection of diffraction patterns that represent both surface and bulk contribution. The beam was focused to approximately 45x45 mm^2 by means of reflective lenses. The Debye-Scherrer diffraction cones were detected by a Pixium 4700 area detector (Thales Group, Neuilly-sur-Seine, France) with an active area of 381.9x294.1 mm^2.[177] This two-dimensional diffraction image was split into 36 sections, each covering an angular range of ξ=10 °. Subsequent radial integration via the fit2D software (by A. Hammersley, ESRF, Grenoble, France) yielded 36 one-dimensional in-

tensity versus 2θ plots. This procedure enabled texture measurements by detecting the diffracted beam at different angles with respect to the electric field vector. The electric field was applied perpendicular to the X-ray beam in incremental steps with a step size of 0.46 $kV \cdot mm^{-1}$ and a step length of 22 s up to a maximum field of 6 $kV \cdot mm^{-1}$. Then the electric field was accordingly reduced to zero again. The experiments were conducted by Wook Jo and John E. Daniels (ESRF at that time). The studied compositions were BNT-20BKT-100yBZT, with y={0; 0.02; 0.04; 0.06}.

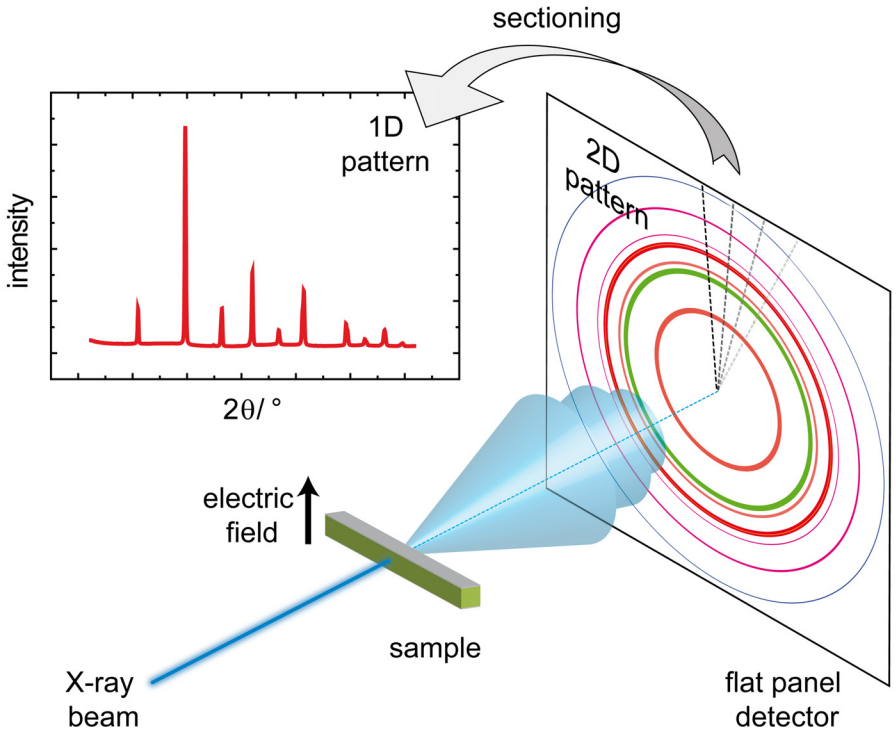

Figure 4.5: Schematic experimental setup for high-energy *in situ* XRD measurements as a function of electric field at beamline ID15B (ESRF). Note that the delineated Laue cones are shortened for the sake of clarity.

4.2.5 Piezoresponse Force Microscopy

It is well known that the domain structure determines the electromechanical properties of ferroelectrics.[178] *An effective means to image and probe the microstructure is piezoresponse force microscopy (PFM).*

PFM studies were conducted at the Functional Imaging on the Nanoscale group at the Center for Nanophase Materials Sciences (CNMS) within the Oak Ridge National Laboratory (ORNL, Oak Ridge, TN, USA) in collaboration with Dr. Sergei Kalinin and Dr. Nina Balke. PFM is a Scanning Probe Microscopy (SPM) technique derived from Atomic Force Microscopy (AFM). In AFM, a sharp tip is utilized to scan a sample surface in order to obtain information on the topography. When the tip is in contact mode, a laser in combination with a photodiode monitors the tip deflection as illustrated in Figure 4.6. Keeping the tip deflection constant via a feedback

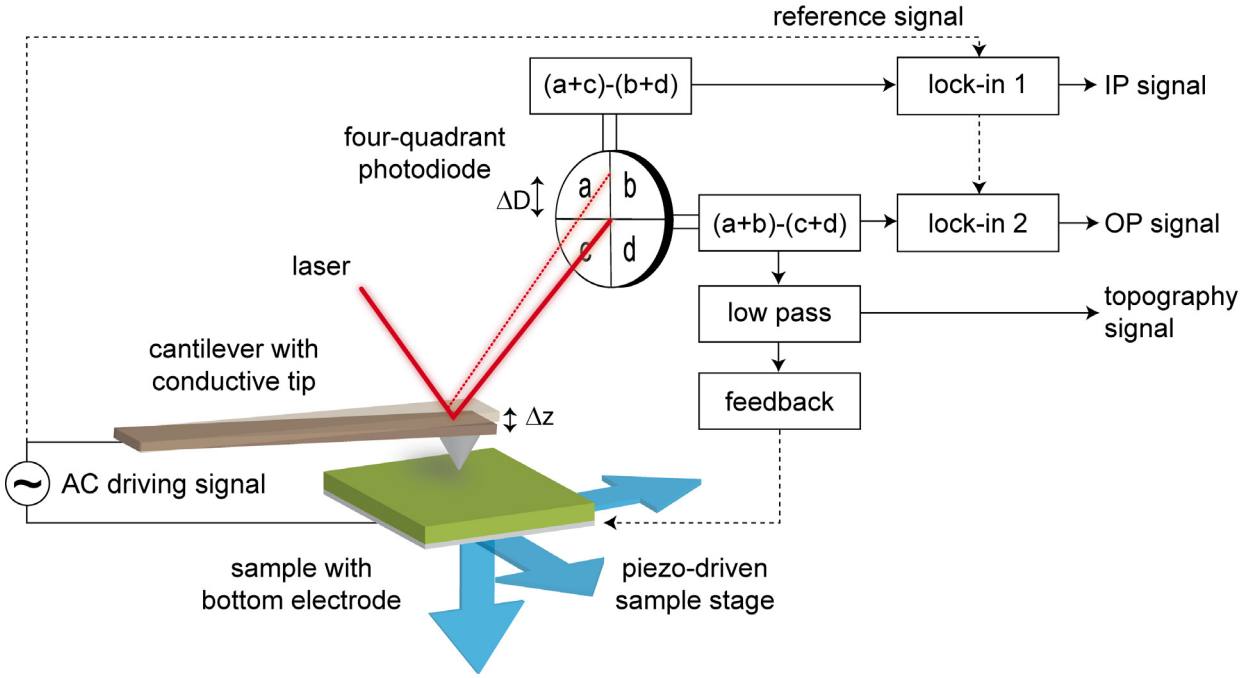

Figure 4.6: Operational principle in piezoresponse force microscopy (after Ref.[179]).

loop allows for the imaging of the topography. Other than conventional AFM, PFM additionally affords the assessment of electrical and electromechanical properties on the nanoscale.

All PFM studies within this work were conducted on two commercially available microscopes, namely MFP-3D™ and a Cypher™ AFM (both Asylum Research, Santa Barbara, California, USA). The measurements were performed by scanning the surface of a sample with a sharp tip that was coated with Pt/Ir and thus was conductive (Nanosensors™, Neuchâtel, Switzerland). As the sample was grounded via a bottom electrode, the tip acted as a moving top electrode. Due to the converse piezoelectric effect, the application of an electrical signal caused an oscillation of the sample. This oscillation could be detected with the aforementioned arrangement of laser and photodiode. As illustrated in Figure 4.6, the vertical displacement of the tip as consequence of grain deformation is referred to as out-of-plane (OP) PFM signal. By contrast, a shear deformation will contribute to a torsional movement of the cantilever mediated via frictional forces, which is termed in-plane (IP) signal.

In single-frequency PFM, the excitation signal was sinusoidal with a frequency slightly below the resonance frequency f_R of the contacted tip, typically at around f_R=300 kHz for OP and f_R=750 kHz for IP measurements. Lock-in amplification enabled the extraction of the minute signal of the periodic displacement from the overall response, yielding the amplitude A and phase shift ϕ of the oscillation. The latter one was determined from the orientation of the respective polarization vector with respect to the applied electric field, shown in Figure 4.7. Using both A and ϕ, it is possible to image and characterize the domain structure.

As f_R may shift considerably depending on the topography, single-frequency PFM is prone to topography cross-talk. Therefore this technique was used in this work merely for fast overview

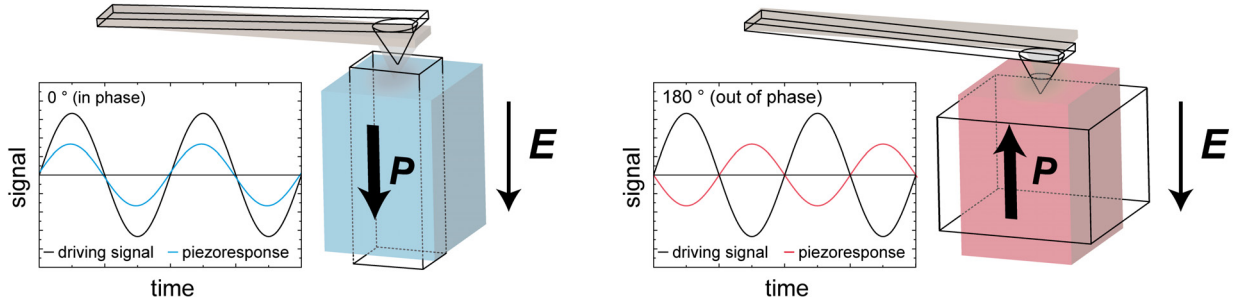

Figure 4.7: In-phase (left) and out-of-phase (right) piezoresponse signals. Monitoring the phase ϕ enables the discrimination of domains with a distinct orientation of polarization; the wireframe drawing denotes the response to the applied field.

measurements and long-time measurements that required fast, repetitive scanning. The rest of the measurements employed the band excitation (BE) method.[180] Instead of using one single frequency, the excitation signal contained a band of frequencies encompassing the resonance frequency. The predefined signal was converted to the time domain by inverse fast Fourier transform (iFFT), yielding a complex waveform that was used for the excitation of the cantilever. Then, the resulting response was recorded and processed by means of FFT for each point of the image. Both excitation and response amplitude are exemplified in Figure 4.8 for single frequency PFM as well as BE PFM.

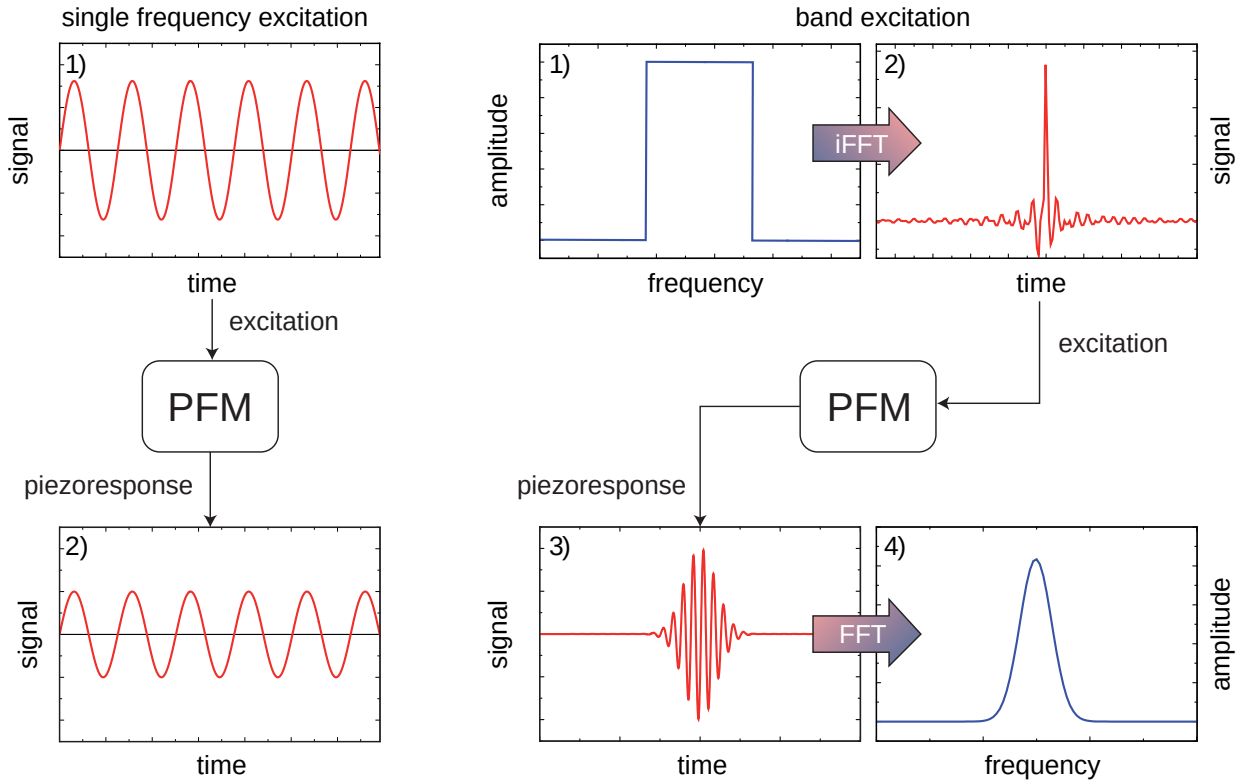

Figure 4.8: Schematic comparison of excitation and piezoresponse signal for single-frequency PFM (left) and BE PFM (right).

Amplitude A_0 at resonance frequency f_R, phase ϕ, and quality factor Q can be calculated by fitting the response to the single harmonic oscillator (SHO) model, using the following equations.

$$A(f) = \frac{A^{max} \cdot f_R^2}{\sqrt{\left(f^2 - f_R^2\right)^2 + \left(f \cdot f_R \cdot Q^{-1}\right)^2}} \tag{4.4}$$

$$tan(\phi(f)) = \frac{f \cdot f_R \cdot Q^{-1}}{f^2 - f_R^2} \tag{4.5}$$

A third excitation mode is the Dual AC Resonance Tracking (DART) technique of the Asylum Cypher™ PFM.[181] Here, the excitation signal comprises two frequencies, one slightly below and one slightly above the resonance frequency. Using two frequencies enabled the tracking of changes in resonance frequency, *e.g.*, due to topography cross-talk.

The PFM study was conducted on samples of the pseudoternary material system BNT-6BT-100yKNN with y={0; 0.01; 0.03; 0.09; 0.18}. At first, the initial, virgin domain morphology of all five compositions was imaged using DART in the in-plane as well as the out-of-plane mode of the Cypher PFM with 3 V_{AC}. Moreover, poling experiments were performed by applying a DC bias voltage to the tip. In the first step, an unbiased 5x5 µm^2 area was scanned by means of the BE technique with 2 V_{AC} and the OP signal was recorded. Then, a 3x3 µm^2 area was poled by using a DC bias of -10 V. This procedure was repeated with a positive bias of the same amplitude for a 1x1 µm^2 area within the previously poled region, in order to check for reversibility. Then the initial 5x5 µm^2 square was measured again, encompassing the two inversely poled areas. This overall procedure was then repeated for $\mp$20 V in the same area.[1] In order to examine the stability of the poled domains for x={0; 0.01; 0.03}, a 1x1 µm^2 square was poled with -20 V_{DC}. Then the according 3x3 µm^2 area was successively scanned for at least 66 min using the single-frequency OP PFM technique.

Microscopic piezoelectric response loops were measured in a grid of 10x10 points spanned across a 5x5 µm^2 square for y={0; 0.01; 0.03; 0.09; 0.18}. The maximum amplitude was set as low as possible but as high as necessary to induce switching. The individual loops were averaged, yielding loops that are representative for the microscopic switching behavior of the respective material. A custom-made software by CNMS was used to determine characteristic values like switching voltage and switchable polarization. For x={0; 0.01; 0.03} additional voltage spectroscopy measurements were conducted in a dense 70x70 grid spanned across a 5x5 µm^2 square. Owing to the high required switching voltages for y=0.09 and y=0.18 and the associated reduced lifetime of the tip, no such high-density mapping could be applied to these two compositions.

[1] The '$\mp$' symbol indicates that the negative electric field was applied first.

4.3 Experimental Results

4.3.1 Large-Signal Constitutive Behavior

Large-Signal Constitutive Behavior of BNT-6BT-100yKNN

The large-signal properties of BNT-6BT-100yKNN depend significantly on KNN content, allowing the distinction into two groups of compositions: i) compositions with remanent strain and polarization and ii) compositions without.

Figure 4.9 summarizes the key parameters derived from the measurement of $P(E)$ and $S(E)$ loops used throughout this work.

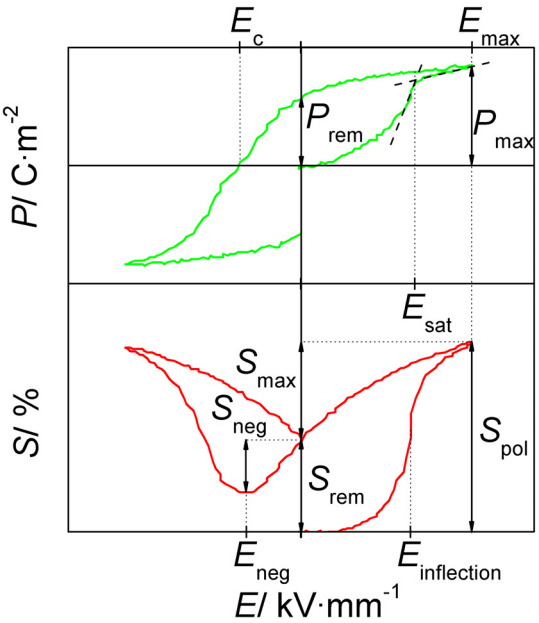

Figure 4.9: Characteristic parameters obtained from large-signal measurements: coercive electric field E_c, maximum electric field E_{max}, saturation electric field E_{sat}, electric field of negative strain E_{neg}, electric field of $S(E)$ inflection $E_{inflection}$, maximum polarization P_{max}, remanent polarization P_{rem}, poling strain S_{pol}, maximum strain S_{max}, remanent strain S_{rem}, and negative strain S_{neg}.

The large-signal polarization and strain hystereses for BNT-6BT-100yKNN are shown in Figure 4.10 for an applied maximum field of 6 kV·mm^{-1} at 1 mHz. For y=0, which is the base composition without KNN, the $P(E)$ loop resembles a ferroelectric hysteresis with a high P_{max} of 0.59 C·m^{-2} and a likewise high P_{rem} of 0.48 C·m^{-2}. The coercive field E_c, which is within this work determined from the x-intercept of the $P(E)$ curve, is 2.2 kV·mm^{-1}. The corresponding $S(E)$ loop features a butterfly shape with a poling strain S_{pol} of 0.53 %, a remanent strain S_{rem} of 0.38 %, and a negative strain S_{neg} of 0.1 %. Due to the sizable remanent strain, S_{max} obtainable during unipolar cycling is comparably small. Consequently, the normalized strain, which is defined as

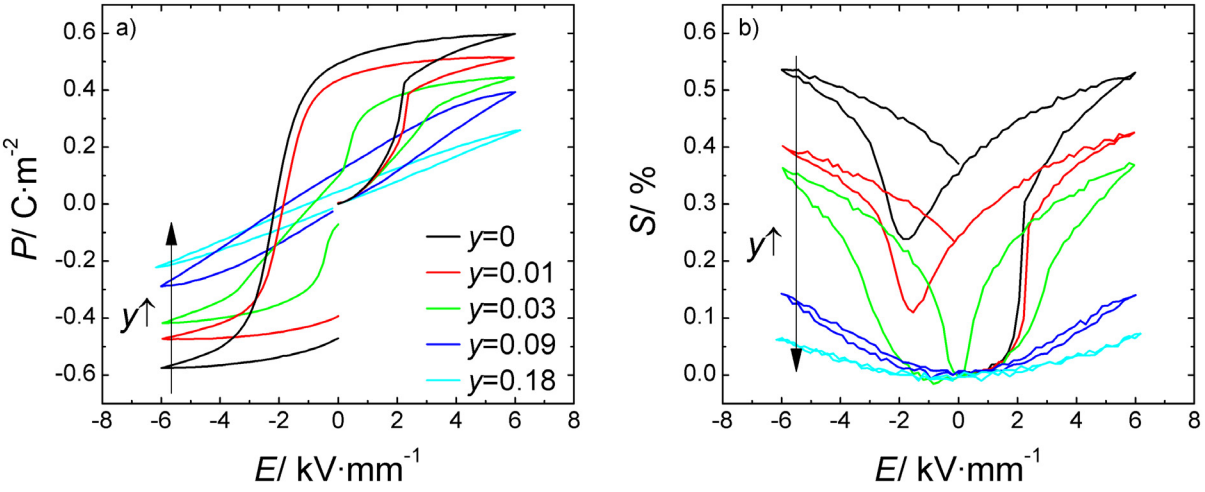

Figure 4.10: Field-induced a) polarization and b) strain for BNT-6BT-100yKNN with y={0; 0.01; 0.03; 0.09; 0.18}.

the ratio of S_{max} over E_{max} and sometimes also termed d^*_{33}, has a small value of 259 pm·V^{-1} at 6 kV·mm^{-1}. With the incorporation of KNN the electromechanical behavior is significantly altered.

For small KNN contents, *e.g.*, for y=0.01, the maximum and remanent values of both polarization and strain are diminished, as shown in Figure 4.11. While E_c decreases to 2 kV·mm^{-1}, $S_{max}{\cdot}E^{-1}_{max}$ increases to 340 pm·V^{-1}. This is because the decrease in S_{rem} overcompensates the decrease of S_{max}. The ferroelectric character of the $P(E)$ and $S(E)$ loops gradually vanishes for higher values of y. For y=0.03 the polarization hysteresis exhibits a pinched shape with the polarization sharply dropping when the value of the electric field approaches zero, yielding a P_{rem} of 0.08 C·m^{-2}. At the same time, the $S(E)$ curve no longer exhibits a butterfly shape as no negative strain is observed. Even though S_{pol} decreases, $S_{max}{\cdot}E^{-1}_{max}$ increases to 611 pm·V^{-1} due to virtually zero S_{rem}. Any further addition of KNN results in a slimming of the $P(E)$ curve. The slimming of the $P(E)$ loop is associated with a drop in the polarization loss density e_{loss}, which is a measure for the dissipated energy during each cycle and is determined from the integral area of the second $P(E)$ loop. For y=0 the polarization loss density is 4.8 MJ·m^{-3}. The modification with KNN results in a decrease to 3.9 MJ·m^{-3}, 1.6 MJ·m^{-3}, 0.9 MJ·m^{-3}, and eventually 0.4 MJ·m^{-3} for a y of 0.01, 0.03, 0.09, and 0.18 respectively. At the same time, P_{max}, P_{rem}, and E_c decline. Note that, strictly speaking, a coercive field may only be determined for saturated $P(E)$ loops. This is clearly not the case for high values of y, however, the term E_c is used to afford a comparison of the electric field, where P becomes zero.

A striking feature of the $P(E)$ loops for y={0; 0.01; 0.03} is the observation of a distinct electric field where the slope changes abruptly during the first half-cycle. This field, referred to as E_{sat}, marks the threshold between a progressive and a regressive curve progression, *i.e.*, beyond E_{sat} the slope gradually decreased with increasing field. For the base composition E_{sat} is 2.23 kV·mm^{-1}, increasing to 2.37 kV·mm^{-1} for y=0.01 and to 3.3 kV·mm^{-1} for y=0.03. Interestingly, this increase

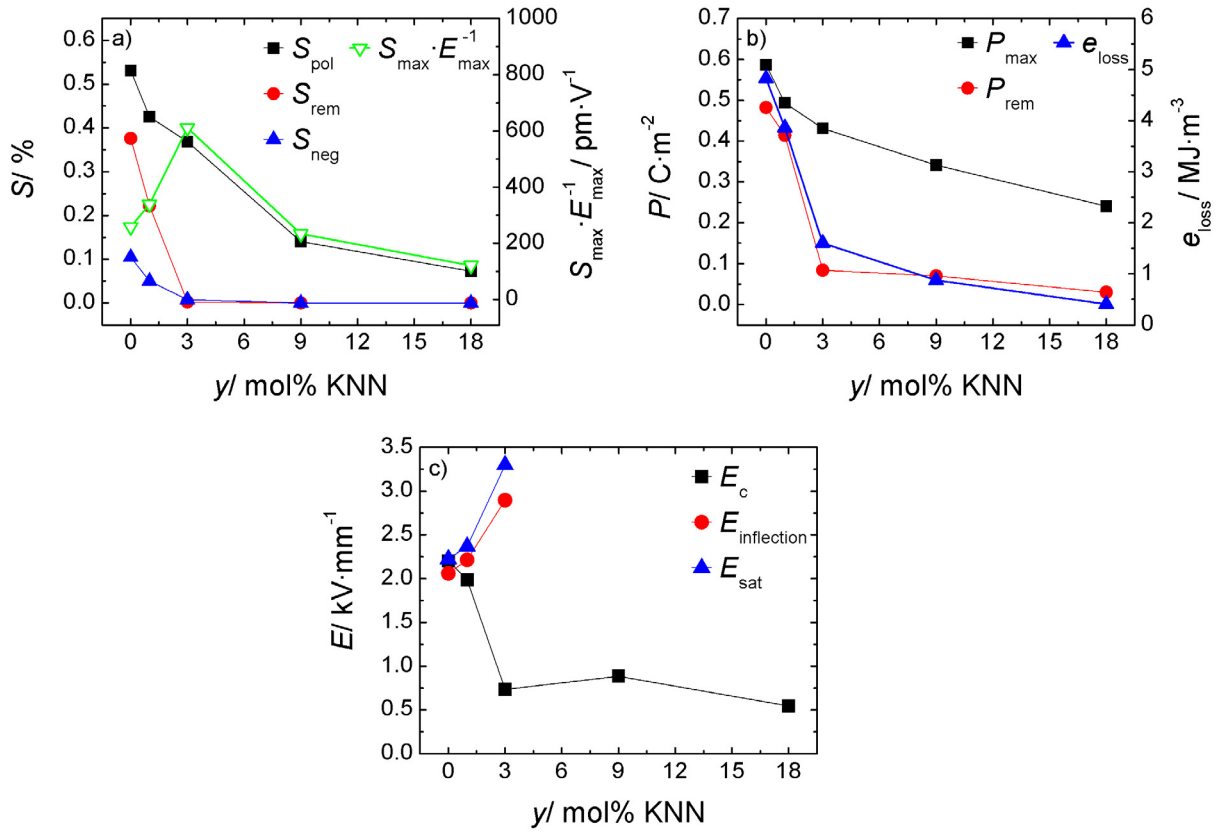

Figure 4.11: Parameters derived from bipolar large-signal measurements on BNT-6BT-100yKNN at 1 mHz and 6 kV·mm^{-1} as a function of y in mol% KNN: a) characteristic values of $S(E)$ curve, S_{pol}, S_{rem}, S_{neg}, and $S_{max}{\cdot}E^{-1}_{max}$; b) characteristic values of $P(E)$ curve, P_{max}, P_{rem}, and e_{loss}; c) characteristic field values, E_c, $E_{inflection}$, and E_{sat}.

in E_{sat} coincides with the increase of $E_{inflection}$, which is determined from the maximum of the derivative of the $S(E)$ curve.

Large-Signal Constitutive Behavior of BNT-20BKT-100yBZT

Despite inherently different chemistry, the BNT-20BKT-100yBZT system exhibits similar properties under high electric fields as the previously shown BNT-6BT-100yKNN system. Depending on the concentration of the ternary compound BZT the strain and polarization behavior may be likewise classified into two types featuring high or very low remanence, respectively.

This is demonstrated in Figure 4.12, where the composition-dependent large-signal properties of BNT-20BKT-100yBZT measured with an amplitude of 6 kV·mm^{-1} at 1 Hz closely resemble that of BNT-6BT-100yKNN. The basic composition with y=0, BNT-20BKT, exhibits a polarization hysteresis that has many of the features of a typical ferroelectric. At 6 kV·mm^{-1}, P_{max} is comparably high with 0.32 C·m^{-2} and a likewise high P_{rem} of 0.29 C·m^{-2}. The coercive field is 3.1 kV·mm^{-1} for both positive and negative electric fields, with a polarization loss density, calculated from the integral area of the second $P(E)$ loop, of 3.7 MJ·m^{-3}. With the incorporation of 2 mol% BZT,

P_{max} and P_{rem} stay virtually constant and the overall shape of the $P(E)$ hysteresis persists. The coercive field, however, slightly increases to 3.5 kV·mm^{-1} and consequently e_{loss} also increases to 4.1 MJ·m^{-3}. Eventually, drastic changes are observed for y=0.04. Despite P_{max} remaining large with 0.35 C·m^{-2}, the overall characteristic of the hysteresis changes to a slim and pinched loop. Thus, P_{rem} decreases to 0.08 C·m^{-2} and E_c has diminished to 1 kV·mm^{-1}, resulting in a decrease of e_{loss} to 1.6 MJ·m^{-3}. As illustrated by Figure 4.13 b), the increase in y to 0.06 causes a decay of P_{max} to 0.3 C·m^{-2} and e_{loss} to 1.2 MJ·m^{-3}. The parameters P_{rem} and E_c exhibit only minor changes to 0.06 C·m^{-2} and 1 kV·mm^{-1}, respectively.

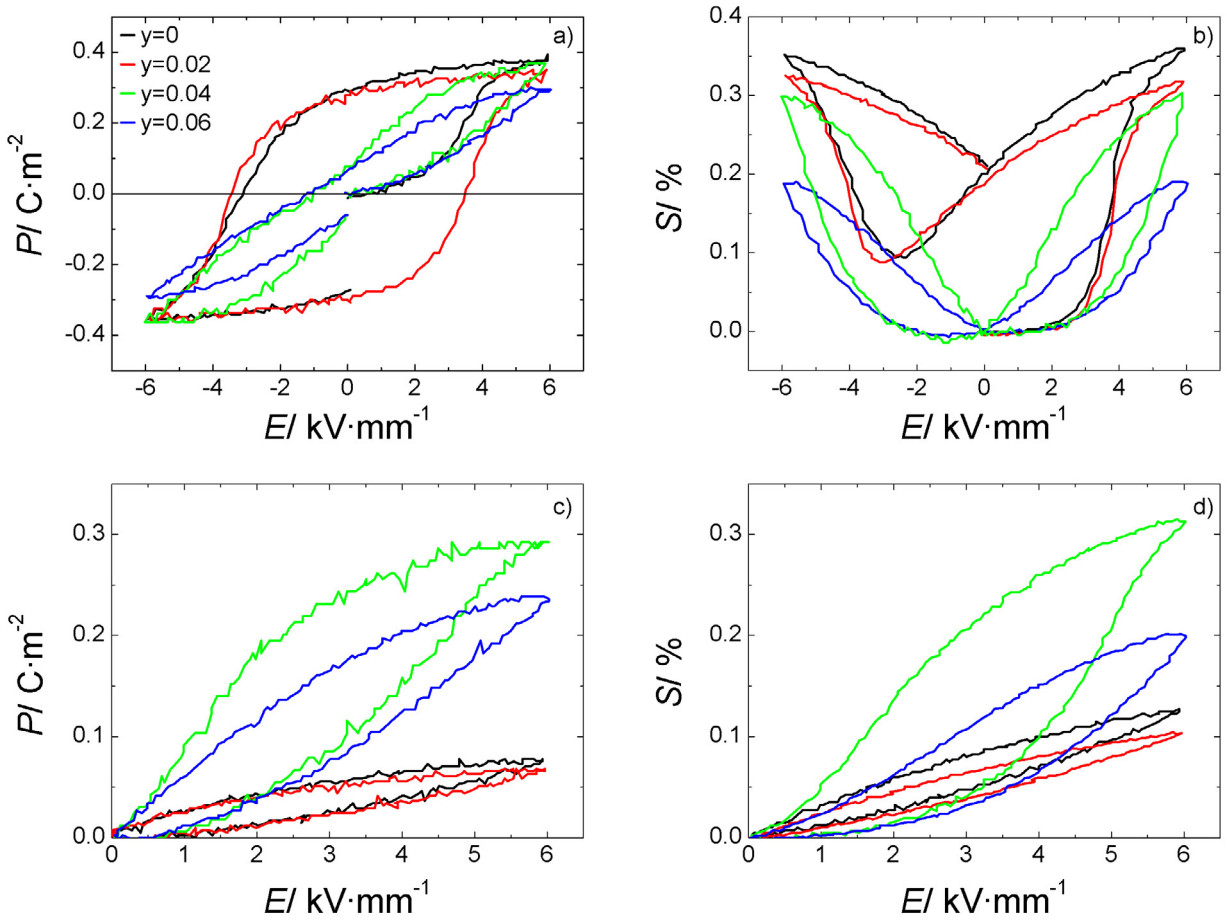

Figure 4.12: Field-induced polarization $P(E)$ and strain $S(E)$ for a, b) bipolar and c, d) unipolar cycling of BNT-20BKT-100yBZT with y={0; 0.02; 0.04; 0.06}.

According to Figure 4.12, BNT-20BKT and BNT-20BKT-2BZT feature $S(E)$ loops with a typical ferroelectric butterfly shape with the development of a remanent strain. The poling strain exceeds 0.3 % at 6 kV·mm^{-1} but due to the high S_{rem} of more than 0.2 %, the usable strain S_{max} is largely diminished beyond the first cycle. While incorporation of 2 mol% BZT hardly affects the field-induced strain behavior, the $S(E)$ loop is notably altered for 4 mol% BZT. The negative strain S_{neg} decreases to almost zero and in contrast to S_{pol}, which remains high at approximately 0.3 %, the remanent strain nearly vanishes. As a consequence, the usable strain is enhanced, represented

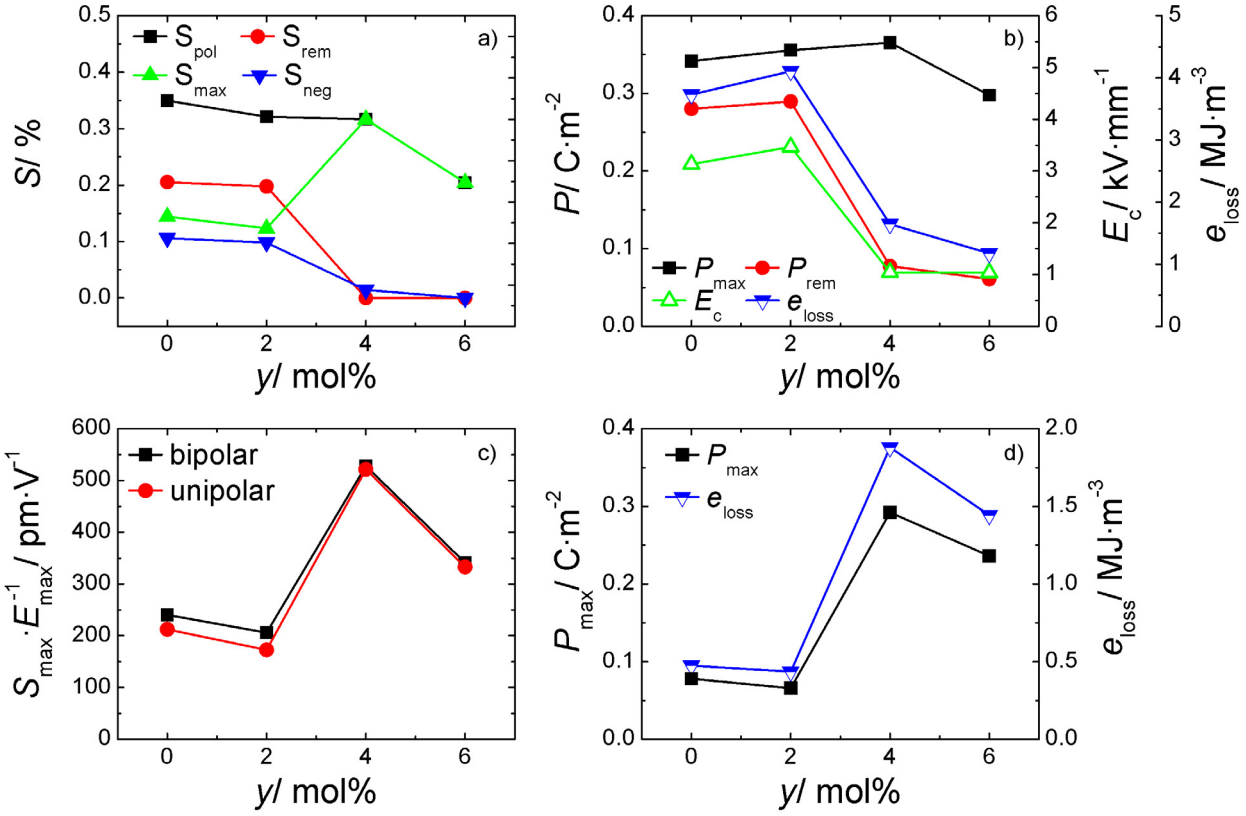

Figure 4.13: Parameters derived from large-signal measurements on BNT-20BKT-100yBZT at 1 Hz and 6 kV·mm^{-1} as a function of y in mol% BZT: a) characteristic values of bipolar $S(E)$ curve, S_{pol}, S_{rem}, S_{max}, and S_{neg}; b) characteristic values of bipolar $P(E)$ curve, P_{max}, P_{rem}, E_c, and e_{loss}; c) normalized strain $S_{max}{\cdot}E_{max}^{-1}$ determined for bipolar and unipolar cycling; d) characteristic values of unipolar $P(E)$ curve, P_{max}, and e_{loss}.

by an increase in $S_{max}{\cdot}E_{max}^{-1}$ from 240 pm·V^{-1} for y=0 and 206 pm·V^{-1} for y=0.02 to 528 pm·V^{-1} for y=0.04. Further addition of BZT, however, leads to a decrease of $S_{max}{\cdot}E_{max}^{-1}$ to 341 pm·V^{-1} in BNT-20BKT-6BZT.

The compositional evolution of the unipolar $S(E)$ hystereses (Figure 4.12 d)) follows for the most part the trend of the bipolar curves. Therefore, curve progression of $S_{max}{\cdot}E_{max}^{-1}$ is almost identical for both bipolar and unipolar cycling, as demonstrated by Figure 4.13 c). It is interesting to note that the large strain in BNT-20BKT-4BZT is induced only under high electric fields beyond 3 kV·mm^{-1}. Below this field, the basic composition without BZT exhibits larger strain. Furthermore, the compositional dependence of both P_{max} and e_{loss} differs from the bipolar evolution with both parameters featuring a pronounced peak at y=0.04. For unipolar measurements on BNT-20BKT-4BZT, P_{max} is 0.29 C·m^{-2} and e_{loss} is 1.9 MJ·m^{-3}.

4.3.2 Influence of Electric Fields on Small-Signal Properties

Small-Signal Properties of BNT-6BT-100yKNN

With increasing KNN content the d_{33} loop becomes slim and shows little remanence. At the same time the hysteresis and the field dependence of the $\varepsilon_{r,33}(E)$ curve are diminished.

Figure 4.14 presents the small-signal electrical properties as a function of applied electric bias field.

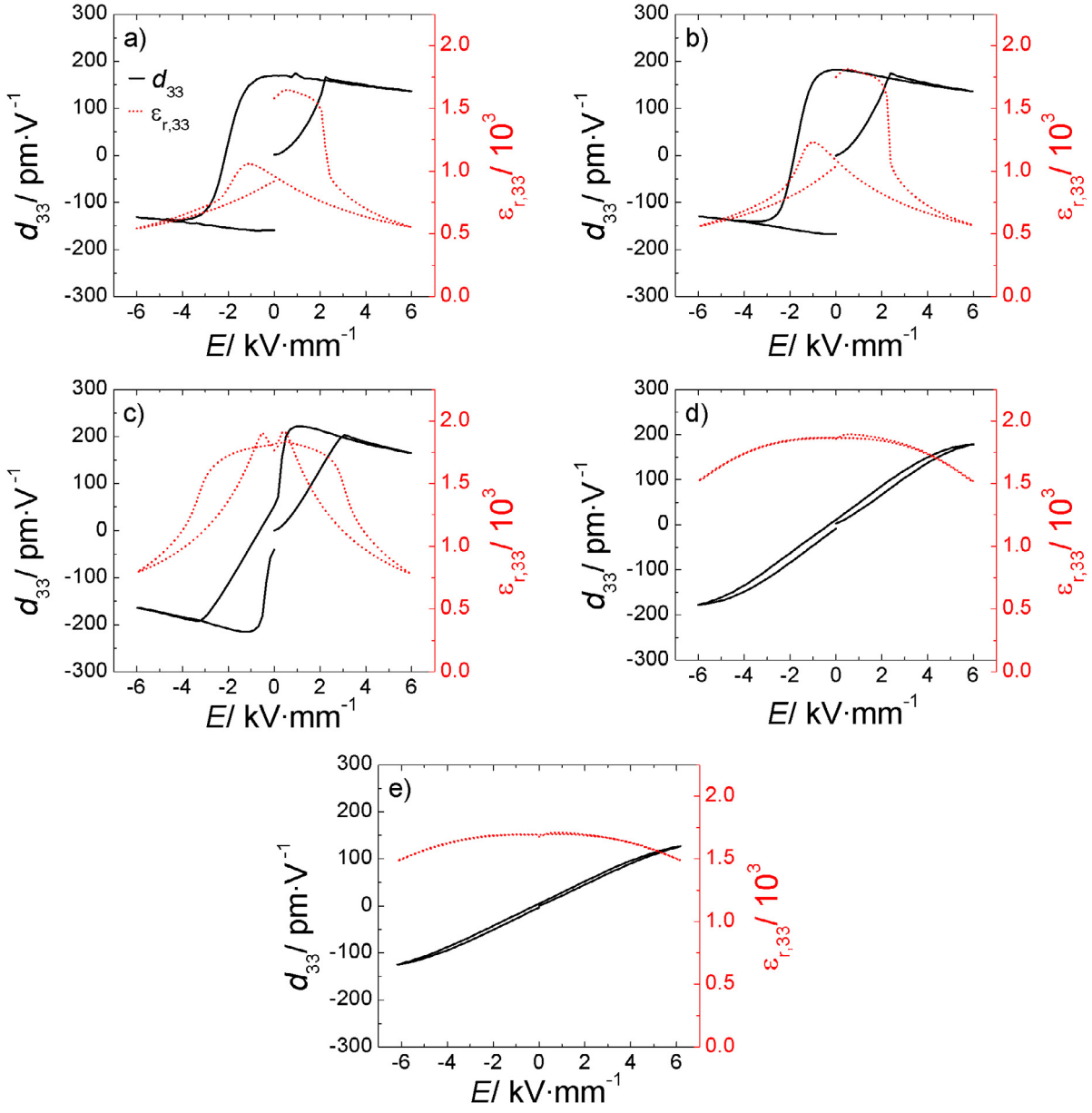

Figure 4.14: Small-signal piezoelectric coefficient d_{33} (solid line) and permittivity $\varepsilon_{r,33}$ (dotted line) as a function of bias field for BNT-6BT-100yKNN with a) y=0.0, b) y=0.01, c) y=0.03, d) y=0.09, and e) y=0.18 as measured from the virgin state.

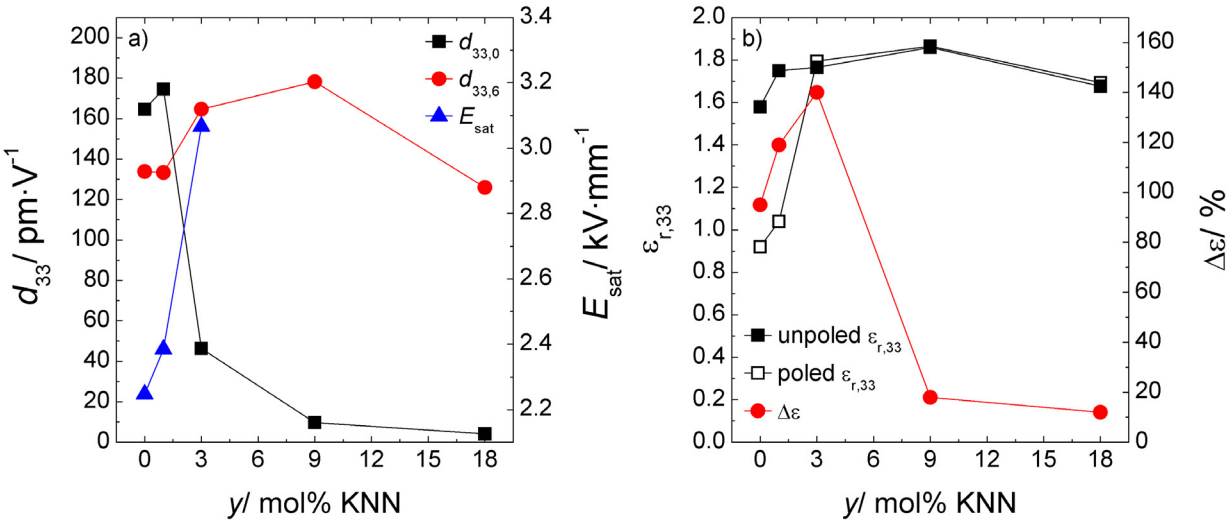

Figure 4.15: Small-signal parameters for BNT-6BT-100yKNN as a function of y in mol% KNN: a) $d_{33,0}$, $d_{33,6}$, and derived E_{sat}; b) $\varepsilon_{r,33}$ for unpoled and poled case along with the according relative difference $\Delta\varepsilon$.

The $d_{33}(E)$ loop resembles to some extent the previously presented $P(E)$ curve. Thus, for y=0, $d_{33}(E)$ increases from zero upon application of an electric field and features a distinct E_{sat} at 2.25 kV·mm^{-1}, which corresponds to the value determined earlier from the $P(E)$ behavior. The d_{33} at the maximum electric field of 6 kV·mm^{-1}, referred to as $d_{33,6}$, is 134 pm·V^{-1} while the remanent value $d_{33,0}$ at zero-field is 165 pm·V^{-1}. With the introduction of KNN, $d_{33,0}$ decreases to only 4 pm·V^{-1} for y=0.18 while $d_{33,6}$ peaks at y=0.09 with 178 pm·V^{-1}. Moreover, E_{sat} increases to 2.38 kV·mm^{-1} for y=0.01 and 3.1 kV·mm^{-1} for y=0.03, hence, complying to the trend of E_{sat} observed in $P(E)$.

The relative permittivity $\varepsilon_{r,33}$ in the unpoled state at zero-field shows a dependence on y and varies between 1580 and 1865. Upon application of small electric fields <1 kV·mm^{-1}, $\varepsilon_{r,33}$ initially increases and then declines at higher electric fields. For y={0; 0.01; 0.03} this drop coincides with the E_{sat} determined from $d_{33}(E)$. After electric field loading the permittivity is significantly reduced to 920 and 1040 for y=0 and y=0.01, respectively. As shown in Figure 4.15, the permittivity at zero-field is virtually unchanged after electrical cycling for higher KNN contents. Compositions with low KNN content $y \leq 0.03$ feature two broad local maxima in $\varepsilon_{r,33}(E)$. The maximum variation $\Delta\varepsilon = \frac{\varepsilon_{max}-\varepsilon_{min}}{\varepsilon_{min}}$ increases from initially 95 % in BNT-6BT to 119 % in BNT-6BT-1KNN and 140 % in BNT-6BT-3KNN. By contrast, the $\varepsilon_{r,33}(E)$ curves for y=0.09 and y=0.18 exhibit a slim parabolic shape with a diminished $\Delta\varepsilon$ of 18 % and 12 %, respectively.

Small-Signal Properties of BNT-20BKT-100yBZT

Similar to the BNT-6BT-100yKNN system, the increase of y in BNT-20BKT-100yBZT yields a decrease in the zero-field value of d_{33} as well as slimmed $d_{33}(E)$ and $\varepsilon_{r,33}(E)$ loops, respectively.

The small-signal parameters d_{33} and ε_{33} are provided by Figure 4.16 as a function of bias field with a maximum electric field amplitude of 6 kV·mm^{-1}.

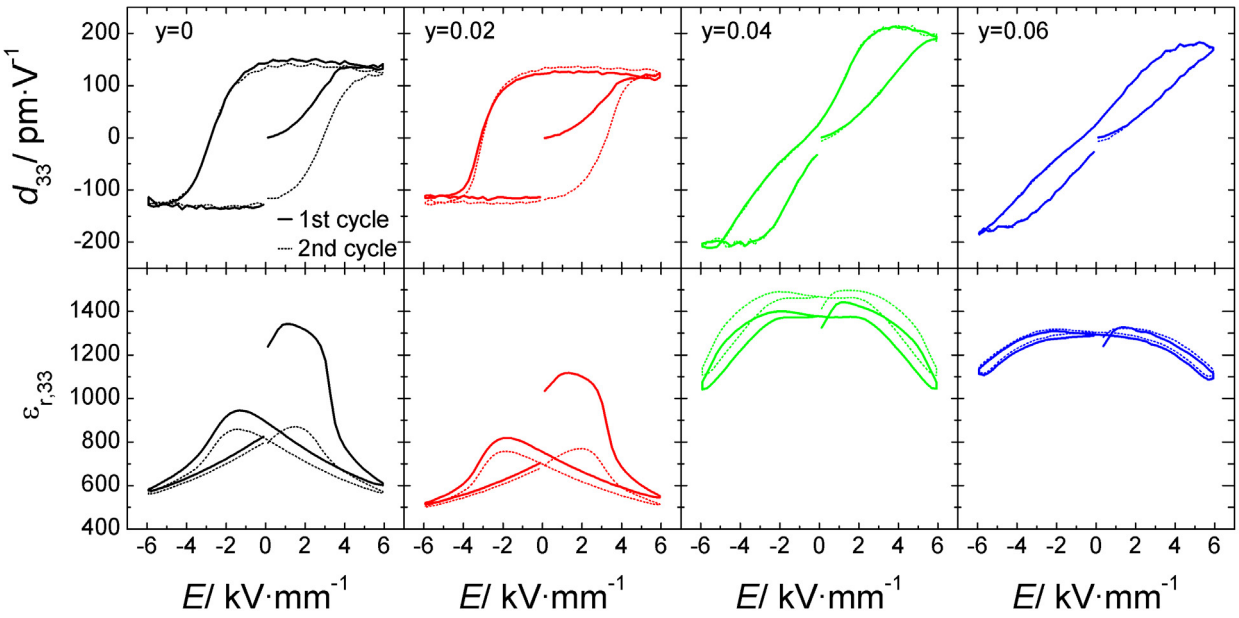

Figure 4.16: Small-signal piezoelectric coefficient d_{33} and permittivity $\varepsilon_{r,33}$ as a function of bias field for BNT-20BKT-100yBZT with y={0; 0.02; 0.04; 0.06}.

It is apparent that the $d_{33}(E)$ loops resemble the corresponding $P(E)$ curves, *i.e.*, for y=0 and y=0.02 the loops are saturating and possess a fairly rectangular shape. During poling from the virgin state in the first half-cycle an E_{sat} can be determined as 3.7 kV·mm^{-1} in BNT-20BKT and 4 kV·mm^{-1} in BNT-20BKT-2BZT. When the electric field is decreased from the maximum value to zero, the piezoelectric coefficient stays virtually constant, with d_{33} shifting from 143 pm·V^{-1} to 141 pm·V^{-1} in BNT-20BKT and from 124 pm·V^{-1} to 123 pm·V^{-1} in BNT-20BKT-2BZT. By contrast, $d_{33,6}$ and $d_{33,0}$ of y=0.04 and y=0.06 diverge significantly, as depicted in Figure 4.17, *e.g.*, in BNT-20BKT-4BZT d_{33} drops from 194 pm·V^{-1} to 26 pm·V^{-1}. Moreover, neither of these two compositions feature a distinct E_{sat}.

Upon application of an electric field the permittivity $\varepsilon_{r,33}$ initially increases and subsequently decreases in all compositions. For y=0, $\varepsilon_{r,33}$ decreases notably from 1239 at zero-field to 602 at 6 kV·mm^{-1} and for y=0.02 $\varepsilon_{r,33}$ decreases from 1036 to 544. The permittivity curve of both materials exhibits a steep slope in the vicinity of the previously determined E_{sat}. Then, when the field is removed, the permittivity of these two compositions increases gradually. However, the zero-field values are smaller than in the unpoled state, *i.e.*, $\varepsilon_{r,33}$ decreases to 893 and 753 for y=0 and y=0.02 (Figure 4.17 b)). In addition, the $\varepsilon_{r,33}(E)$ curves of poled BNT-20BKT and

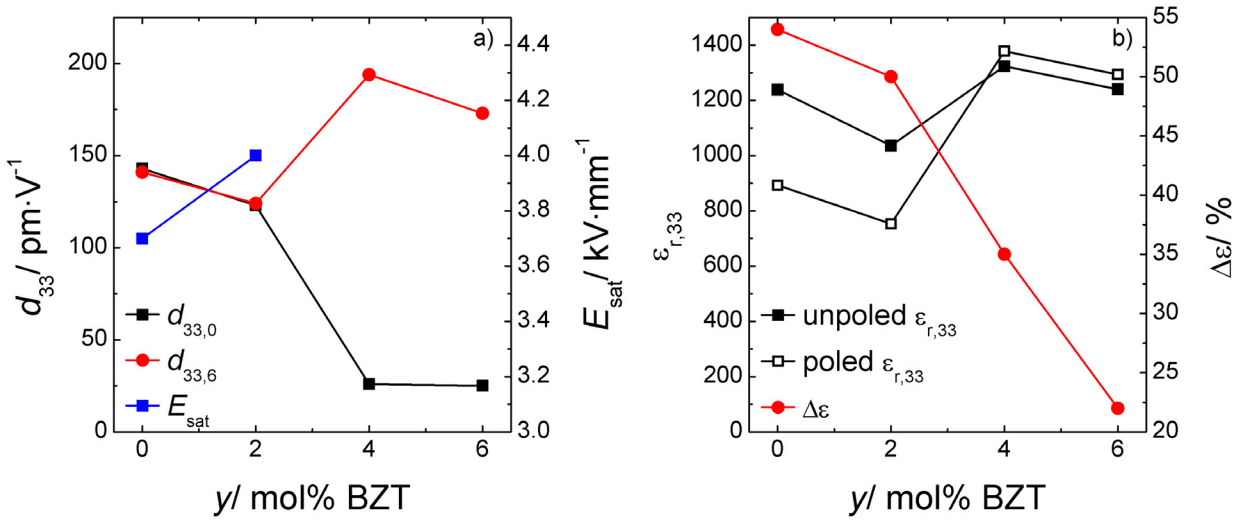

Figure 4.17: Characteristic figures derived from small-signal measurements of a) d_{33} and b) $\varepsilon_{r,33}$ for BNT-20BKT-100yBZT with a field amplitude of 6 kV·mm^{-1} as a function of BZT content y.

BNT-20BKT-2BZT exhibit maxima in the vicinity of E_c. By contrast, the $\varepsilon_{r,33}(E)$ curves for BNT-20BKT-4BZT and -6BZT do not feature two distinct maxima. The discrepancy between unpoled and poled zero-field permittivity is reduced and there is no drop in $\varepsilon_{r,33}(E)$ after poling. The increasing BZT content has a flattening effect on the field-dependent permittivity, *i.e.*, the variation $\Delta\varepsilon = \frac{\varepsilon_{max}-\varepsilon_{min}}{\varepsilon_{min}}$ changes from initially 54 % for y=0 to 50 % for y=0.02, 35 % for y=0.04, and finally 22 % for y=0.06.

4.3.3 Influence of Amplitude on the Large-Signal Constitutive Behavior

Irrespective of BZT content, the large-signal behavior of BNT-19BKT-100yBZT is virtually indistinguishable for electric fields below 2 kV·mm^{-1}. The addition of BZT impedes the establishment of a remanent strain at high electric fields, which otherwise constrains S_{max}·E_{max}^{-1}.

As presented earlier, BNT-BKT-BZT may develop large strains, however, only under very high electric fields (Figure 4.12). In order to investigate the influence of the electric field amplitude on the electromechanical behavior, the large-signal properties of BNT-19BKT-100yBZT are assessed from the virgin state with varying field amplitude.

At low fields $\leq$2 kV·mm^{-1} the hystereses exhibit little composition dependence (Figure 4.18). Irrespective of BZT content, the $S(E)$ loops exhibit only small remanent and negative strain and the $P(E)$ loop is a thin ellipse with accordingly low P_{rem}.

At higher fields, however, the evolution of strain and polarization is strongly dependent on the respective composition. Figure 4.19 presents $P(E)$ and $S(E)$ loops for y={0.02; 0.03; 0.04} for different electric fields from 1 kV·mm^{-1} up to 6 kV·mm^{-1}. For y=0.02, cycling with a maximum electric field of 4 kV·mm^{-1} results in the development of the typical butterfly loop with significant S_{rem} and S_{neg}. Moreover, S_{rem} increases upon consecutive cycling and for this reason the

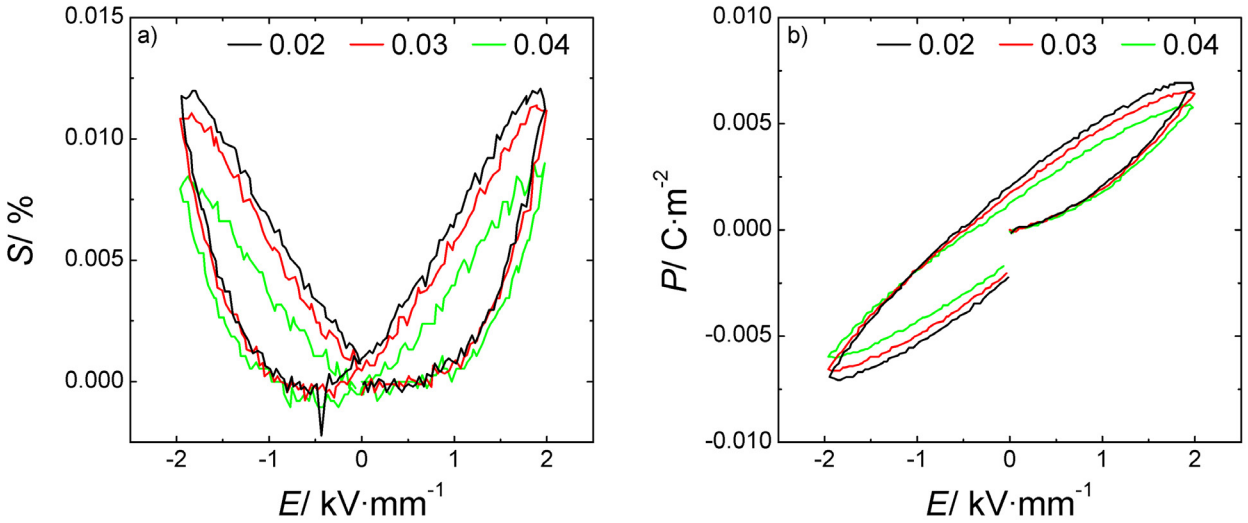

Figure 4.18: Strain (a) and polarization (b) as a function of electric field with an amplitude of 2 kV·mm^{-1} for BNT-19BKT-100yBZT with y={0.02; 0.03; 0.04}.

$S(E)$ loop appears asymmetric. For an amplitude of 5 kV·mm^{-1}, the polarization reaches saturation, where E_{sat}=4.7 kV·mm^{-1}. Moreover, the strain in the first half-cycle rapidly increases up to 5 kV·mm^{-1} but the slope decreases close to the maximum field. The maximum slope $^{\Delta S}/_{\Delta E}$ is measured at approximately 4 kV·mm^{-1}. Finally, for the highest applied field, remanent and maximum values increase, albeit to a lesser extent than in previous steps.

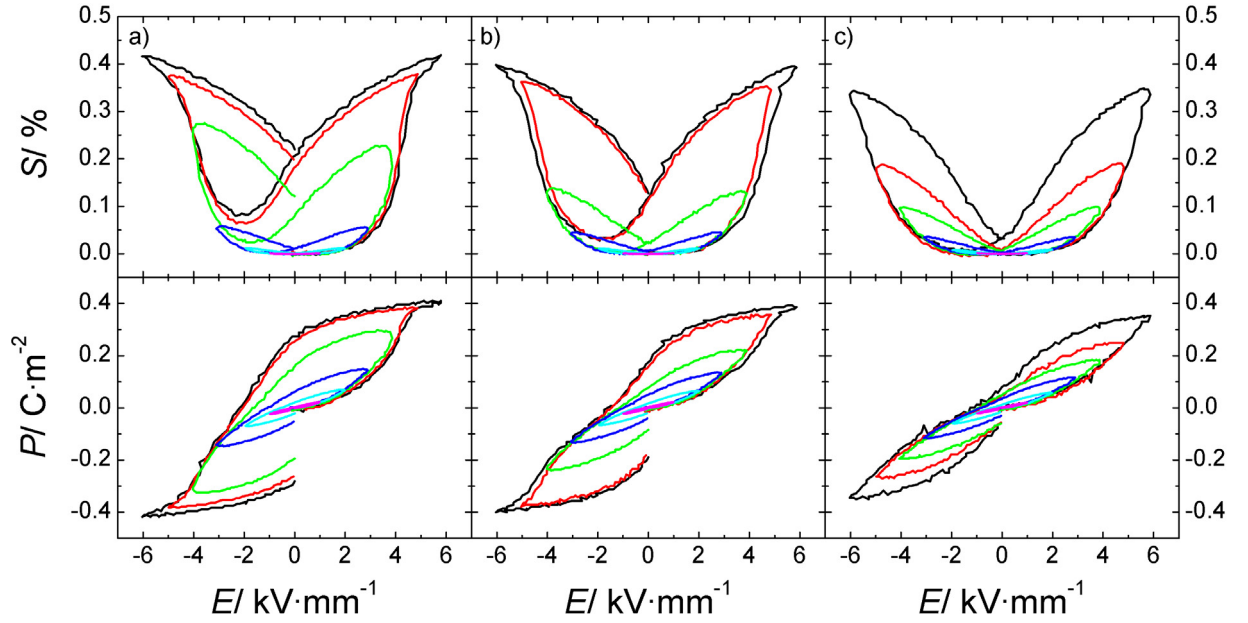

Figure 4.19: Field-induced strain and polarization from the annealed virgin state in BNT-19BKT-100yBZT with a) y=0.02, b) y=0.03, c) y=0.04 at 1 Hz for field amplitudes from 1 kV·mm^{-1} through 6 kV·mm^{-1}.

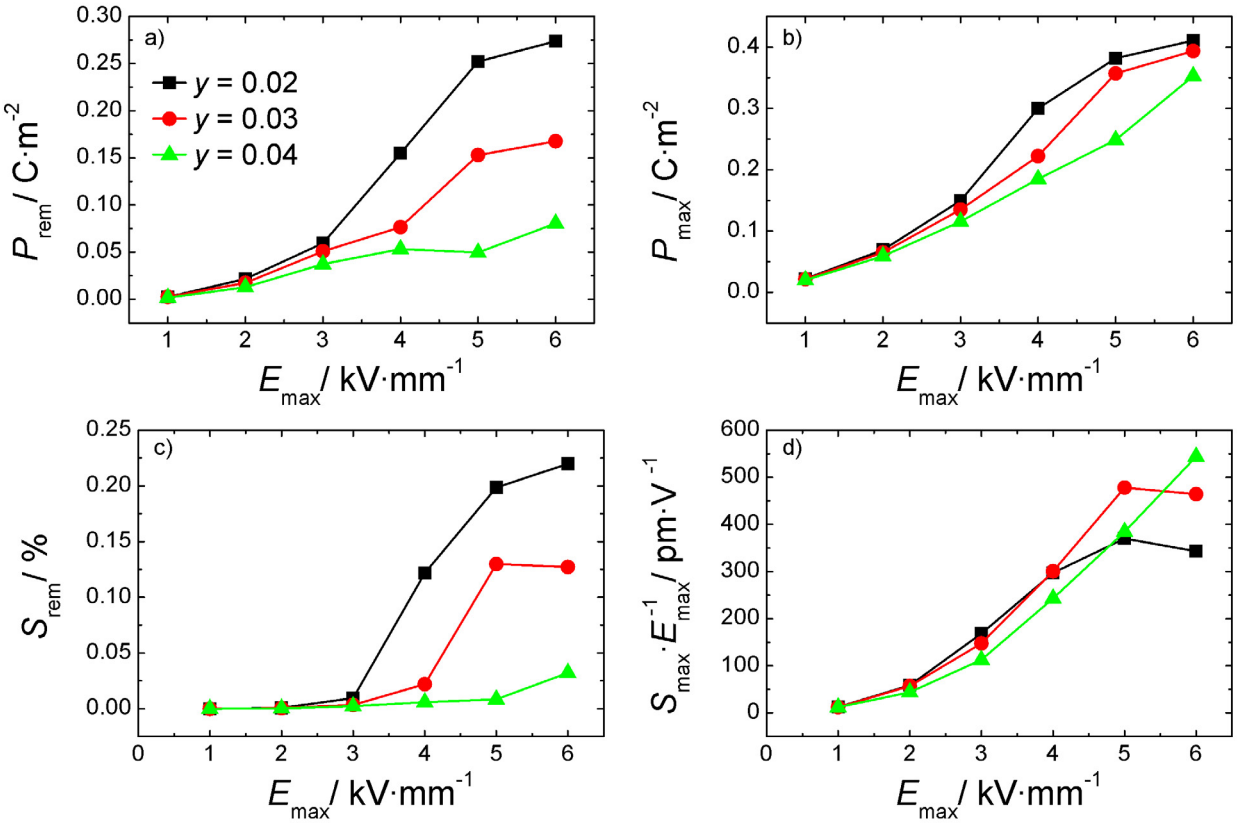

Figure 4.20: a) Remanent and b) maximum polarization in addition to c) remanent strain and d) $S_{max} \cdot E_{max}^{-1}$ as a function of field amplitude for BNT-19BKT-100yBZT with y={0.02; 0.03; 0.04}.

By contrast, for y=0.04 the $P(E)$ and $S(E)$ hystereses effectively scale up with increasing field, which means that both curves gradually evolve without abrupt changes and increase to higher maximum values. Figure 4.20 d) demonstrates that this evolution is not linear but can be described by a parabola.

The intermediate composition with y=0.03 depicts a transition between the other two materials, which is illustrated by Figures 4.20 c) and d). In comparison to y=0.02, higher fields are required for y=0.03 to establish a sizable S_{rem}. This means that the scaling, which is observed for y=0.04 throughout all applied electric fields, occurs here as well, albeit only up to between 3 kV·mm^{-1} to 4 kV·mm^{-1}. Compared to y=0.02, the deviation from the parabolic evolution of S_{max} sets in at higher electric fields, namely at 5 kV·mm^{-1} rather than 4 kV·mm^{-1}. It is interesting to note that the composition with y=0.02 has the highest strain at a comparably low electric field of 3 kV·mm^{-1}. At 5 kV·mm^{-1}, however, the highest strain is found for y=0.03 and at 6 kV·mm^{-1} the highest strain is found for y=0.04.

As suggested by the observation of very similar $P(E)$ loops, the dissipated energy density e_{loss} is virtually identical among all three materials up to 2 kV·mm^{-1}. According to Figure 4.21, the composition-dependent spread in e_{loss} begins at 3 kV·mm^{-1}. With an electric field amplitude of 6 kV·mm^{-1}, e_{loss} is 3.3 MJ·m^{-3} for y=0.02, 2.53 MJ·m^{-3} for y=0.03, and 1.7 MJ·m^{-3} for y=0.04.

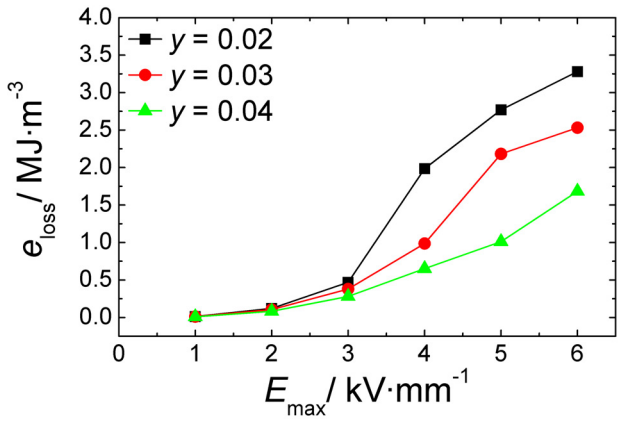

Figure 4.21: Polarization loss density as a function of field amplitude for BNT-19BKT-100yBZT with y={0.02; 0.03; 0.04}.

4.3.4 Influence of Frequency on the Large-Signal Constitutive Behavior

It was found that both the remanent strain and polarization were virtually frequency-insensitive, while maximum strain, maximum polarization, and coercive field feature sizable variations with frequency depending on both composition and field amplitude.

The influence of the frequency of the applied electric field on both field-induced polarization and strain was investigated. As demonstrated by Figure 4.22 the compositions BNT-19BKT-100yBZT with y={0.02; 0.03; 0.04} display a smooth transition. BNT-19BKT-2BZT features a ferroelectric-

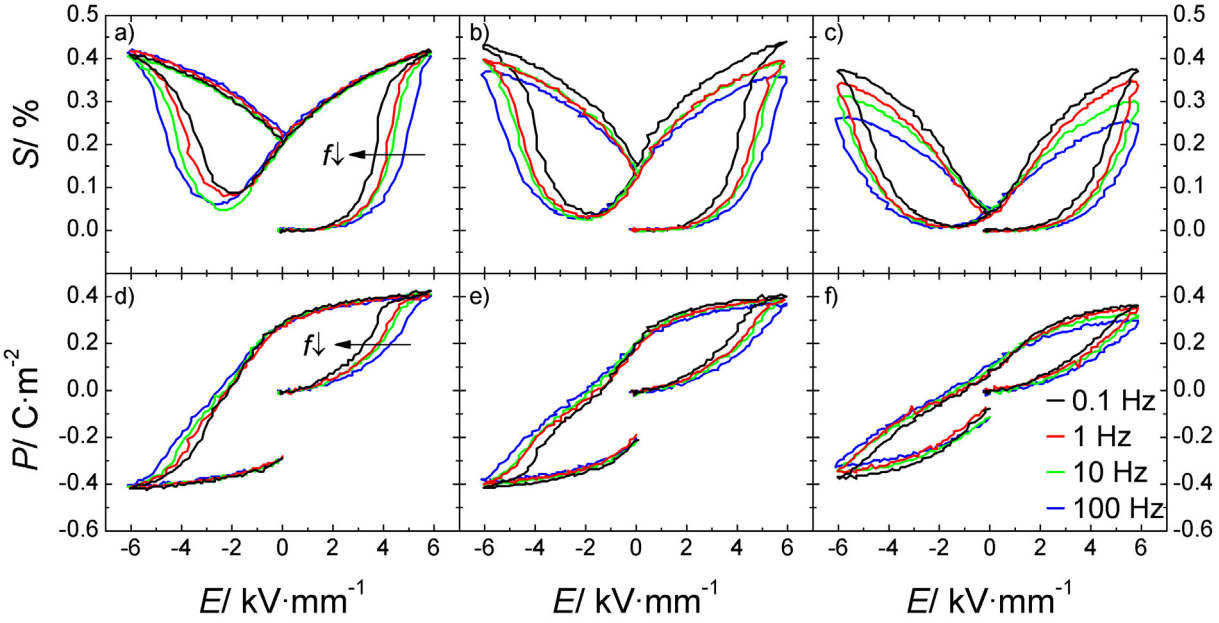

Figure 4.22: Frequency dependence of field-induced strain and polarization for BNT-19BKT-100yBZT with a, d) y=0.02, b, e) y=0.03, and c, f) y=0.04 at frequencies from 0.1 Hz to 100 Hz.

like characteristic with a butterfly shape of the $S(E)$ loop and large remanent strain, while BNT-19BKT-4BZT exhibits large usable strain due to diminished S_{rem}. The composition in-between, BNT-19BKT-3BZT, shows an intermediate behavior with decreased yet comparably high remanent strain. This smooth transition affords a systematic study on the compositional evolution of the frequency dependence of electromechanical properties.

At 0.1 Hz, S_{rem} decreases with y from 0.21 % to 0.16 % and 0.04 %, while S_{pol} exhibits less variation with 0.42 %, 0.43 %, and 0.37 %. Consequently, the normalized strain $S_{max}{\cdot}E_{max}^{-1}$ increases with y from 349 pm·V^{-1} to 445 pm·V^{-1} and eventually to 580 pm·V^{-1}. The $P(E)$ curves behave accordingly, *i.e.*, P_{rem} drops significantly from 0.28 C·m^{-2} to 0.20 C·m^{-2} and 0.06 C·m^{-2}; P_{max} decreases to a lesser extent from 0.43 C·m^{-2} to 0.40 C·m^{-2} and 0.36 C·m^{-2}.

On the one hand, throughout all materials, relevant field parameters, such as the coercive field E_c, the field of maximum slope in the $S(E)$ curve $E_{inflection}$, and the field of maximum negative strain E_{neg}, increase with increasing frequency (Figure 4.23). The frequency dependence of these field parameters is in a first approximation linear when plotted logarithmically as a function of frequency. The slope, however, varies, implying differing frequency dependence. A linear curve fit yields an averaged slope of 358 V·(log($f/_{Hz}$))$^{-1}$ for $E_{inflection}$, 173 V·(log($f/_{Hz}$))$^{-1}$ for E_c, and 253 V·(log($f/_{Hz}$))$^{-1}$ for E_{neg}.

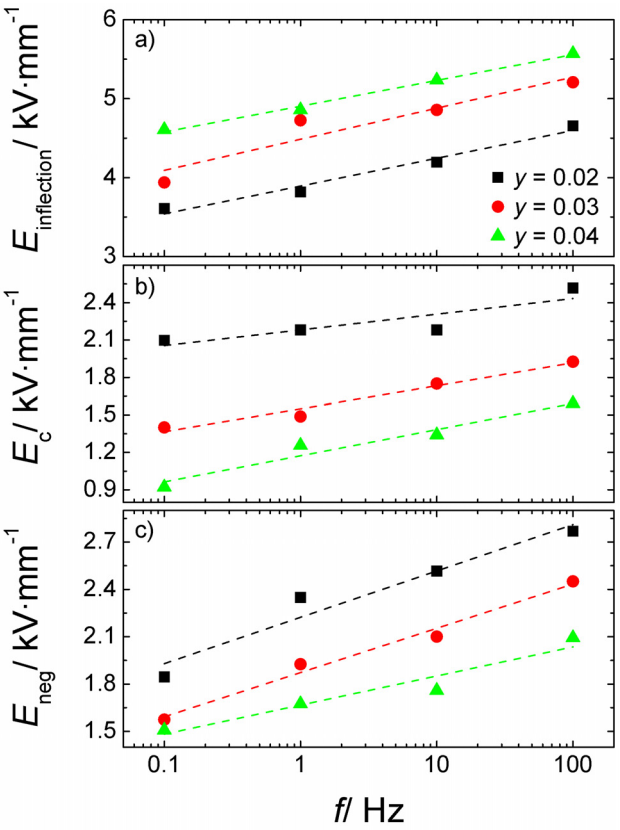

Figure 4.23: Characteristic field values $E_{inflection}$, E_c, and E_{neg} as a function of frequency for BNT-19BKT-100yBZT with y={0.02; 0.03; 0.04}.

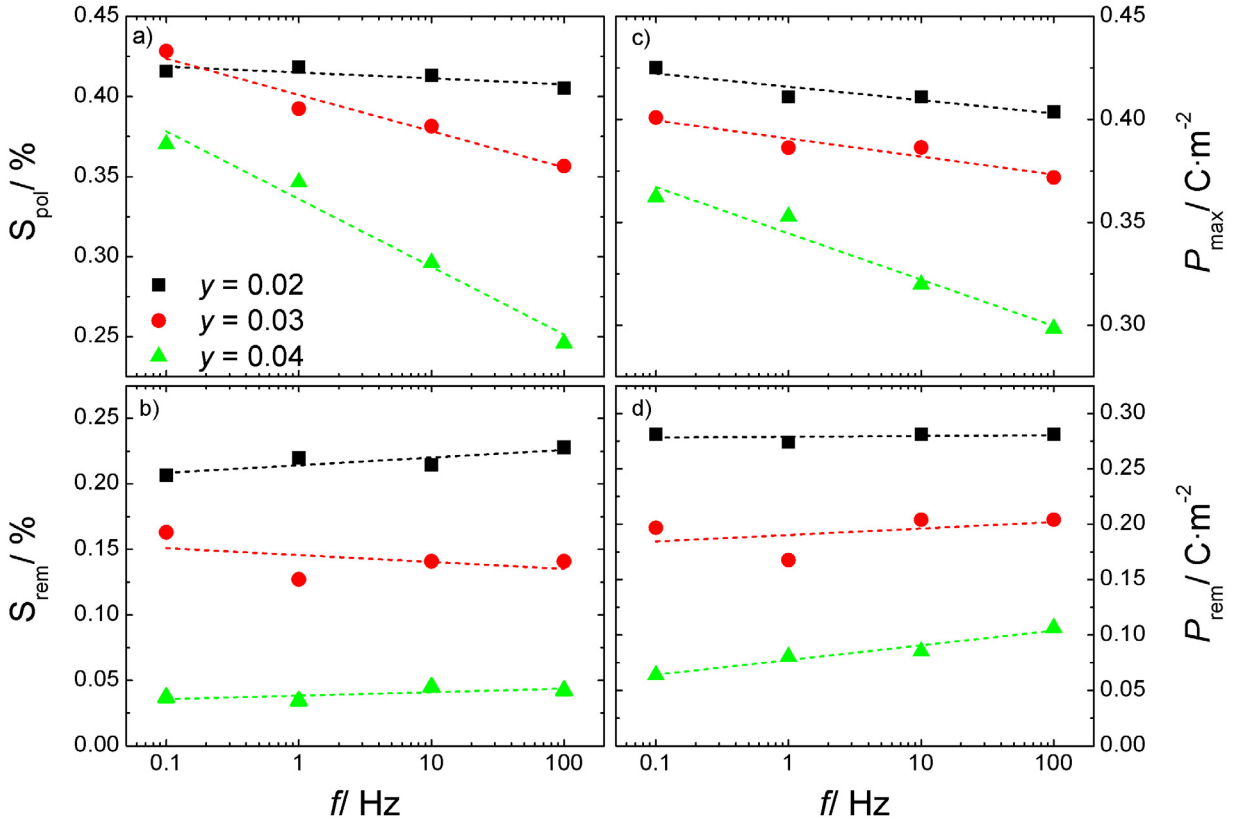

Figure 4.24: Characteristic strain and polarization values as a function of frequency for BNT-19BKT-100yBZT with y={0.02; 0.03; 0.04}: a) poling strain S_{pol}, b) remanent strain S_{rem}, c) maximum polarization P_{max}, and d) remanent polarization P_{rem}.

On the other hand, it is apparent that a variation of frequency exerts different effects on characteristic strain and polarization parameters depending on composition. Poling strain remains virtually constant in BNT-19BKT-2BZT, *e.g.*, 0.42 % at 0.1 Hz and 0.41 % at 100 Hz. By contrast, S_{pol} in BNT-19BKT-3BZT drops by 16 % from 0.43 % at 0.1 Hz to 0.36 % at 100 Hz and, even more pronounced, drops by 32 % in BNT-19BKT-4BZT from 0.37 % at 0.1 Hz to 0.25 % at 100 Hz. Interestingly, S_{rem} is nearly independent of frequency in all compositions. Therefore, $S_{max}{\cdot}E_{max}^{-1}$ of BNT-19BKT-4BZT decays notably with increasing frequency from 580 pm·V^{-1} at 0.1 Hz down to 340 pm·V^{-1} at 100 Hz. The compositional and frequency dependence of the polarization largely represents the trend observed for strain. Thus, the maximum polarization decreases with frequency and this effect is more pronounced for higher BZT content, *e.g.*, in BNT-19BKT-2BZT P_{max} decreases by 5 % from 0.43 C·m^{-2} at 0.1 Hz to 0.40 C·m^{-2} at 100 Hz while in BNT-19BKT-4BZT P_{max} decreases by 18 % from 0.36 C·m^{-2} to 0.3 C·m^{-2}. The remanent polarization for BNT-19BKT-4BZT slightly increases from 0.06 C·m^{-2} to 0.10 C·m^{-2}. The increase in P_{rem} is associated with a decreased constriction of the $P(E)$ loop, *i.e.*, the hysteresis exhibits a less pinched shape at higher frequencies. This effect occurs in all compositions but is most prominent for y=0.04. The dissipated energy during bipolar cycling e_{loss} decreases with y and increases with frequency, as demonstrated by Figure 4.25.

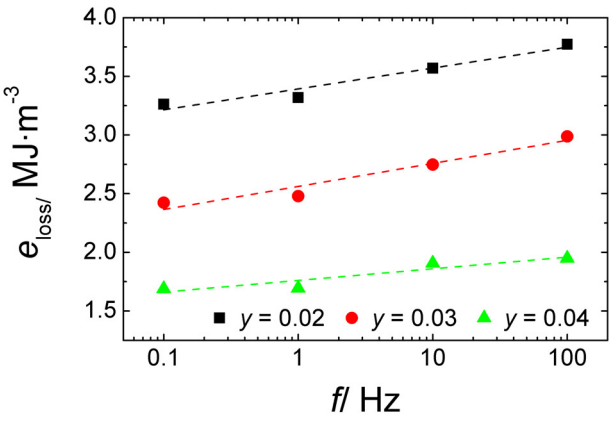

Figure 4.25: Integral area of the $P(E)$ loop, e_{loss}, as a function of frequency for BNT-19BKT-100yBZT with y={0.02; 0.03; 0.04}

4.3.5 *In situ* XRD as a Function of Electric Field

In order to investigate structural changes under electric field, high-energy in situ *XRD experiments were conducted on BNT-20BKT-100yBZT with y={0; 0.02; 0.04; 0.06} and field amplitudes of 6 kV·mm^{-1}. Beyond a threshold electric field BNT-20BKT shows an irreversible broadening of Bragg reflections in the diffraction pattern, depending on the angle between scattering vector and electric field. With increasing BZT content, the threshold field increases until no such broadening or angular dependence is observed anymore for $y\geq$0.04 at 6 kV·mm^{-1}.*

All compositions consist of a single perovskite phase except for BNT-20BKT-2BZT where traces of an unidentifiable second phase are found. Judging from the integrated intensity of the respective spurious reflections, this second phase has a volume fraction on the order of 1 %.

Figure 4.26 presents the diffraction patterns of the $\{111\}_c$ reflection as a function of increasing and decreasing electric field and Figure 4.27 represents the equivalent patterns for the $\{200\}_c$ reflection. Unless stated otherwise, the electric field vector and the scattering vector are parallel. Initially, the base composition BNT-20BKT is pseudocubic at zero-field as reflections are symmetric without any pronounced non-cubic distortion. At $2\theta\approx$3.47 °, however, a slight reflection is observed, which cannot be rationalized with a purely cubic structure. This $^1/_2\{311\}_c$ superlattice reflection is a result of antiphase oxygen octahedral tilting referred to as $a^-a^-a^-$ in Glazer notation.[93] According to Glazer, this superlattice reflection is indicative of the $R3c$ space group. Therefore, despite the lack of non-cubic distortions in the Bragg reflections, virgin BNT-20BKT appears to some extent to be rhombohedral. For electric fields below 1 kV·mm^{-1}, the diffraction pattern is virtually unchanged. Upon the application of >1 kV·mm^{-1}, however, the reflections begin to broaden, as illustrated for $\{111\}_c$ and $\{200\}_c$ in Figures 4.26 and 4.27. Beyond a threshold of 3.2 kV·mm^{-1} this broadening increases notably and at the same time the peak intensity drops by 18 % compared to zero-field. The underlying reason for the observed increase in the reflection width is reflection splitting, *e.g.*, $\{111\}_c$ splits into the reflection doublet $(111)_r$ and $(11\bar{1})_r$ and $\{200\}_c$ splits into $(200)_t$ and $(002)_t$. While the splitting in $\{111\}_c$ may indicate rhombohedral

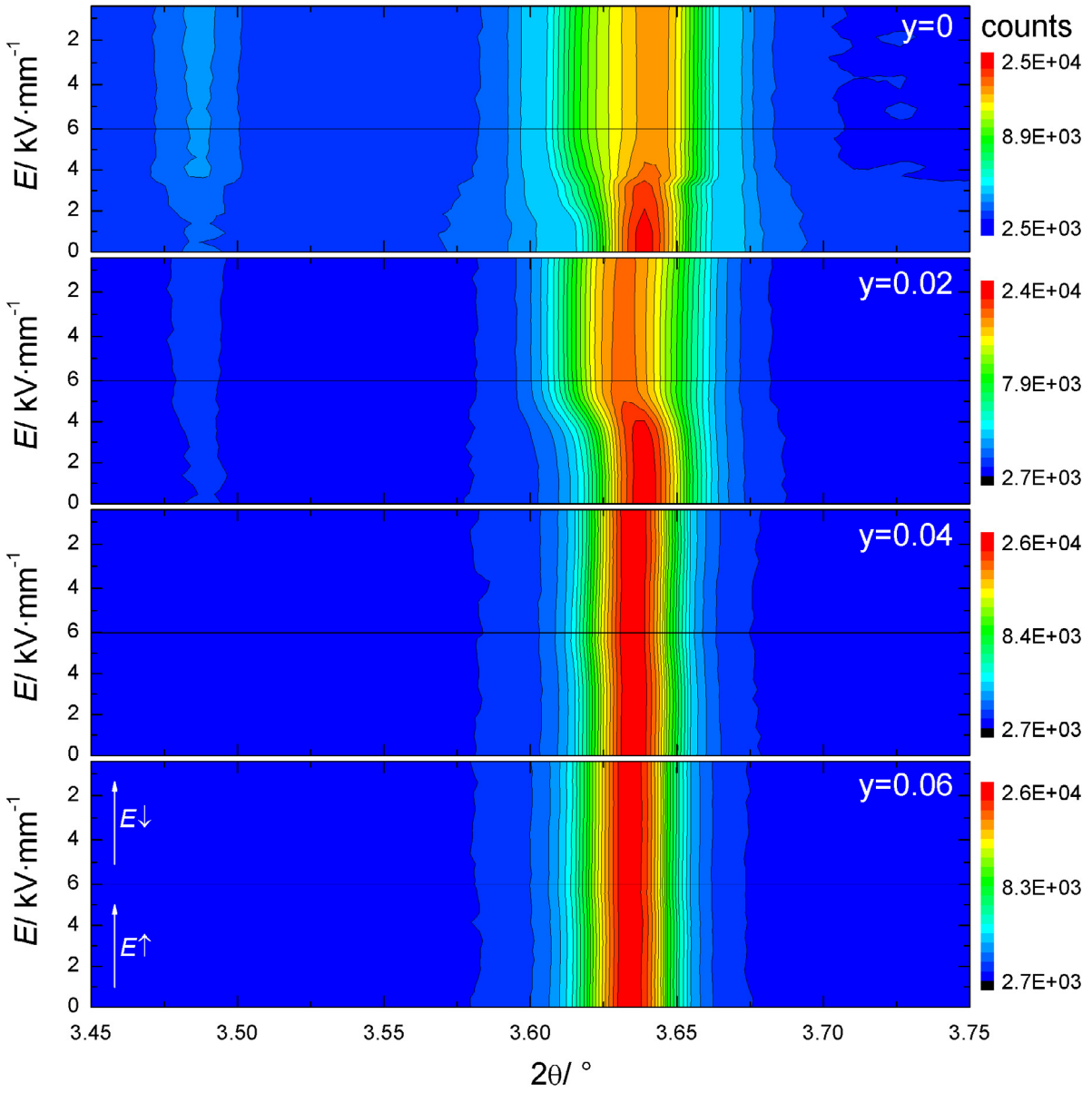

Figure 4.26: Contour plots from the diffraction patterns of the $^1/_2\{311\}_c$ superlattice reflections and the $\{111\}_c$ reflections measured by *in situ* XRD as a function of increasing and decreasing electric field for BNT-20BKT-100yBZT with y={0; 0.02; 0.04; 0.06}.

symmetry, the asymmetry in $\{200\}_c$ can be associated with tetragonal symmetry. The splitting, however, is minute and thus no separated reflections can be determined. Moreover, the $^1/_2\{311\}_c$ superlattice reflection increases at approximately 3.2 kV·mm^{-1} in intensity by 7 %, which is only 11 % higher than the background intensity. When the electric field is reduced to zero again, most of the induced changes in the diffraction pattern persist to their initial state, *i.e.*, the increased $^1/_2\{311\}_c$ superlattice reflection and the peak splitting remain.

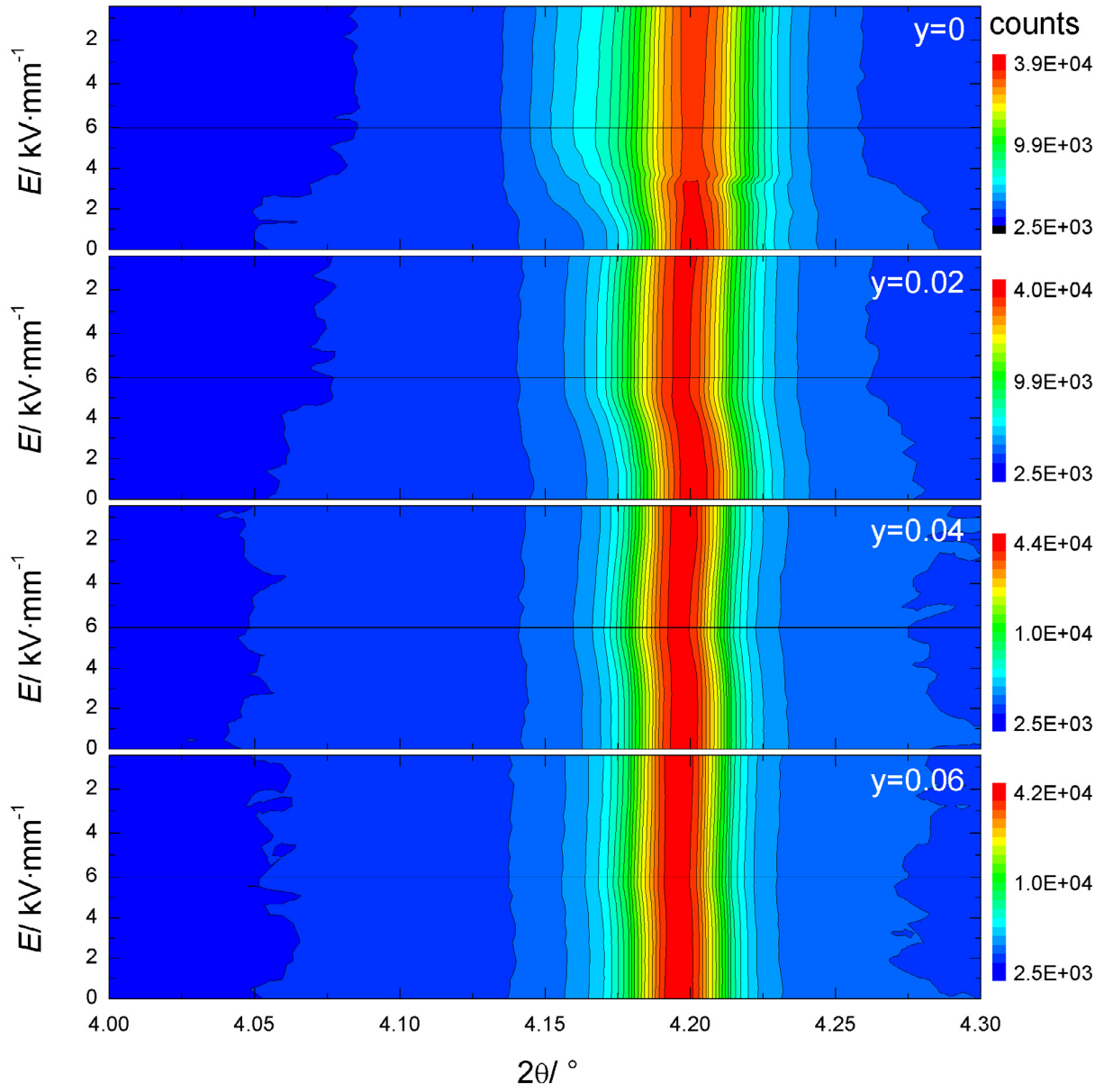

Figure 4.27: Contour plots from the diffraction patterns of the $\{200\}_c$ reflections measured by *in situ* XRD as a function of increasing and decreasing electric field for BNT-20BKT-100yBZT with y={0; 0.02; 0.04; 0.06}.

The field-dependent structural evolution for y=0.02 strongly resembles the aforementioned progression for y=0. Therefore, broadening also occurs, albeit at higher field. Notable peak splitting of $\{111\}_c$ and $\{200\}_c$ sets in at 4 kV·mm^{-1}. The increase in the intensity of $^1/_2\{311\}_c$ by approximately 2 % is less pronounced than for y=0.

From Figure 4.26 and 4.27 it is readily apparent that the field-dependent structural evolution is drastically altered for y=0.04. In contrast to the former two compositions, the diffraction patterns feature neither superlattice reflections nor a pronounced, irreversible reflection broadening. In-

stead, the unit cell is distorted under the electric field and subsequently reverts to the initial shape under decreasing field as demonstrated by the shift in 2θ peak position of $\{111\}_c$ and $\{200\}_c$. Consequently, the peak width is nearly constant and the effect of decreasing peak intensity under increasing field is reduced. With the addition of 6 mol% BZT both the field-induced reversible shift of the reflections and the decrease of peak intensity are further reduced, *i.e.*, the effect of the electric field on the structure is diminished.

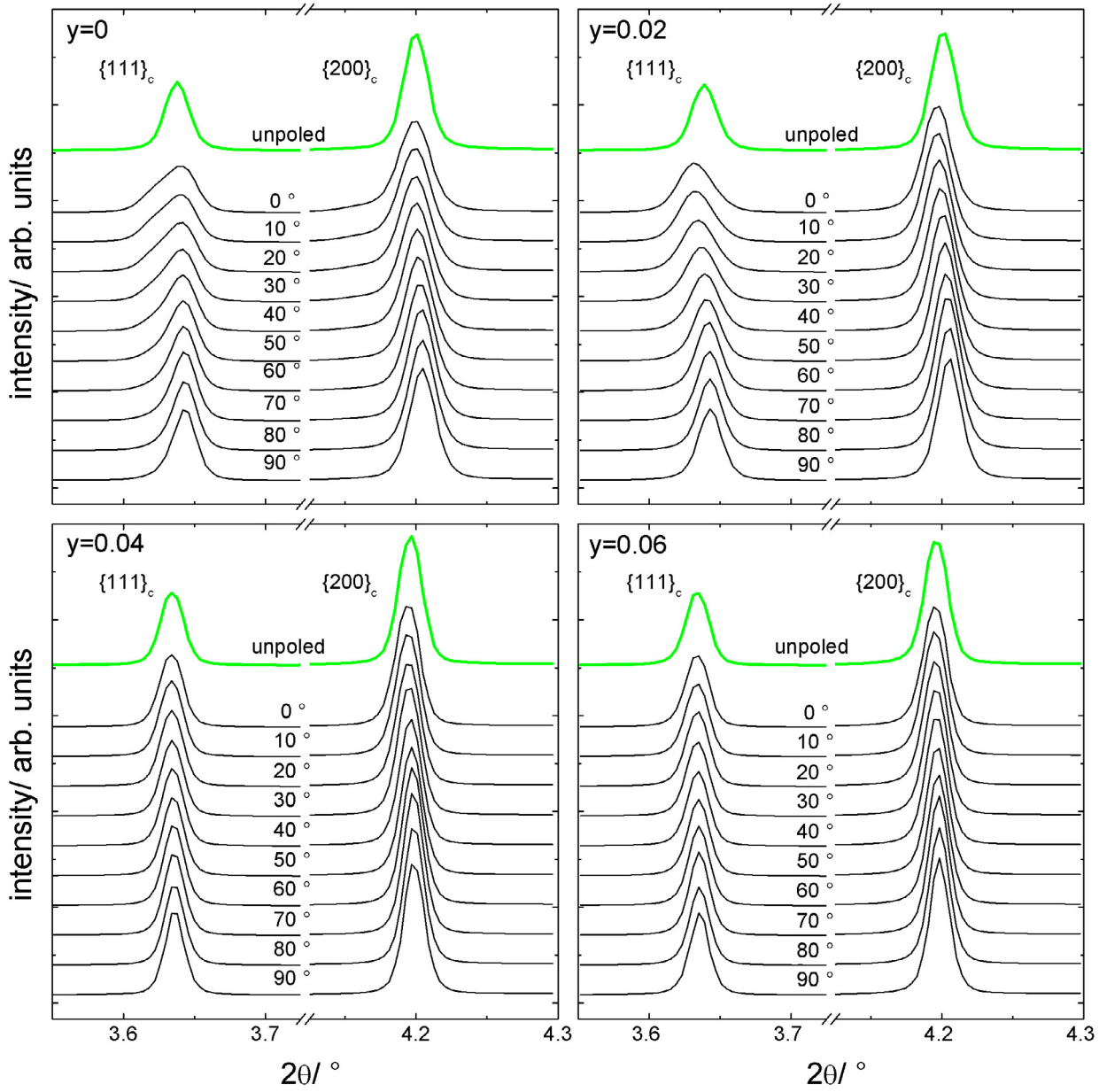

Figure 4.28: Diffraction patterns of the $\{111\}_c$ and $\{200\}_c$ reflections in the unpoled (green lines) and the poled state (black lines) at 6 kV·mm^{-1}. The angle ξ between scattering vector q and electric field is rotating from 0 ° through 90 ° for BNT-20BKT-100yBZT with y={0; 0.02; 0.04; 0.06}.

For the diffraction patterns presented in Figure 4.26 and 4.27, the scattering vector and the electric field vector are approximately parallel, *i.e.*, the enclosed angle ξ is zero. In order to assess the texture development under electric field, however, the diffraction data has to be investigated with varying ξ. For this purpose, the two-dimensional data obtained through the area detector is segmented into sectors each covering a 10 ° angular range in ξ. The diffraction data from 0 ° to 90 °, which was consolidated for every sector by means of rotational averaging, is presented in Figure 4.28 for a field of 6 kV·mm^{-1} and contrasted with the unpoled state. For y=0 a texture develops, meaning that both the $\{111\}_c$ and the $\{200\}_c$ reflections exhibit a clear variation in intensity and asymmetry on ξ. As demonstrated before, peak broadening and asymmetries are observed for 0 °. Both effects are diminished when ξ is increased. Eventually, no non-cubic distortion is observed for ξ=90 °. The occurrence of this texture suggests the presence of domains, *i.e.*, the establishment of a ferroelectric long-range order as introduced in Chapter 2. Similar to the composition BNT-20BKT, a texture is also evident in BNT-20BKT-2BZT, albeit slightly less pronounced. For y=0.04 and y=0.06, however, the sensitivity of the structure on the electric field is again diminished. The broadening in $\{111\}_c$ is minute for both compositions while the $\{200\}_c$ reflection is virtually independent from ξ.

4.3.6 Piezoresponse Force Microscopy

Interestingly, all investigated samples of the BNT-6BT-100yKNN material system are devoid of domains in the initial state but a DC bias field may induce domains depending on the KNN content.

It is well known from ferroelectrics that the domain structure exerts a decisive influence on the piezo- and ferroelectric properties.[178] Piezoresponse force microscopy allows for the observation and manipulation of domains on a submicroscopic scale and thus is an ideal investigation technique for BNT-based ceramics. BNT-6BT-100yKNN compositions with y={0; 0.01; 0.03; 0.09; 0.18} were examined by means of PFM to elucidate the microstructure along with the field and time dependence. Figure 4.29 presents the topography, in addition to the out-of-plane (OP) and in-plane (IP) piezoresponse amplitude, measured on the mirror-polished surfaces. All samples feature a generally densely sintered surface with few pores, represented by dark spots. The topography maps demonstrate that the surface roughness is low with deviations typically in the nanometer range. Some grains are distinguishable by slight variations of topography, which holds true especially for y=0.03. Moreover, the surface profiles for y=0.09 and y=0.18 reveal less contrast whose origin cannot be clearly ascertained.

The OP amplitude of BNT-6BT shows little contrast except for contrast due to topography crosstalk caused by pores. By comparison, the map of IP amplitude features a grainy and blurry contrast that affords a distinction of some grains. The lack of well-defined macroscopic domains is a clear difference to ferroelectrics like lead zirconate titanate (compare Figure A.2). For y=0.01 and y=0.03, the OP amplitude provides more contrast, hence, some grain boundaries are distinguishable. The IP amplitude map resembles the results obtained for BNT-6BT with little, mostly blurry and grainy contrast. With higher KNN contents, a grain-like contrast is found in both OP and IP

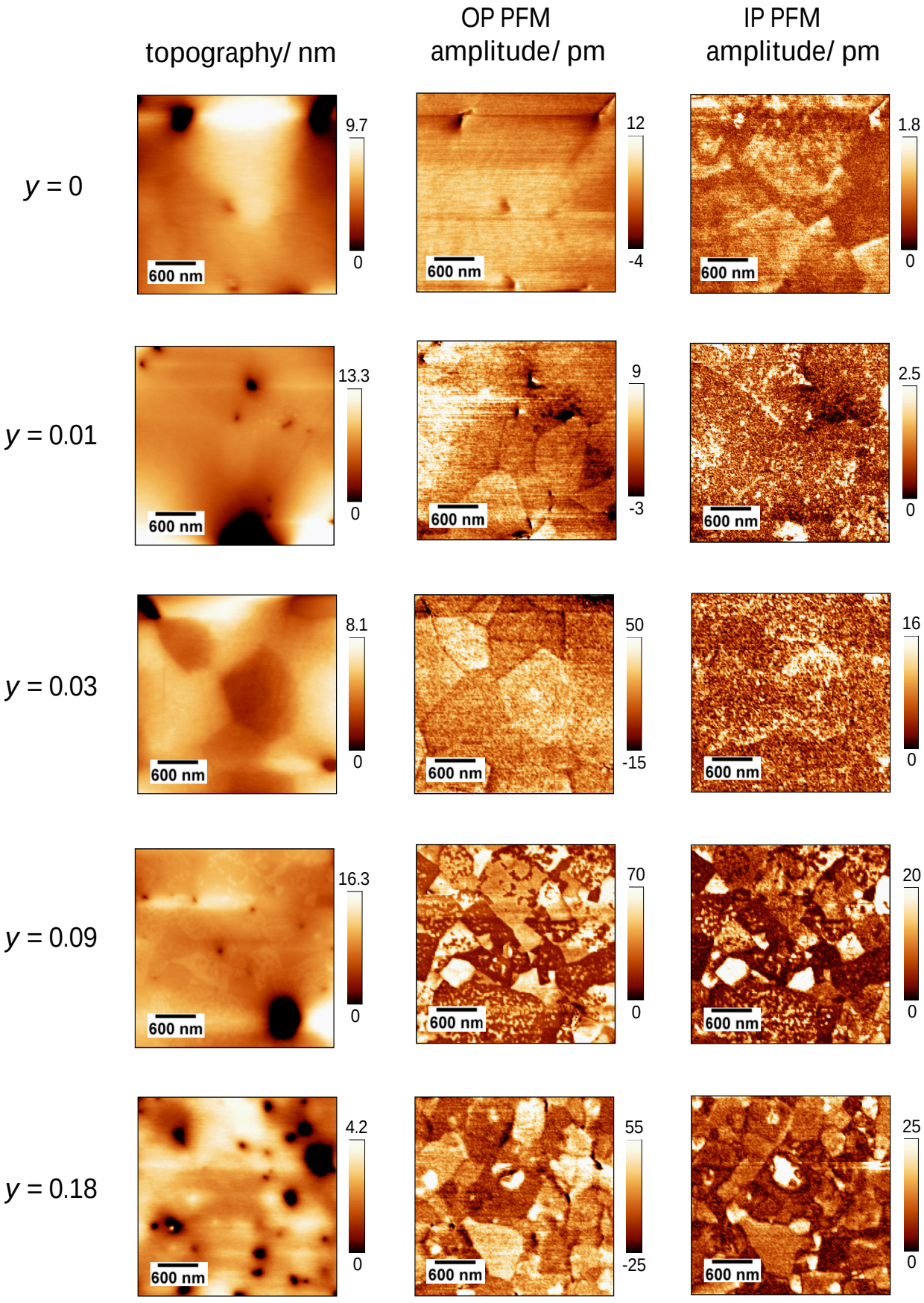

Figure 4.29: Topography in addition to out-of-plane (OP) and in-plane (IP) amplitude for BNT-6BT-100yKNN.

response as demonstrated for y=0.09 and y=0.18, although the observable features are not well formed.

One particularly valuable merit of the PFM technique is the ability to perform local poling experiments by applying a bias voltage to the tip while scanning a predefined area. In order to examine potential field-induced transitions a 3x3 µm^2 square in the center of the scanned area was poled with incrementally increasing negative DC voltages. After this first poling step another, likewise centrally located square of 1x1 µm^2 size was poled with a DC bias voltage of the same magnitude but inverse polarity. Out-of-plane piezoresponse maps of the unbiased surface are presented in Figure 4.30 together with maps after poling with $\mp$10 V and $\mp$20 V, respectively. The piezoresponse images for the virgin state support the observations outlined above with Figure 4.29, *i.e.*, no pronounced macroscopic domains for y={0; 0.01; 0.03} and a grain-like contrast for y=0.09 and y=0.18. For BNT-6BT the application of a $\mp$10 V DC voltage induces microscopic domains of converse piezoresponse and both squares are well-defined, *i.e.*, the outer contours are distinguishable across the majority of the circumference. At the same voltage, BNT-6BT-1KNN and BNT-6BT-3KNN exhibit domains as well, but these domains cover merely a fraction of the area that was previously exposed to the electric field. This effect of incomplete contrast in the piezoresponse is enhanced with increasing KNN content. Consequently, for y=0.09 and y=0.18, no domains can be induced. Increasing the bias voltage to $\mp$20 V affords the writing of complete domains in BNT-6BT-1KNN. With an increased voltage of 20 V, BNT-6BT-3KNN features domains that are, albeit still incomplete, enhanced in both size and contrast. Interestingly, the inner squares in BNT-6BT-1KNN and BNT-6BT-3KNN are more pronounced than the respective outer squares. This result is probably associated with the increased duration of the poling. In contrast to the outer area, the inner square is exposed twice as long to the electric field, namely during scanning with both negative and positive tip bias. The poling procedure furthermore requires that the inner area is poled subsequently to the poling treatment of the outer area. The piezoresponse of these materials, however, exhibits a notable time dependence and, therefore, the sequence of field exposure has an effect on the measured piezoresponse, as will be shown later. For BNT-6BT-9KNN and BNT-6BT-18KNN domains cannot be written with a bias voltage of 20 V. Even the highest applicable tip voltage of 40 V (not shown) is insufficient to create microscopic domains.

By measuring piezoresponse loops on distinct spots at the sample surface it is possible to characterize the ferroelectric switching behavior on a nanoscopic scale. For this purpose, band excitation voltage spectroscopy is applied in two sets of experiments. First, loops are measured for y={0; 0.01; 0.03; 0.09; 0.19} in a grid of 10x10 points spanning a 5x5 µm^2 area. In order to assess the representative switching behavior for each composition, the average hysteresis loop is calculated from the 100 individual curves. As illustrated by Figure 4.31 all five compositions feature a closed piezoresponse hysteresis of approximately rectangular shape. While BNT-6BT exhibits a slim loop, the addition of KNN causes a broadening of the piezoresponse loop, *i.e.*, the switching voltage U_{sw} increases with y. The switching voltage was determined for each composition from the average loop via fitting (Figure 4.32). For BNT-6BT U_{sw}=3.5 V, linearly increasing to 5.3 V for BNT-6BT-1KNN and 8.4 V for BNT-6BT-3KNN. A high switching voltage of 23.3 V and 27.4 V is determined for BNT-6BT-9KNN and BNT-6BT-18KNN, respectively. It is important to note

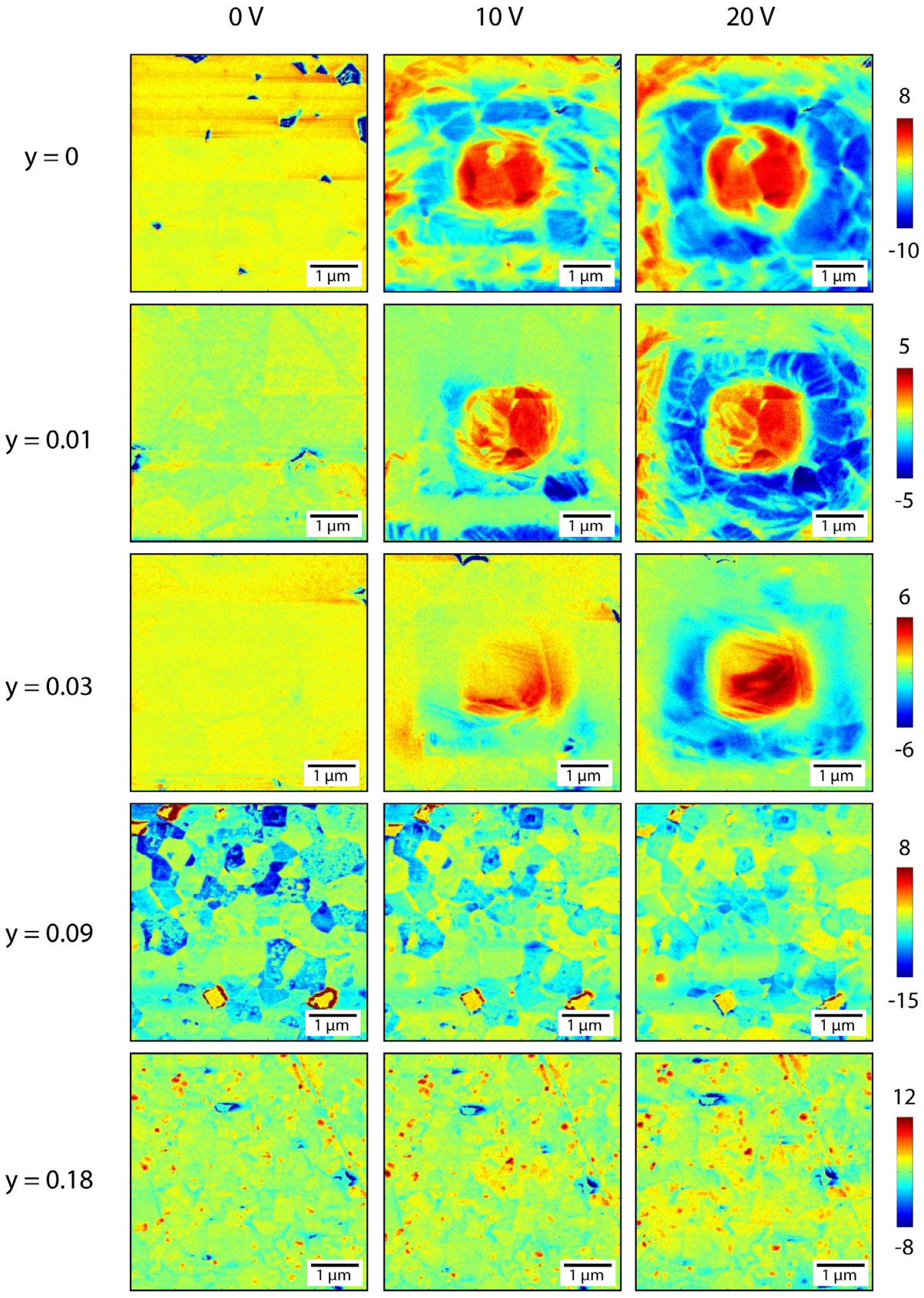

Figure 4.30: Out-of-plane piezoresponse for BNT-6BT-100yKNN at 0 V and after poling with $\mp$10 V and $\mp$20 V in a 3x3 µm^2 and 1x1 µm^2 square, respectively.

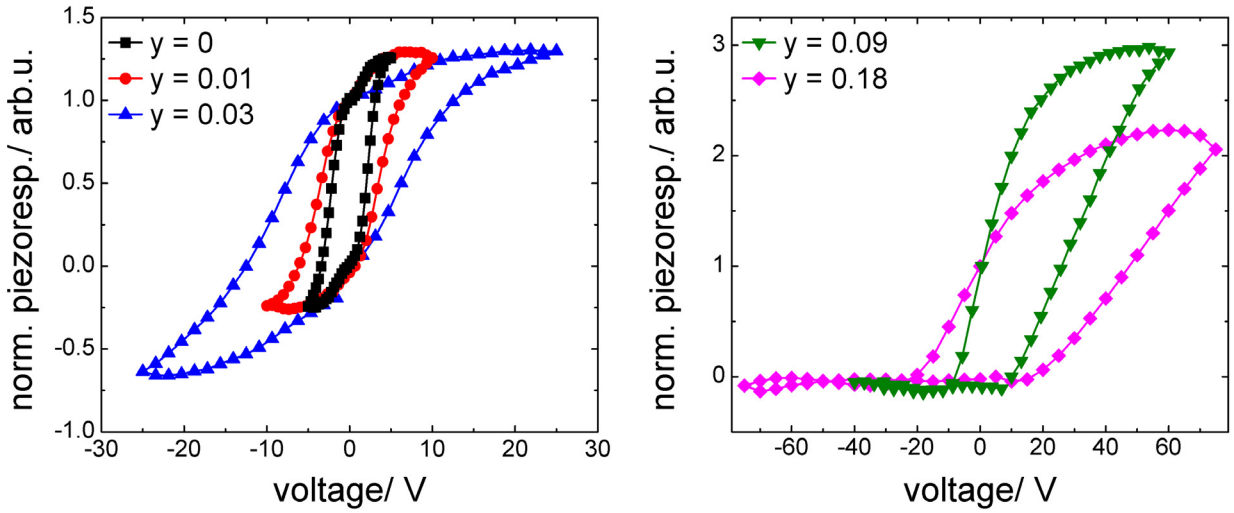

Figure 4.31: Locally measured piezoresponse loops for BNT-6BT-100yKNN with y={0; 0.01; 0.03; 0.09; 0.18}, measured in a 10x10 grid within a 5x5 µm^2 square.

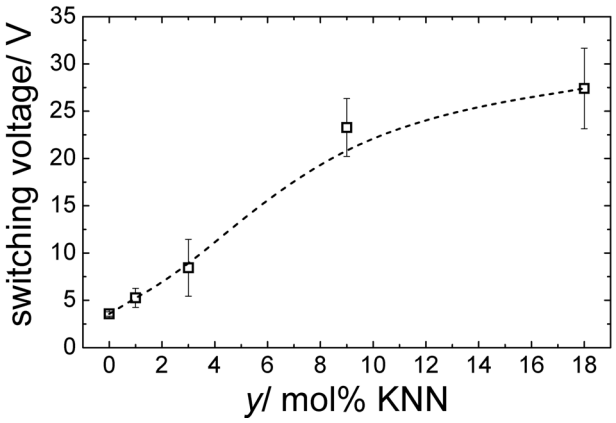

Figure 4.32: Switching voltage as determined by fitting of the averaged piezoresponse loops.

that the loops for these two compositions are not symmetric. The observation of a closed loop suggests that switching could be induced throughout all compositions on a macroscopic scale, provided the applied electric field is large enough. The calculation of quantitative values from the locally measured U_{sw} is highly difficult, mainly due to uncertainties arising from the tip-surface-junction. Consequently, it is not possible to deduce the electric field that is required for macroscopic switching. An estimation, however, is feasible by comparing the local switching voltage of 3.5 V and the macroscopic coercive field of 2.25 kV·mm^{-1} for BNT-6BT. Judging from these two values, the macroscopic switching field of BNT-6BT-9KNN and BNT-6BT-18KNN could be larger than 15 kV·mm^{-1}. An electric field of this magnitude notably exceeds the typical breakdown field of bulk samples, found to be approximately 8 kV·mm^{-1} for disc shaped specimens of 40 mm^3 volume. Therefore, the macroscopic $S(E)$ and $P(E)$ hystereses for y={0.03; 0.09; 0.18} display no or little switching.

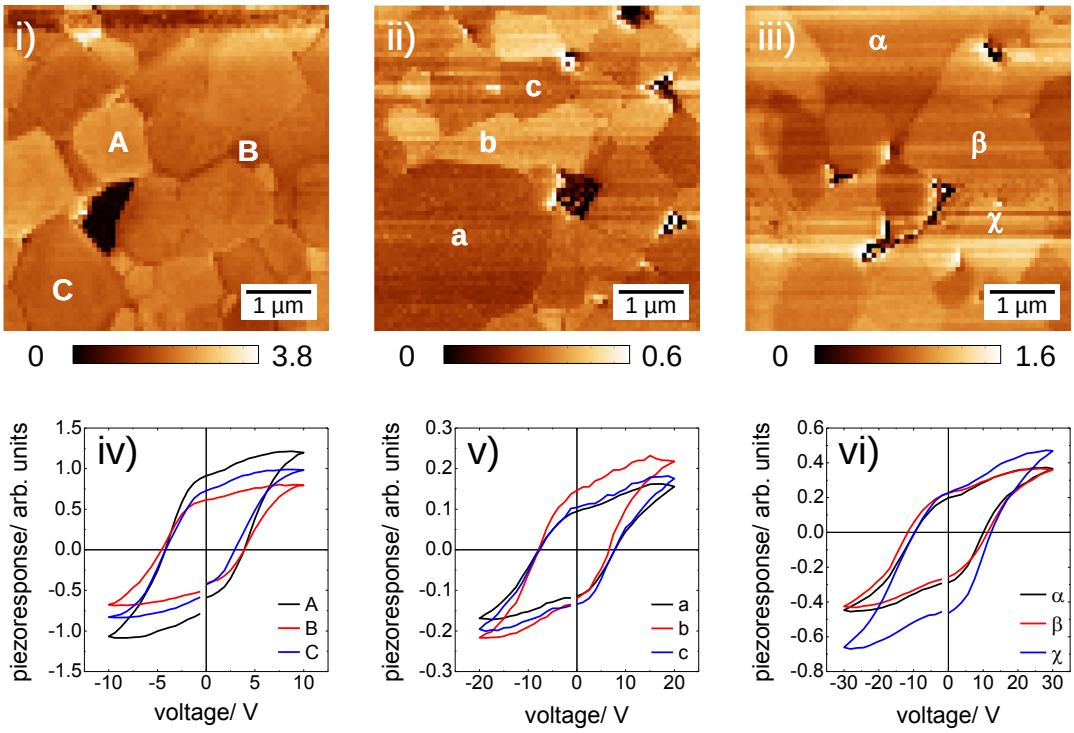

Figure 4.33: Top row: Mapping of the switching polarization P_{sw} determined from microscopic piezoresponse loops in a grid of 70x70 points within a 5x5 µm^2 area for BNT-6BT-100yKNN with i) $y = 0$, ii) $y = 0.01$, and iii) $y = 0.03$. Bottom row: piezoresponse loops for iv) $y = 0$, v) $y = 0.01$, vi) $y = 0.03$ measured in three distinct grains from an average of at least ten individual loops.

In the second set of voltage spectroscopy experiments, piezoresponse loops were measured across a much denser grid of 70x70 points in an equally sized 5x5 µm^2 area. The higher number of measurement points affords an investigation of the spatial variance of switching parameters. Owing to the required high switching voltages for y=0.09 and y=0.18 and the consequently decreased durability of the tip, high-density mapping was performed up to a maximum KNN content of y=0.03. The resulting 4-dimensional data array has to be reduced to three dimensions to allow the plotting of a color-coded two-dimensional map. Therefore, the difference in piezoresponse signal at zero-field is extracted from each of the 4900 individual loops. This difference, termed P_{sw} as a measure for the switching polarization, is presented for BNT-6BT, BNT-6BT-1KNN, and BNT-6BT-3KNN in Figure 4.33. As indicated by the lack of contrast, the spatial variation of P_{sw} within individual grains is very small, *i.e.*, the switching polarization is homogeneously distributed. There is, however, a difference in P_{sw} from grain to grain. Due to this intergranular contrast, the maps shown in Figure 4.33 provide insight into the microstructure, similar to polished microsections that had been subject to a contrasting method, such as thermal or chemical etching. In addition to intergranular contrast, BNT-6BT also exhibits a pronounced grain boundary contrast, demonstrated by the dark tone in-between grains (Figure 4.33 i)). By contrast, BNT-6BT-1KNN and BNT-6BT-3KNN do not feature this kind of pronounced contrast.

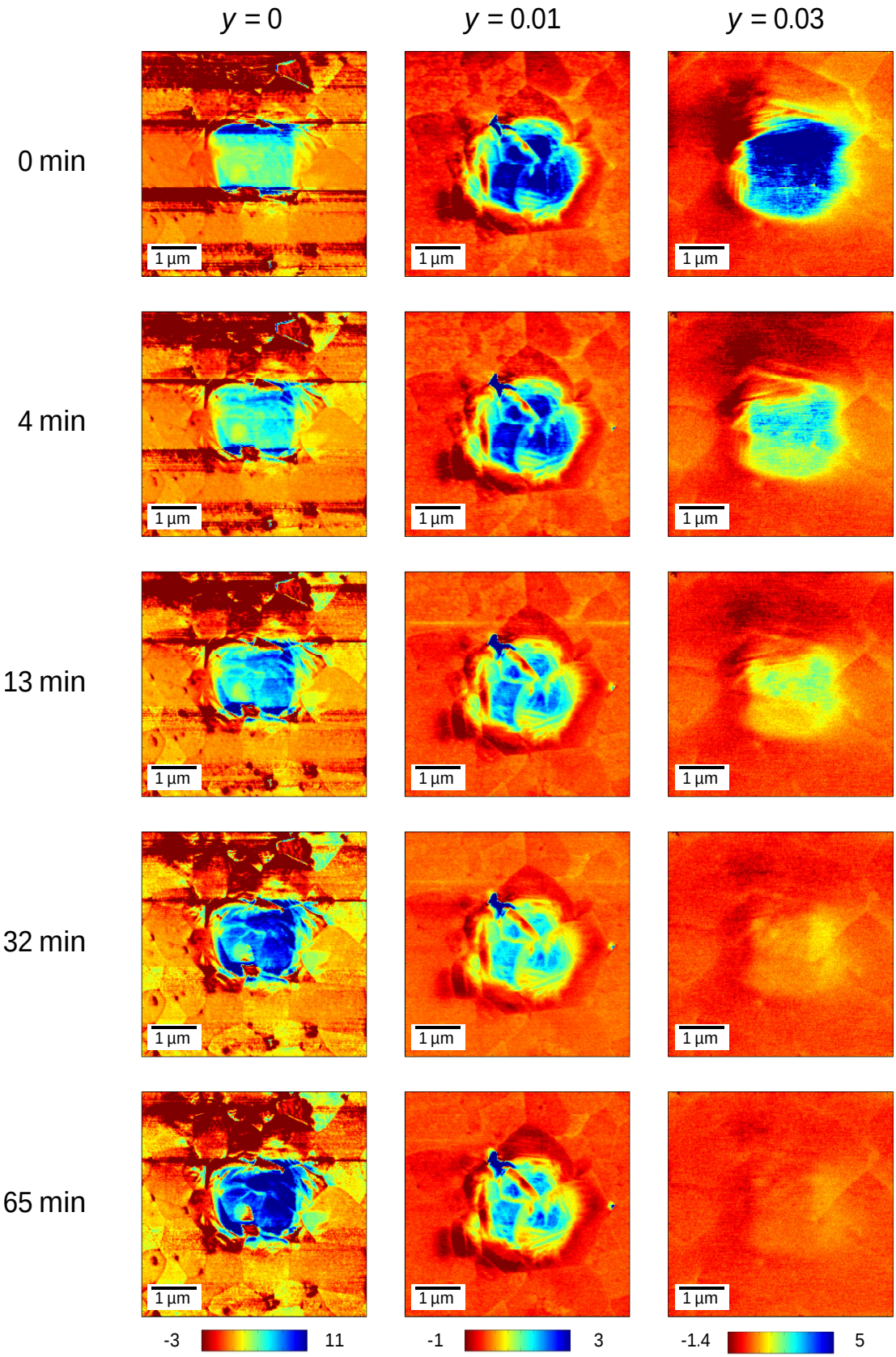

Figure 4.34: Maps of the piezoresponse after t={0; 4; 13; 32; 65} min for y={0; 0.01; 0.03} after poling a 1x1 μm^2 area in a 5x5 μm^2 square with -20 V_{DC}.

Unlike ferroelectrics such as PZT, BNT-6BT-100yKNN does not possess domains in the initial, unbiased state, as demonstrated earlier in Figure 4.29. Upon application of electric field, however, domains develop. The stability of this long-range ordered phase was further investigated as a function of time. For this purpose, a 1x1 µm^2 area was scanned with -20 V tip bias to create a domain. Subsequently, an enveloping 5x5 µm^2 square was repeatedly scanned to monitor the evolution of the piezoresponse with time (Figure 4.34). This experiment was conducted for y={0; 0.01; 0.03}; no domains could be induced for y=0.09 and y=0.18. The domain induced in BNT-6BT is persistent throughout the whole measurement period and the piezoresponse signal even slightly increases with time. Please note that the partially streaky appearance is caused by scanning in the single-frequency PFM mode across pores with a high scanning rate of 1 Hz, equivalent to 5 µm·s^{-1}. Rapid scanning is required to provide a sufficient time resolution. In contrast to BNT-6BT, the PFM signal for BNT-6BT-1KNN gradually decreases to approximately 50 % of the initial piezoresponse. After approximately 30 min the piezoresponse approaches this value and remains virtually constant. When the KNN content is increased to y=0.03, the piezoresponse within the induced domain decreases quickly. Eventually, the domain has nearly vanished 65 min after the poling process.

Interestingly, the poling experiments shown in Figures 4.30 and 4.34, both demonstrate that the induced domains notably exceed the 1x1 µm^2 area that was exposed to the electric bias field.

4.4 Discussion

4.4.1 Functional Properties

Large-Signal Properties of BNT-based Ternary Material Systems

It is hypothesized for BNT-6BT that an electric field induces a transition from a state of PNRs to a long-range ordered state with micro-domains. Increasing KNN content y eventually impedes this transition, yielding a slim $P(E)$ hysteresis and a sprout-shaped $S(E)$ curve. The novel lead-free material BNT-BKT-BZT exhibits very similar characteristics. Therefore, it is concluded that the observed field dependence can be generalized to the whole material class.

The large-signal properties of the model material BNT-6BT are revisited for a fixed frequency of 1 mHz and a fixed maximum field of 6 kV·mm^{-1}. The $S(E)$ and $P(E)$ curves presented in Figure 4.10 for BNT-6BT largely comply with earlier reports.[120,182] Initially, both hystereses appear to present typical ferroelectric behavior as introduced in Chapter 2.1.2, suggesting the presence of long-range order in the form of domains. In the past, BNT-6BT has been referred to as ferroelectric.[115] Close inspection of the $P(E)$ and $S(E)$ curves, however, reveals notable differences in comparison to conventional ferroelectrics.[16,19,38] A distinctive feature is the extraordinarily high remanent strain (0.38 %), which is considerably larger than in PZT[183] (0.16 %) or in BT[184] (0.047 %). Another distinguishing characteristic is the discontinuity in the slope of $P(E)$ at E_{sat} and the corresponding nearly discontinuous strain. This characteristic depicts a clear contrast to

PZT or BT where field-induced polarization increases more gradually. These two observations, large remanent strain and discontinuity in $P(E)$, support the assumption that the processes during first exposure to the electric field are not limited to mere domain switching and alignment.

Therefore, in the following discussion BNT-6BT will not be referred to as a ferroelectric but rather a relaxor ferroelectric. To support this, it is useful to reconsider the crucial features and prerequisites for relaxor behavior. As outlined in Chapter 2.1.3, the fundamental properties of relaxor ferroelectrics arise from the presence of small regions with locally correlated polarizations. These nanometer sized polar regions, referred to as polar nano-regions (PNRs), are embedded in a metrically cubic matrix. From a materials point of view, the assumption that the solid solution of BNT and BT is a relaxor ferroelectric appears plausible, considering the two individual end-members. The first composition that was found to exhibit relaxor properties is based on barium titanate, namely $BaTiO_3$-$BaSnO_3$.[45] The originally ferroelectric BT can be turned into a relaxor with relatively low amounts of heterovalent substitutions.[44] Replacing the A-, B- or oxygen-site of the perovskite lattice with ions of differing valence may easily induce relaxor properties, *e.g.*, in (1-x)$BaTiO_3$-$x$$NaNbO_3$,[185] (1-$x$)$BaTiO_3$-$x$La($Mg_{0.5}Ti_{0.5}$)$O_3$,[186] or Ba($Ti_{1-x}Li_x$)$O_{3-3x}F_{3x}$.[187] BNT was also reported to exhibit relaxor features such as a broad peak in permittivity[94] as well as a frequency dispersion[102] and PNRs in the form of nanoscale twin domains.[98] Therefore, it is reasonable to expect that BNT-6BT, as the solid solution of both compounds, also features relaxor properties, especially with regard to the mixed occupancy. A total of three heterovalent ions occupy the A-site, namely Ba^{2+}, Bi^{3+}, and Na^{+}. The mixed occupancy of the A-site induces charge and positional disorder. As demonstrated by inverse Fourier transformed images obtained via high-resolution TEM (HRTEM), BNT-6BT indeed consists of differently ordered regions.[188] These regions were of 10-20 nm size and could be distinguished from each other by the homogeneous contrast within each region. The authors stated that this observation may be rationalized by different chemical ordering or different crystal structures. Simulations within the same report, however, did not support the assumption of different chemical ordering, thus implying disorder. By contrast, for pure BNT, first-principles calculations based on density functional theory suggested that chemically ordered nano-regions embedded in a disordered matrix are energetically favorable.[189] These chemically ordered areas were suggested to explain the relaxor properties of BNT as they supposedly act as nucleation sites for PNRs.

For these reasons, BNT-6BT fulfills the necessary requirement of lattice disorder that is essential for relaxor behavior. As stated earlier the polarization and strain hystereses both strongly indicate the presence of ferroelectric domains, *i.e.*, domains with a size on the micrometer or submicrometer scale rather than the nanoscopic scale. This finding suggests that BNT-6BT is a nonergodic relaxor at room temperature and undergoes a field-induced transition towards a ferroelectric long-range ordered state. In the initially nonergodic state the PNRs cannot be considered as completely independent, isolated entities. Instead, ergodicity is broken, resulting in a correlation among the PNRs through the host matrix. In the virgin, unbiased state the sum of all individual polarizations $\sum P_i$ is zero and the material does not exhibit piezoelectricity.

This NE phase is then converted into a FE phase upon the application of an electric field. It is well known from lead-containing relaxor ferroelectrics such as PMN[63] or PLZT,[190] that a ferroelec-

tric long-range ordered phase can be induced either by field cooling (FC) or via application of an electric field after zero-field cooling (ZFC) to a nonergodic state. In both cases the field is required to surpass a threshold value E_{th}, whereas the electric field after ZFC is always higher than during FC.[75] It will be shown in a subsequent section that the bending in the $P(E)$ loop around E_{sat} involves changes of the average structure and the establishment of a domain texture. In addition, it was recently shown that the bend in $P(E)$ is associated with a minimum in the volume strain and a formation of domains as observed by *in situ* TEM.[191] For BNT-6BT the critical field after ZFC is located around 2.2 kV·mm^{-1}. At this field, the formerly nanoscopic polar regions are hypothesized to transform into domains of microscopic size, percolating the sample. A steep increase in strain and polarization precedes this transformation. For example, the field of inflection in the $S(E)$ curve is $E_{inflection}$=2.1 kV·mm^{-1}. As soon as the transformation is accomplished, an increase in the electric field causes a further alignment of domains, just like in an ordinary ferroelectric. As a consequence, $P(E)$ and $S(E)$ do not increase as rapidly as before. During further cycling, the hystereses of BNT-6BT are practically indistinguishable from a conventional ferroelectric, as the bend in the $P(E)$ curve at E_{sat} occurs exclusively in the first half-cycle.

Reports on the electrical properties of the solid solution BNT-100xBT vary and are still controversial. Numerous authors have reported phase diagrams for BNT-100xBT,[124,125,182,192,193,194,195] which implies that the physical properties of BNT-6BT are sensitive to variations in processing conditions, *e.g.*, thermal treatment, exposure to electric field, and aging period. The reason for this discrepancy in properties may be attributed to the metastability of the nonergodic relaxor phase.[43] The equilibrium state is not reached within accessible laboratory time scales due to the large relaxation times. Consequently, different states are achieved, depending on the external conditions. For example, Zang *et al.*[196] demonstrated that the dielectric properties of BNT-6BT depend decisively on the annealing treatment.

When KNN is added, the large-signal behavior remains to a great extent qualitatively unchanged for y=0.01, *i.e.*, BNT-6BT-1KNN represents a nonergodic relaxor in the virgin state that is converted to a relaxor ferroelectric under the influence of an electric field. The threshold field for the transition increases slightly as $E_{inflection}$ and E_{sat} increase to 2.2 kV·mm^{-1} and 2.4 kV·mm^{-1}, respectively (Figure 4.11 c)). This finding can be rationalized considering the substitutional disorder that is introduced with KNN; the A-site occupancy is further diversified with four different ions. Moreover, mixed B-site occupancy is introduced as Ti^{4+} now shares the B-site with heterovalent Nb^{5+}. This increased substitutional disorder, in return, enhances the random electric fields that arise from charged compositional fluctuations.[76] As a consequence, the external electric field that is required to establish long-range order increases. Interestingly, the coercive field slightly decreases. This finding suggests that, when the ferroelectric order is established, polarization reversal by domain switching is facilitated, *i.e.*, the domain wall mobility is enhanced.

According to Figure 4.10, the addition of 1 mol% KNN also affects the maximum attainable value for both polarization and strain. Note that the maximum polarization of the end-member KNN at 6 kV·mm^{-1} is with 0.2 C·m^{-2} notably lower than for BNT-6BT.[197] Considering the low concentration of KNN, however, the drop in P_{max} by 16 % is remarkably high and disproportional. Hence, it is concluded that the observed decrease is not a result of a simple 'dilution' of properties. Rather, it

can be assumed that the decline in maximum polarization is associated with the increased disorder. In a study on the thermal evolution of $P(E)$ for the relaxor ferroelectric PLZT 12/40/60, a similar decrease was observed not as a function of composition but as a function of temperature.[198] The authors rationalized this finding with the decreased volume fraction of local polar regions. Consequently, it is suggested that the addition of 1 mol% KNN and the associated compositional disorder result in a decrease in the volume fraction of PNRs. As evidenced by the high remanent strain, the long-range order can still be induced from the metastable nonergodic phase, albeit at a higher electric field. Polarization of BNT-6BT-1KNN, however, is reduced throughout the whole field range, indicating that the fraction of polar regions and domains remains diminished in comparison to BNT-6BT. As will be discussed later, there is a strong correlation between strain and polarization and, therefore, the decline in P_{max} involves a decrease in the poling strain S_{pol}. The repeatedly accessible strain S_{max} increases due to the decrease in remanent strain.

When the KNN content is increased to y=0.03, the electrical properties are fundamentally altered. The $P(E)$ loop exhibits an S-shape rather than the rectangular shape for y=0 and y=0.01. Obviously, the increased disorder has a dramatic effect on the inherent configuration of the nanoscopically distributed polar phase and its stability. The critical threshold field increases notably, as indicated by E_{sat}=3.3 kV·mm^{-1} , and P_{max} is further diminished. From the change in slope of $P(E)$ at E_{sat} it is concluded that the transition from relaxor to a long-range order still takes place. This long-range order, however, is not stable, partly collapsing with a decrease of the electric field as denoted by the sudden drop in $P(E)$. When the negative electric field reaches the value of E_{sat}, the long-range order is re-established. Therefore, other than for y=0 and y=0.01, the bend in the $P(E)$ loop is observed not only in the first but every half-cycle. Long-range order is repeatedly established but collapses when the value of the electric field approaches zero. Therefore, it is concluded that BNT-6BT-3KNN is not a nonergodic relaxor like BNT-6BT but rather an ergodic relaxor. At room temperature, the establishment of a stable FE phase by application of an electric field is impeded. The quenched random fields have a destabilizing effect and eventually destroy the long-range order when the electric field is removed, retrieving the predominantly nano-sized domains. The direction of the dipole moment of the PNRs is largely random as it is governed by the quenched random fields and as a consequence, polarization drops. As will be discussed in a later chapter, the relaxation mechanism is indeed observed on the nanoscale and can be assessed by means of PFM measurements.

Figure 4.35 further illustrates the peculiar field-induced behavior by means of the slope of the $P(E)$ loop, which is sometimes interpreted as a large-signal permittivity.[199] The polarization drops sharply within a narrow field range with an inflection point at approximately 0.3 kV·mm^{-1}. The resultant double-loop-like $P(E)$ hysteresis with a low P_{rem} of 0.08 C·m^{-2} resembles the polarization loops reported for PMN. In this canonical relaxor the double hysteresis feature occurs at approximately -70 °C and is rationalized as the interplay between the field-induced ferroelectric phase conversion and the re-conversion to the relaxor state.[200] It is furthermore interesting to note that the authors explicitly state that the double-loop is not related to antiferroelectric order. A double-loop polarization hysteresis is also observed in other relaxors like $Pb(Sc_{1/2}Ta_{1/2})O_3$ (PST),[201] $Pb(Sc_{1/2}Nb_{1/2})O_3$ (PSN),[202] PLZT,[198] PMN-PSN,[203] and PMN-PT[204].

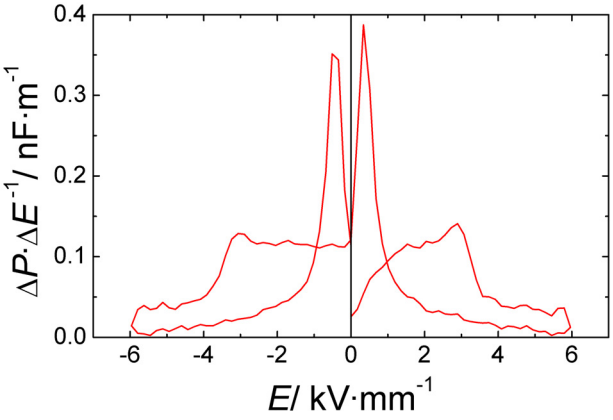

Figure 4.35: Slope $\Delta P{\cdot}\Delta E^{-1}$ of the $P(E)$ curve for BNT-6BT-3KNN.

Due to the repeated establishment and subsequent collapse of long-range order the poling strain is large while remanent strain is practically zero. Therefore, the effective strain S_{max} nearly equals S_{pol} and consequently high strokes can be harvested during each single cycle. By contrast, S_{max} of BNT-6BT is limited by a large S_{rem}. This interrelation between high achievable S_{max} and low S_{rem} has also been demonstrated by Jo *et al.*.[149] As this strain mechanism is inherently different from that one found in ferroelectrics, practically no negative strain is observed. In ferroelectrics, the negative strain is caused by domain nucleation and domain wall motion during polarization reversal.[205,206] In the present material the field-dependent behavior is not determined by aligned domains but by PNRs whose polarization vectors are largely random. Consequently, no negative strain can evolve. Following the figurative description 'butterfly curve' for a typically ferroelectric $S(E)$ curve, the strain hysteresis described here with little to no remanent and negative strain will be referred to as 'sprout curve'[207] throughout the following discussion.

The non-zero remanent polarization of BNT-6BT-3KNN indicates that the polarization vectors of the polar volume fractions are still at least partially aligned and not completely randomized. From this observation it is conjectured that PNRs and micron-sized domains potentially coexist in this state. It was concluded from dielectric measurements in $Ba(Ti_{0.675}Zr_{0.325})O_3$ (BTZr) that two sets of polar regions coexist below the freezing temperature T_f, namely static and dynamic ones.[208] There are weak interactions between dynamic PNRs, which are thought to behave like an ergodic species. By contrast, the static polar regions are notably bigger and thermal fluctuations are not sufficient to reorient their dipole moment since the activation energy for flipping of dipole moments is approximately proportional to the volume of the PNR.[47] These large static domains are consequently associated with nonergodicity, allowing ergodicity and nonergodicity to coexist in BTZr. A similar concept was proposed for the bismuth-based lead-free compound 0.78BNT-0.22BKT, which was modified with $LaFeO_3$.[209] From the relaxation of polarization and strain the authors concluded a mixture of ergodic and nonergodic phases at room temperature. Similarly, Wang *et al.*[78] concluded the existence of a precursory state with partially frozen PNRs from phase field simulations. Consequently, it is hypothesized that, in certain temperature ranges, ergodic and nonergodic phases may likewise coexist in BNT-6BT-100yKNN.

A further increase in the KNN content increases the ergodicity due to enhanced compositional disorder and likewise enhanced quenched random electric and elastic fields. For y=0.09 the long-range ordered state can no longer be induced by the application of an external electric field. The correlation length of the majority of the PNRs remains in the nanometer range. At the same time, the decreased P_{max} indicates that the fraction of polar volume is further decreased. Instead of a squared or double-loop shape, the $P(E)$ loop is of slim, almost elliptical appearance. The hysteretic behavior, represented by the integral area, decreased. There are different contributions to the dissipated energy during cycling. According to Hall,[15] the losses result from extrinsic effects such as the vibration and translation of domain walls and the switching of polarization directions. The observation of a slim loop, therefore, supports the hypothesis that the polar volume fraction is diminished and that comparably few micron-sized domains exist. The PNRs are aligned by a high external field, yielding sizable polarization. Upon removal of the field the PNRs revert to their mostly random orientations.

The $S(E)$ loop of BNT-6BT-9KNN exhibits a parabola shape with little hysteresis. Thus, the obtained $S(E)$ curve resembles strain loops measured for the relaxor PMN, which is ergodic at room temperature,[210,211] or PLZT 7.5/65/35 at elevated temperatures, where it is likewise ergodic.[212] In the final composition with y=0.18 the trend is continued, *i.e.*, the maximum values as well as remanence and hysteretic behavior further decrease.

The parabolic shape of $S(E)$ found for y=0.09 and y=0.18 indicates that strain is in a first approximation proportional to the square of the electric field. As the polarization dependence on the electric field is relatively linear, strain is proportional to polarization squared. This relation is presented in Figure 4.36. As described in Chapter 2, the linear relationship between strain and polarization squared is referred to as electrostrictive behavior. According to Figure 4.36, the relation $S_i = Q_{ij}P_j^2$ is fulfilled for BNT-6BT-9KNN and -18KNN. According to Damjanovic,[213] deviation from the perfectly linear $S(P^2)$ curve progression can be interpreted as evidence of the extrinsic contribution from PNRs due to their motion and switching.

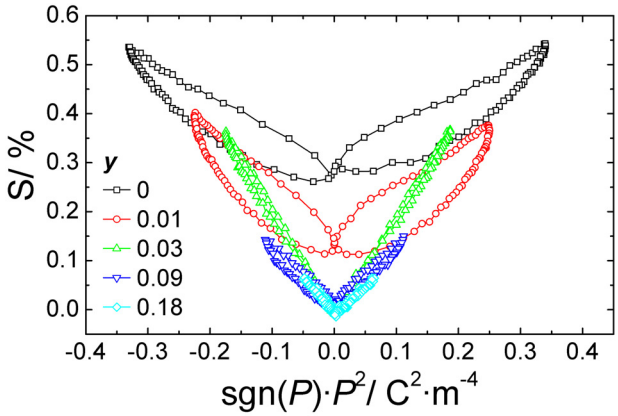

Figure 4.36: Strain as a function of polarization squared measured at 1 mHz and an amplitude of 6 kV·mm^{-1} for BNT-6BT-100yKNN with y={0; 0.01; 0.03; 0.09; 0.18}. Note that the curves are translated according to their respective remanent strain.

Considering the significantly nonlinear curve progression of both $P(E)$ and $S(E)$ for BNT-6BT-3KNN, it is remarkable that the linear relation between S and P^2 holds true also for this composition. This finding, however, is not unusual. The electrostrictive relation (Equation 2.7) also applies for ferroelectric soft PZT under both high temperatures[214] and high compressive stress[215], despite the likewise nonlinear curve progression of $P(E)$ and $S(E)$. The longitudinal electrostrictive coefficients were determined as $2.0 \cdot 10^{-2}$ m^{4}C^{-2} for y=0.03 and $1.2 \cdot 10^{-2}$ m^{4}C^{-2} for y=0.09 and y=0.18. These values, in particular the former, are sizable and can be compared to other relaxor ferroelectrics that are long known to exhibit high Q_{ij} values.[13] In general, the large electrostrictive values in relaxors are rationalized with the dipoles of the PNRs that give rise not only to large polarization but also large electrostrictive strains.[216] Table 4.1 lists the measured Q_{11} values of various ceramic electrostrictors for comparison.

Table 4.1: Electrostrictive coefficient Q_{11} for BNT-6BT-100yKNN with y={0.03; 0.09; 0.18} in comparison with well-studied lead-containing relaxor ferroelectrics.

material	Q_{11}/ 10^{-2} m^{4}C^{-2}	reference
BNT-6BT-3KNN	2.0	this work
BNT-6BT-9KNN	1.2	this work
BNT-6BT-18KNN	1.2	this work
PMN	2.3	[211]
SBN61:39 (120 °C)	2.7	[47]
PLZT 9.5/65/35	2.6	[217]
PMN-0.1PT	2.1	[210]
0.85PZN-0.1BT-0.05PT	1.8	[218]
BNT-6BT-18KNN	2.7	[174]

Interestingly, the Q_{11} of commercially available PMN and PMN-0.1PT is similar to that of BNT-6BT-3KNN. Zhang *et al.*[174] reported the qualitatively equivalent electrostrictive behavior for BNT-6BT-18KNN, however, provided a notably higher Q_{11} of $2.7 \cdot 10^{-2}$ m^{4}C^{-2}. The reason for the discrepancy may arise from a range of different reason. As outlined earlier, the properties of relaxor materials are sensitive to the processing and, therefore, differences may arise from distinct electrical or thermal treatment. Moreover, the authors utilized not only a higher field amplitude of 8 kV·mm^{-1} but, more importantly, a higher frequency of 50 mHz compared to approximately 1 mHz in this work. As will be demonstrated later, the electrostrictive coefficient depends on the measurement frequency, particularly in the case of a predominantly ergodic relaxor, where a higher frequency yields higher values for Q_{11}.

In order to check whether the results obtained from the BNT-BT-KNN system can be generalized, the results can be compared against the second BNT-based pseudoternary system, BNT-BKT-BZT. According to Figure 4.12, there is a range of common features in both systems. First, the base compound BNT-20BKT, just like the analog BNT-6BT, exhibits a ferroelectric-like behavior with a rectangular polarization loop and a butterfly-shaped strain hysteresis. The $P(E)$ loops exhibit a bend, albeit at a higher E_{sat} of 4 kV·mm^{-1}, and a nearly discontinuous strain with an $E_{inflection}$

of 3.3 kV·mm^{-1}, eventually resulting in a high remanent strain of 0.2 %. Both loops consequently suggest that BNT-20BKT is a nonergodic relaxor that undergoes a field-induced transition to a long-range ordered state beyond a critical field of the order of 3.5 kV·mm^{-1}. For small changes in the BZT content, the changes in $P(E)$ and $S(E)$ are minute. For $y \geq 0.04$, however, the long-range ordered state can no more be induced. The $P(E)$ loop is slim with low P_{rem} and the $S(E)$ loop features the sprout shape with virtually no remanent strain. Therefore, BNT-20BKT-4BZT is a predominantly ergodic relaxor, similar to BNT-6BT-3KNN.

It was found that, depending on y, the applied maximum field has a tremendous effect on the observed electromechanical behavior of BNT-19BKT-100yBZT (Figure 4.19). Up to 2 kV·mm^{-1}, strain and polarization are almost the same irrespective of BZT content. The required field to establish long-range order throughout the sample is not reached for either of these compositions as indicated by virtually zero remanent strain. Therefore, none of the $S(E)$ loops exhibits a butterfly shape lacking switchable micron-sized domains. A sizable S_{rem} in the predominantly nonergodic BNT-19BKT-2BZT is established only for fields $E \geq 4$ kV·mm^{-1}. The increase in BZT content consequently increases the required electric field, *i.e.*, the establishment of a notable S_{rem} in BNT-19BKT-3BZT necessitates fields higher than 5 kV·mm^{-1}. Finally, no stable long-range order can be induced in BNT-19BKT-4BZT for fields up to 6 kV·mm^{-1}. The establishment of long-range order actually limits the achievable maximum strain at very high fields due to high S_{rem}, demonstrated by the flattening of the $S_{max} \cdot E_{max}^{-1}$ curve as a function of maximum electric field in Figure 4.20 d). Within the observed range of y, a higher BZT content yields higher attainable $S_{max} \cdot E_{max}^{-1}$ values, even though only at highest electric fields.

The similarities between both systems, BNT-BT-KNN and BNT-BKT-BZT, are remarkable considering that the underlying chemistry is significantly different. This may indicate that the constitutive electromechanical characteristics of the pseudoternary systems are to a great extent inherited from the main compound BNT. The drastic change that is induced with increasing content of the ternary component, denoted with y, is not so much a consequence of the electrical properties of the respective end-member, in the present case KNN or BZT, themselves. Rather, it is the result of the substitutional disorder that is introduced through them. For this reason, numerous complex pseudobinary and -ternary perovskites systems have been reported recently, exhibiting comparable features to the presented material systems. Table 4.2 lists some of these systems along with the critical content in y where the $S(E)$ loop was found to exhibit a sprout shape with the normalized strain $S_{max} \cdot E_{max}^{-1}$ peaking. This list demonstrates that a large variety of ions is able to cause a transition into the predominantly ergodic phase, eventually yielding giant strains. Actually, in the case of 0.78BNT-0.22BKT the addition of 3 mol% of either Nb, Hf, or Zr yields very similar results. Thus, it can be conjectured that the ergodic phase can be induced by practically every ion, provided the ion meets the requirements in terms of size and charge so that a stable perovskite can be formed. The choice of respective ions may, however, affect the required threshold field and the achievable maximum polarization and strain values.

Therefore, both systems, BNT-BT-KNN and BNT-BKT-BZT, are comparable from the viewpoint of large-signal properties because the fundamental mechanisms are suggested to be the same.

Table 4.2: Overview on some reported BNT-based pseudobinary and -ternary systems. The critical y denotes the composition where large normalized strain $S_{max}{\cdot}E_{max}^{-1}$ is obtained due to the loss of remanent strain. Note that the entries are listed in chronological order according to the date of publication with the exception of the first two systems.

material	critical y	$S_{max}{\cdot}E_{max}^{-1}$ / pm·V^{-1}	E_{max} / kV·mm^{-1}	f/ Hz	Ref.
BNT-6BT-100yKNN	0.03	611	6	0.001	this work
BNT-20BKT-100yKNN	0.04	560	6	1	this work
(0.94-y)BNT-0.06BT-yKNN	0.02	560	8	0.05	[144]
(1-y)BNT-$y$$SrTiO_3$	0.28	488	6	0.1	[111]
(1-y)(0.94BNT-0.06BT)-yTa	0.02	600	6	0.3	[219]
(1-y)BNT-$y$$KNbO_3$	0.08	498	9	0.1	[132]
(1-y)BNT-$y$$Ba(Al_{1/2}Sb_{1/2})O_3$	0.045	532	9	0.1	[220]
(1-y)BNT-$y$$Ba(Al_{1/2}Nb_{1/2})O_3$	0.055	533	9	0.1	[221]
$Bi_{0.5}(Na_{0.78}K_{0.22})_{0.5}(Ti_{1-y}Zr_y)O_3$	0.03	614	7	0.3	[222]
(1-y)(0.8BNT-0.2BKT)-$y$$BiAlO_3$	0.05	391	7	0.1	[164]
$Bi_{0.5}(Na_{0.78}K_{0.22})_{0.5}(Ti_{1-y}Hf_y)O_3$	0.03	475	8	0.3	[223]
$Bi_{0.5}(Na_{0.78}K_{0.22})_{0.5}(Ti_{1-y}Nb_y)O_3$	0.03	641	7	n/a	[224]
(0.935-y)BNT-0.065BT-$y$$SrTiO_3$	0.22	490	4	0.5	[158]
(1-y)(0.8BNT-0.2BKT)-$y$$SrTiO_3$	0.03	600	6	0.5	[166]
(1-y)BNT-$y$$Ba(Al_{1/2}Ta_{1/2})O_3$	0.045	448	8	10	[225]

Knowledge gained from investigation of one of the two systems may very well apply not only to the respective other system but to the whole class of lead-free piezoceramics that incorporate a BNT-based morphotropic composition like BNT-6BT or BNT-20BKT. The following inspection of the small field properties under bias field will underpin this hypothesis further. There are, however, also differences as will be demonstrated later by *in situ* diffraction studies on BNT-20BKT-100yBZT under electric field.

Small-Signal Properties as a Function of Electric Bias Field

The in situ *measurement of ε and d_{33} as a function of electric bias field provides further insight into the effect of an electric field. Combining both affords a discussion about the domain state and the evolution with electric field. In contrast to nonergodic compositions the ergodic materials with high y feature sizable piezoelectric effects only under high electric fields and are, therefore, termed 'incipient piezoceramics'. The curve progression of $\varepsilon_{r,33}(E)$ suggests that the electric field gives rise to a coalescence and alignment of PNRs that subsequently collapse after the removal of the electric field.*

The small-signal properties, *i.e.*, the piezoelectric coefficient d_{33} and the relative permittivity $\varepsilon_{r,33}$, were shown in Figure 4.14 for BNT-6BT-100yKNN and in Figure 4.16 for BNT-20BKT-100yBZT. The experimental results will first be discussed for the BNT-6BT-100yKNN system. From Figure 4.14 it is apparent that the permittivity measured at 1 kHz varies in a strongly nonlinear, hysteretic

manner under the electric field. A small electric field causes an increase in $\varepsilon_{r,33}$ throughout all compositions, which may be rationalized with either the formation of new PNRs in previously pseudocubic sample volume or growth of existing PNRs. For y=0 and y=0.01, a further increase of the electric field results in the coalescence of PNRs into micron-sized domains. Therefore, the domain wall density is drastically diminished, causing a drop in $\varepsilon_{r,33}$. When the electric field is reduced again, the permittivity increases until it peaks in the vicinity of $\mp E_c$. This maximum is rationalized with the nucleation of domains that increase the domain wall density and $\varepsilon_{r,33}$. In contrast to soft PZT[226] or PLZT[227] the peak is comparably flat and broad. Interestingly, the $\varepsilon_{r,33}(E)$ curves strongly resemble loops measured on soft PZT under uniaxial compressive stress[228] or La-doped PZT in the fatigued state after bipolar cycling.[229] This similarity suggests that, like in PZT under stress or fatigued PZT, the domain walls are impeded in their mobility, eventually yielding a broader distribution of switching fields. Beyond that peak, the domain wall mobility diminishes because of a clamping effect that is caused by strain mismatch of switched domains and the associated elastic fields.[230] The decay of domain mobility counteracts the effect of the increased domain wall density and, consequently, $\varepsilon_{r,33}(E)$ decreases.

Initially BNT-6BT-3KNN behaves similarly to compositions with y=0 and y=0.01, *i.e.*, a slight increase in $\varepsilon_{r,33}$ for small fields and a pronounced drop for higher electric fields due to the coalescence of PNRs to larger domains. Subsequently, when the electric field is reduced, the permittivity increases at a higher rate than for y=0 and y=0.01. This rapid increase can be explained by the fragmentation of the micron-sized domains into PNRs. The final zero-field permittivity after one full cycle is hardly discriminable from the permittivity measured in the virgin state, in contrast to BNT-6BT and BNT-6BT-1KNN. Therefore, the domain state in BNT-6BT-3KNN after one cycle must be similar to the initial state.

Finally, the $\varepsilon_{r,33}(E)$ curves for y=0.09 and y=0.18 assume the shape of an inverted parabola with nearly no hysteresis. A similar decrease in permittivity with bias field has also been reported for the lead-containing relaxors PMN[231] and PMN-PT[232]. For PMN-0.1PT, it was observed that permittivity decreases quadratically. This finding was explained with the field-induced alignment of the dipole moments of the PNRs, resulting in a saturation of the polarization and a consequential decrease in the dielectric response. Compared to BNT-6BT-9KNN, the permittivity of BNT-6BT-18KNN decreases at a lower rate with the electric field, indicating that the alignment of the PNR polarization directions requires higher electric fields. In both compositions, the permittivity before and after exposition to the electric field is practically identical, owing to ergodicity.

The curve progression of d_{33} for y=0 and y=0.01 depicted in Figure 4.14 reflects the well-known behavior measured in other ferroelectrics or nonergodic relaxors.[227,229,233] Due to the flat curve progression of $\varepsilon_{r,33}(E)$, the d_{33} loops strongly resemble the respective $P(E)$ loops since the piezoelectric coefficient and the permittivity are interrelated according to the following equation.[6]

$$d = 2Q \cdot \varepsilon \cdot P \tag{4.6}$$

Even though this equation is strictly speaking only valid for the single-domain state of a single-crystal, it is often applied to polycrystals to illustrate that permittivity, polarization, and the piezoelectric coefficient are closely interrelated. Interestingly, $d_{33,6}$ of BNT-6BT-3KNN reaches a value

of 165 pC·N^{-1}, while the same material shows merely 46 pC·N^{-1} under zero-field. Since this material exhibits sizable and practically useful piezoelectric properties only under high electric field, Jo *et al.* [207] coined the novel term 'incipient piezoceramics' for this group of materials.

The compositional evolution of small-signal properties for BNT-20BKT-100yBZT (Figure 4.16) under bias field is to a great extent comparable to BNT-6BT-100yKNN. For low y, the d_{33} and $\varepsilon_{r,33}$ curves exhibit ferroelectric-like behavior. The maximum d_{33} of BNT-20BKT at 6 kV·mm^{-1} is slightly higher with 143 pm·V^{-1} compared to 134 pm·V^{-1} in BNT-6BT. The zero-field value of 141 pm·V^{-1}, however, is smaller than for BNT-6BT, which exhibits 165 pm·V^{-1}. In addition, the characteristic bend in $P(E)$ at E_{sat}=3.7 kV·mm^{-1} is higher with respect to BNT-6BT, which features an E_{sat} of 2.25 kV·mm^{-1}. In the BNT-20BKT-100yBZT system, the maximum $d_{33,6}$ was found for y=0.04 with 194 pm·V^{-1}. By contrast, the BNT-6BT-100yKNN system displayed a $d_{33,6}$=178 pm·V^{-1} at y=0.09. Both compositions are incipient piezoceramics with a sizable d_{33} under high electric fields and diminished macroscopic piezoelectric effect under zero-field. The evolution of the field-dependent permittivity is also comparable as low BZT or KNN contents both yield $\varepsilon(E)$ curves with two maxima while high BZT or KNN contents yield slim curves with little hysteresis.

Therefore, the two material systems share great similarities in their electromechanical characteristics under electric field in regard to both large- and small-signal properties. This finding underpins the hypothesis that, despite distinct chemical composition, there are universally valid trends in this group of ceramics of BNT-based pseudoternary material systems.

Frequency Dependence of Large-Signal Properties

The proposed mechanism of coalescence and fragmentation of PNRs during electrical cycling suggests a time dependence due to the kinetics assumed for these processes. Therefore, polarization and strain measurements at varying frequencies may shed light on this issue. It is demonstrated that the time dependence of the maximum values at 6 kV·mm^{-1} increases with the degree of ergodicity, which is coupled to the compositional disorder. For high y values the usable strain and the maximum polarization decrease notably with frequency.

As outlined in Chapter 4.3.4, the measurement frequency exerts a significant influence on the large-signal properties of lead-free piezoceramics depending on the respective composition. Figure 4.37 presents E_{sat} determined at different frequencies versus $E_{inflection}$.

The evolution of E_{sat} suggests that the field-induced transition is frequency-dependent, *i.e.*, the transition begins at lower electric field values for lower frequencies. For y=0.02, 6 kV·mm^{-1} suffices to convert the material into the FE phase, which results in practically frequency-independent S_{max} and P_{max}. By contrast, at lower fields the $S(E)$ curve exhibits a significant frequency dispersion, as, for example, at 4 kV·mm^{-1} strain is 0.3 % at 0.1 Hz and 0.07 % at 100 Hz in the first half-cycle. This suggests that the transition is close to completion for 0.1 Hz while 100 Hz would require a far higher field, namely 5.4 kV·mm^{-1} (Figure 4.37).

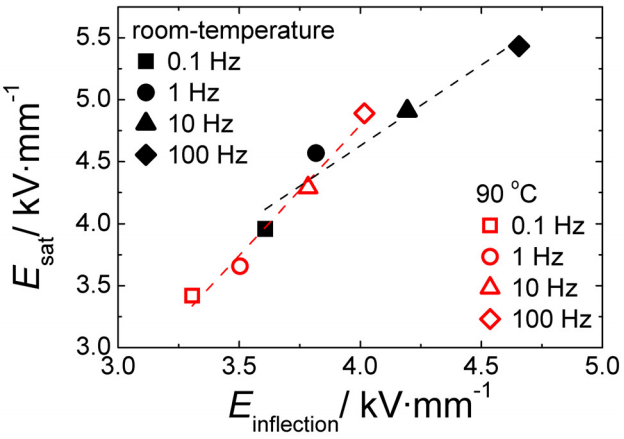

Figure 4.37: Interrelation of E_{sat} and $E_{inflection}$ for BNT-19BKT-2BZT at frequencies from 0.1 Hz to 100 Hz for room temperature and 90 °C (to be discussed later).

The $S(E)$ behavior of poled PLZT 7.5/65/35 at room temperature features a similar frequency dependence as BNT-19BKT-2BZT.[212] Both E_{neg} and $E_{inflection}$ increase with increasing frequency, while S_{max} is virtually frequency-insensitive. This similarity is not surprising since BNT-19BKT-2BZT as well as PLZT 7.5/65/35 are nonergodic relaxors at room temperature that exhibit a field-induced establishment of ferroelectric long-range order. Some of the features observed here are also observed in ordinary ferroelectrics. For example, the increase in coercive field has been reported for barium titanate[234] and soft-doped PZT.[37,235] Beyond that, E_{neg} and $E_{inflection}$ were shown to increase while P_{max} and S_{max} are virtually constant at an electric field amplitude of 2 kV·mm^{-1}.[236] Therefore, it is demonstrated that the lead-free, BNT-based piezoceramic complies to ordinary ferroelectrics in terms of large-signal behavior as soon as the nonergodic relaxor is transformed to a long-range ordered phase. Moreover, the observation that the threshold field is time-dependent is in good agreement with earlier reports about nonergodic relaxors. For example, Colla *et al.*[73] investigated the time-dependent evolution of permittivity in PMN under applied electric field and reported that lower electric fields require more time to induce the FE phase.

This compositional series depicts an evolution from a predominantly nonergodic relaxor (y=0.02) to a predominantly ergodic relaxor (y=0.04). As a consequence of increasing ergodicity, the frequency dispersion in BNT-19BKT-4BZT is observed throughout the whole electric field range up to 6 kV·mm^{-1}, owing to a broad distribution of relaxation times. With increasing y and the accordingly increasing degree of ergodicity, the magnitude of the frequency dependence is likewise enhanced. Meng *et al.*[212] reported on the frequency-dependent strain of PLZT 7.5/65/35 at 100 °C, *i.e.*, in its ergodic state. A frequency-dispersion was likewise observed but not as pronounced as in the present lead-free materials. This difference, however, may be rationalized by the small frequency range, 0.02 Hz to 0.3 Hz, compared to this work, where frequency is varied across four orders of magnitude.

In Figure 4.38 strain is plotted as a function of polarization squared in order to determine the frequency dependence of the electrostrictive coefficient Q_{11}. According to Newnham *et al.*[10], the Q coefficients of crystalline ionic solids exhibit little frequency dependence. It is apparent from

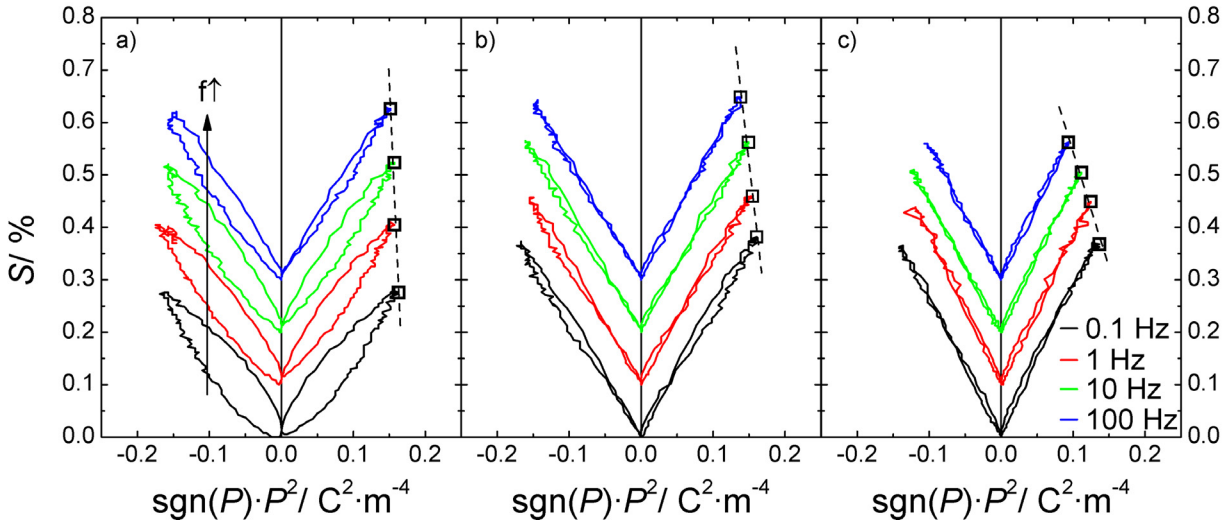

Figure 4.38: Strain as a function of $sgn(P)\cdot(P^2)$ for BNT-19BKT-100yBZT with a) y=0.02, b) y=0.03, and c) y=0.04 at 0.1 Hz, 1 Hz, 10 Hz, and 100 Hz. Note that an offset of $n\cdot 0.1$ % was added instead of S_{rem} because S_{rem} was too small to allow for a clear visibility of all curves.

the $S(P^2)$ curves that Q_{11}, *i.e.*, the slope in the linear sections, indeed varies only slightly. In order to calculate Q_{11} the slope was determined for increasing electric field in the linear section ranging from $P_{max}/2$ to P_{max}. The coefficients are plotted in Figure 4.39 along with the respective uncertainties of the fitting.

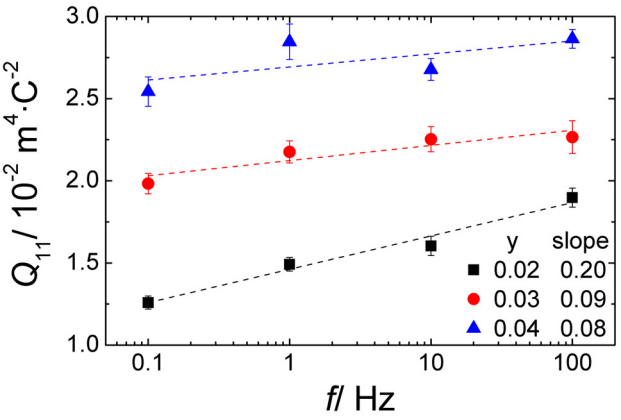

Figure 4.39: Electrostrictive coefficient Q_{11} as a function of frequency for BNT-19BKT-100yBZT with y={0.02; 0.03; 0.04}. The values for the calculated slope have the unit 10^{-2} m^{4}C$^{-2}\cdot$log(Hz)$^{-1}$.

It is apparent that Q_{11} exhibits a small but measurable dependence on frequency as it increases in all three compositions. The variation with frequency is most significant for y=0.02 with a slope of $0.20\cdot10^{-2}$ m^{4}C$^{-2}\cdot$log(Hz)$^{-1}$. It must be noted, however, that BNT-19BKT-2BZT does not obey the electrostrictive relation, *i.e.*, the $S(P^2)$ curves are nonlinear and feature sizable hysteresis. Interestingly, hysteresis decreases with frequency and virtually vanishes for y=0.03 and y=0.04, while Q_{11} increases. Despite the increased Q_{11} value, the achievable maximum strain decreases as

a function of y and frequency because the maximum polarization squared drops disproportionately strong with y and frequency. The frequency and compositional dependence of P^2_{max} is presented in appended Figure A.3.

In summary, the field-induced phase transition depends not only on the applied electric field and the composition but also on frequency. The higher the frequency, the higher the required field is for the transition to take place. This is clear evidence for the time dependence of the transition.

4.4.2 Structural Properties

In previous sections it has been demonstrated how the electromechanical properties evolve as a function of field. In order to rationalize these results it has been hypothesized and discussed that these materials are relaxor ferroelectrics with different degree of ergodicity. The compositional evolution of the field-dependent properties was explained with an increased charge and compositional disorder that are introduced with increasing y, *i.e.*, increasing KNN and BZT content. The comparison with well-known and intensively studied relaxors as PLZT or PMN yielded significant agreement, thus, supporting the relaxor hypothesis. A better understanding of the field-induced behavior, however, requires knowledge about the structure-property relationship. For this reason, the field-dependent *in situ* XRD measurements performed for BNT-20BKT-100yBZT will be discussed in the following in the context of the observed electromechanical properties.

Initial Structure at Zero-Field

The initial crystal structure of the four BNT-20BKT-100yBZT compositions with y={0; 0.02; 0.04; 0.06} is investigated by means of high energy, high intensity X-ray diffraction. Irrespective of BZT content, all four composition are found to exhibit a metrically cubic perovskite structure. The lack of significant non-cubic distortions suggests that the size of the PNRs is notably smaller than the coherence length.

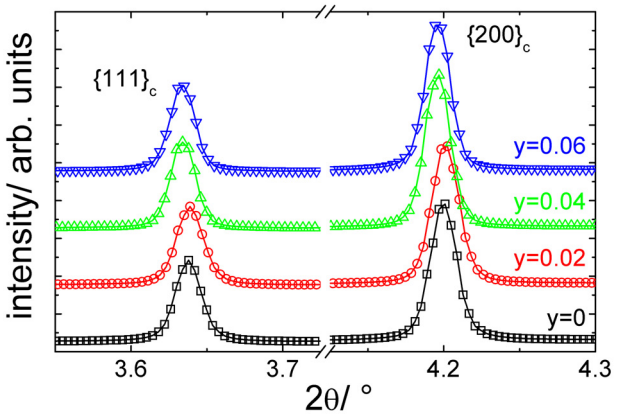

Figure 4.40: $\{111\}_c$ and $\{200\}_c$ reflections at room temperature and zero-field for BNT-20BKT-100yBZT with y={0; 0.02; 0.04; 0.06}.

The structure at zero-field for BNT-20BKT-100yBZT lacks any pronounced non-cubic distortion as shown in Figure 4.40. It is a well-known characteristic that relaxors appear cubic when measured via long coherent probing radiation like X-rays or neutron radiation.[40] For example, PMN has the cubic space group $Pm\bar{3}m$, however, the B-site ions, magnesium and niobium, are distributed randomly and exhibit significant displacements. These displacements give rise to random fields and consequently PNRs.[237] Similar results are reported for other classic relaxors, *e.g.*, PLZT x/65/35 with 8<x<12,[238] $Pb(Fe_{2/3}W_{1/3})O_3$,[239] or $Pb(Fe_{1/2}Ta_{1/2})O_3$.[240] According to Samara,[41] the reason that these systems appear cubic to X-ray and neutron probes down to low temperatures is the small size of the PNRs. Even though the symmetry within the PNRs may substantially deviate from the cubic structure, hardly any non-cubic distortion is observed in the Bragg peaks of the diffraction pattern because the size of the PNRs is lower than the coherence length of the respective diffraction experiments. The coherence length of an X-ray or neutron beam is determined by the wavelength λ, the monochromaticity, the size of the source, and the distance from that source.[241] According to Als-Nielsen and McMorrow,[241] the coherence length of a synchrotron radiation with λ=1 Å is typically on the order of micrometers. For the specific instrument the coherence length is on the order of some 100 nm,[242] which is much larger than the size of PNRs, typically $<$10 nm. For this reason, the apparently pseudocubic structure measured for BNT-20BKT-100yBZT underpins the image derived from the electrical measurement, *i.e.*, polar nano-regions are embedded into a quasi non-polar matrix. The diffraction patterns obtained at room temperature in the course of temperature-dependent high resolution neutron and X-ray diffraction measurements likewise yield a pseudocubic structure for BNT-6BT-100yKNN with y={0.09; 0.12; 0.15; 0.18} and y=0.18, respectively. Both sets of experiments are to be discussed in more detail in Chapter 5.4.

Pseudocubic structures have also been reported for other lead-free BNT-based systems, for example, BNT-BKT-KNN[169] or BNT-ST.[111] Details of the structural properties are still under debate since careful high-resolution studies demonstrated that these pseudocubic materials may actually exhibit minute non-cubic distortions that allow the assignment of a specific non-cubic symmetry. For example, in the case of 92BNT-6BT-2KNN[147] a tetragonal symmetry was found, and BNT-20BKT-2KNN is reportedly a monoclinic and tetragonal phase mixture.[136] For the compositions within the present study the $^1/_2\{311\}_c$ superlattice reflection indicates antiphase oxygen octahedral tilting, which is in agreement with rhombohedral symmetry.[92] The instrument resolution, however, is too low to enable a reasonable Rietveld structure refinement because the instrument in question is optimized for high intensity investigations. Moreover, instead of contemplating Bragg reflections, it was demonstrated recently by different authors that the consideration of diffuse scattering[243] provides a more suitable means to assess the short-range structural correlations in lead-free relaxors, as for example in the case of BNT-4BT[244] or unmodified BNT.[101]

Field-Dependent Structural Evolution

Beyond a threshold electric field a formerly pseudocubic nonergodic relaxor develops significant tetragonal and rhombohedral distortions. This field-induced emergence of a macroscopically polar symmetry represents the merging of PNRs into micro-domains as observed also in lead-based

nonergodic relaxors. Increasing the substitutional disorder inhibits this transition and increases the required threshold field. Eventually, for predominantly ergodic compositions no such transition can be observed.

As demonstrated by Figures 4.26 and 4.27, the application of an electric field induces a reflection broadening in BNT-20BKT and BNT-20BKT-2BZT. This observation agrees with the hypothesis of PNRs growing in size and coalescing into micron-sized domains. It is known from other relaxors that the application of an electric field may induce a transition towards a non-cubic symmetry. For example, in the case of PLZT it was shown by means of XRD that the initial pseudocubic structure becomes orthorhombic with the application of a sufficient electric field.[70] Furthermore, PMN exhibits a field-induced phase transition to a rhombohedral structure[72] with domains of microscopic size.[40]

In the same manner, long-range order is established from PNRs in BNT-20BKT and BNT-20BKT-2BZT under the electric field. Due to the increase in size, these polar regions are now effectively probed by the X-rays giving rise to the aforementioned broadening and asymmetry of the Bragg reflections. These asymmetries suggest that the pseudocubic phase evolves into a tetragonal and rhombohedral phase mixture, *i.e.*, $\{111\}_\mathrm{c}$ splits into the reflection doublet $(111)_\mathrm{r}$ and $(11\overline{1})_\mathrm{r}$ while $\{200\}_\mathrm{c}$ splits into $(002)_\mathrm{t}$ and $(200)_\mathrm{t}$. In order to determine the critical field, the $\{111\}$ and the $\{200\}$ reflection groups are deconvoluted into the respective single reflections using the Voigt function.[245] The resulting lattice spacings are presented in Figure 4.41.

For y=0 the splitting begins at a comparably low electric field of 3.7 kV·mm^{-1} and the resulting splitting at E_{max} is the highest among all four compositions for both reflection doublets. For example, the ratio of $(002)_\mathrm{t}$ over $(200)_\mathrm{t}$ is 1.005, which is equivalent to a tetragonality of 0.5 %. With y=0.02, the splitting begins at a higher field of 4.6 kV·mm^{-1} and the tetragonality of 0.3 % at 6 kV·mm^{-1} is smaller. The derived field values of 3.7 kV·mm^{-1} and 4.6 kV·mm^{-1} depict the field below which no sensible deconvolution could be performed. A comparison with the E_{sat} value determined from the first half-cycle of the $d_{33}(E)$ loop yields good agreement with the XRD measurement. For BNT-20BKT, the same threshold field of 3.7 kV·mm^{-1} is found while the electrical measurement yields 4.0 kV·mm^{-1} for BNT-20BKT-2BZT compared to 4.6 kV·mm^{-1} determined in the *in situ* XRD experiment. This difference is probably connected to the wide step size of 0.46 kV·mm^{-1} used in the diffraction experiment.

It is concluded from the correlation of a peak broadening at E_{sat} that the change in slope in $P(E)$ or $d_{33}(E)$ at that field is most likely associated with the transition to the long-range ordered, macroscopically polar phase.

The established long-range order is also evidenced by the observed domain texture, which is further illustrated by Figure 4.42 for BNT-20BKT. Similar textures are well known from ferroelectrics as PZT, albeit more pronounced.[246] The polar axes of the domains are preferably aligned parallel to the direction of the applied electric field. Consequently, the asymmetries in the reflections are more obvious at low ξ angles, resulting in a decrease in the maximum intensity of the respective reflection groups. It is apparent from Figure 4.42 that the angle dependence is

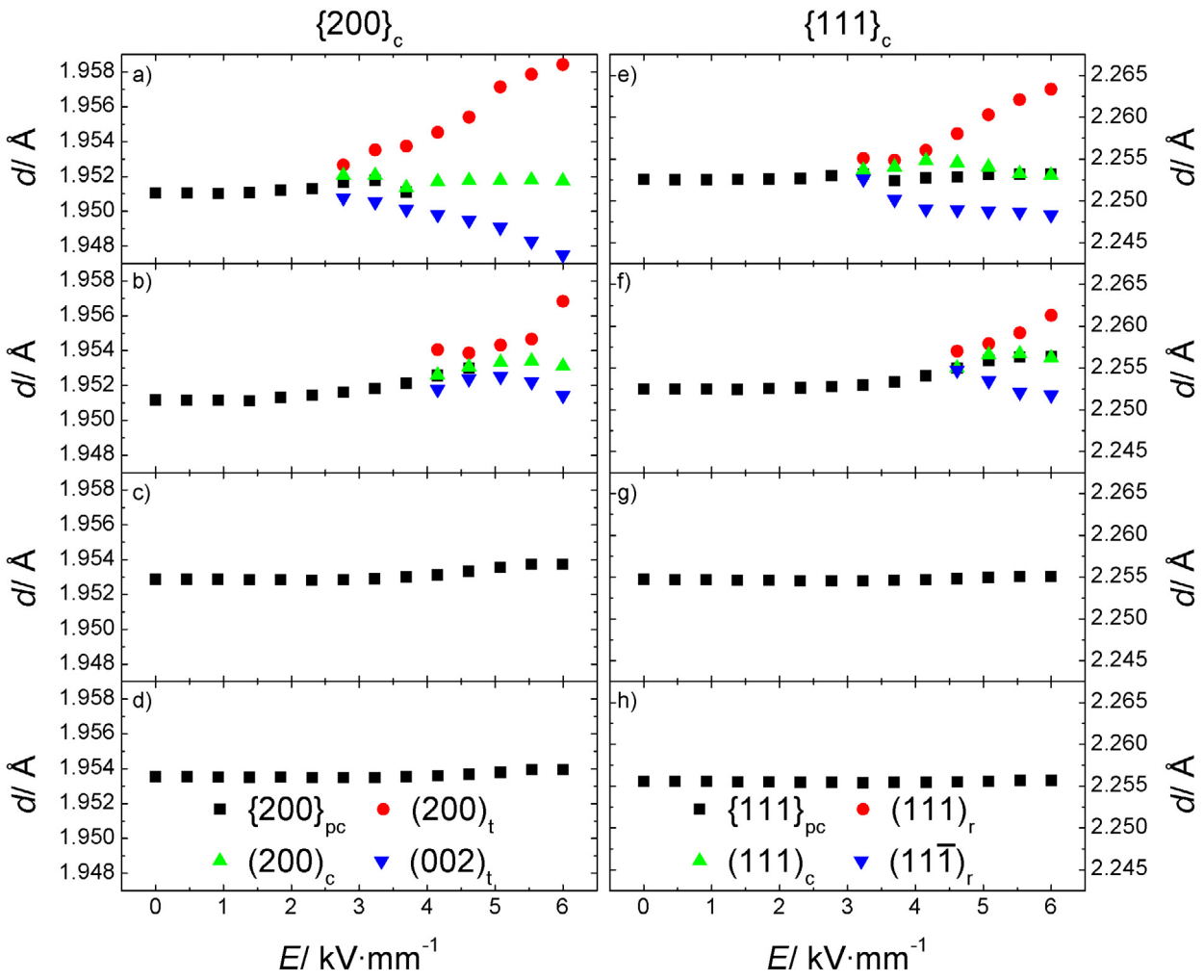

Figure 4.41: Lattice spacing d determined from peak fitting of $\{200\}_c$ (left) and $\{111\}_c$ reflection (right) for BNT-20BKT-100yBZT with a, e) $y = 0$, b, f) $y = 0.02$, c, g) $y = 0.04$, and d, h) $y = 0.06$.

more pronounced for $\{111\}_c$ compared to $\{200\}_c$, indicating that BNT-20BKT is a predominantly rhombohedral.

Finally, no significant splitting occurs for y=0.04 and y=0.06, indicating that the PNRs do not form large domains, thus no threshold field exists within the measured electric field range. This finding is in contrast to *in situ* diffraction measurements reported for 92BNT-6BT-2KNN.[147] The large strain of this incipient piezoceramic was rationalized with a field-induced phase transition from a pseudocubic phase to a polar phase. Upon application of high electric fields, a rhombohedral phase is induced, which vanishes when the electric field is removed. Therefore, this mechanism was suggested to be the physical reason for the large field-induced strain.

In BNT-20BKT-4BZT no such reversible transition is observed and yet large strain is measured under the electric field. It was stated before that E_{sat} in the $P(E)$ curves denotes the transition into a FE phase. Since no E_{sat} can be determined for BNT-20BKT-4BZT, it is plausible that

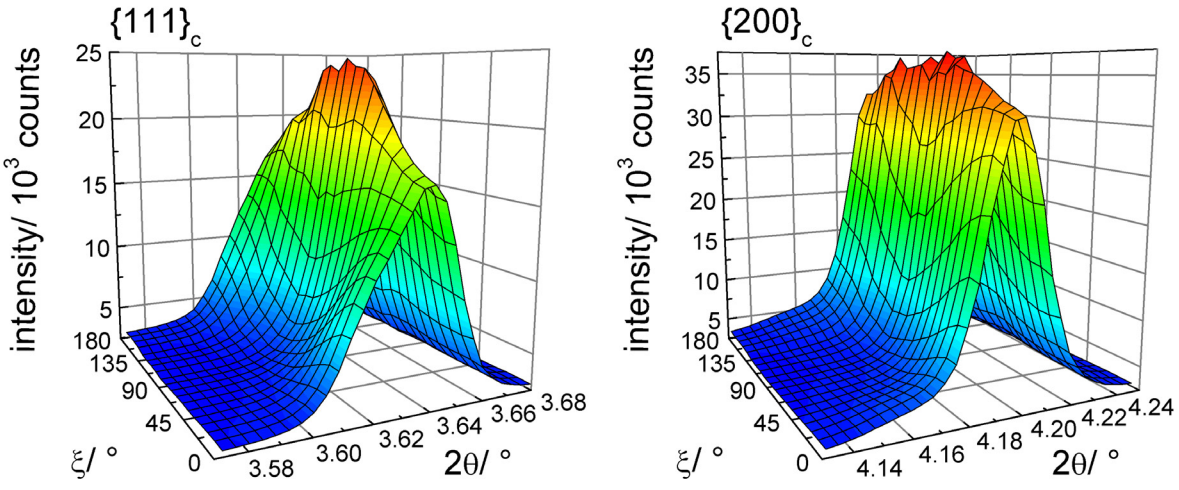

Figure 4.42: Surface plot of the $\{111\}_c$ (left) and the $\{200\}_c$ (right) reflection as a function of the rotational angle ξ for BNT-20BKT at 6 kV·mm^{-1}.

no structural transition is observable in the field-dependent XRD experiment. Close inspection of the $P(E)$ and $S(E)$ curves of both material systems reveals that E_{sat} is always higher than $E_{inflection}$, which is the field where strain sharply increases (Figure 4.37). This finding implies that a high strain occurs even before the structural transition can be observed by XRD. Moreover, strain is found to increase only slowly beyond E_{sat}. Therefore, it is concluded that the high strain is a consequence of the coalescing PNRs, giving rise to both high electrostrictive coefficients and high polarization values. When the FE phase finally emerges, *i.e.*, when the majority of the PNRs is converted to domains, this mechanism is eventually exhausted, causing a decrease in slope of both $P(E)$ and $S(E)$. In BNT-20BKT-4BZT large strain occurs because PNRs grow and coalesce, but the final step of forming a long-range order does not occur. In the XRD experiment, no field-induced transition is observed because PNRs remain comparably small and no micron-sized domains emerge. By contrast, BNT-BT-KNN requires a smaller threshold field as evidenced by the clear bend in the $P(E)$ curve and the consequential field-induced transition.[148] It can only be speculated whether a ferroelectric order may be established in BNT-20BKT-4BZT with higher fields or at lower temperatures. Under the given experimental conditions, no transition occurs.

4.4.3 Domain Structure

The macroscopic polarization and strain of relaxors and ferroelectrics alike is governed by the domain structure and its dynamic response to applied electric fields. Fundamental knowledge about the domains is required to elucidate the field-dependent behavior. Piezoresponse force microscopy (PFM) is the method of choice to study the electromechanical behavior on the nanoscale.

Domain Structure in the Initial State

In the initial state both ergodic and nonergodic compositions are devoid of visible domains owing to the presumably small size of the polar nano-regions. A faint domain-like contrast in BNT-6BT-9KNN and BNT-6BT-18KNN is discussed to likely arise from another yet undisclosed cause.

As presented in Figure 4.29, BNT-6BT-100yKNN materials with y={0; 0.01; 0.03; 0.09; 0.18} do not possess a ferroelectric long-range order in the initial, unbiased state at room temperature. This absence of domains with a size in the micrometer or submicrometer range is evidence that these materials are relaxor ferroelectrics, featuring polar regions of nanoscopic size. In some well-studied relaxors, these PNRs could be imaged by means of piezoresponse force microscopy. The morphology of the PNRs, however, varies notably from system to system. Shvartsman *et al.*[65] reported on labyrinthine, entangled domains in PLZT with a width of approximately 50 nm. PMN-PT, on the other hand, reportedly features nano-domains with a dimension of 1 nm to 100 nm, which are embedded in regular, micrometer-sized domains.[247] The PNRs in PZN-4.5 mol%PT are of irregular shape with a correlation length of 20-100 nm,[248] while $Sr_{0.61-x}Ba_{0.39}Nb_2O_6$:$Ce_x^{3+}$ (SBN:Ce) features fractal-like nano-domains.[249] By contrast, it was found for PMN thin films that the surface does not exhibit piezoelectric activity, provided that an electric threshold bias field is not surpassed.[250] The authors rationalized the absence of a clear domain contrast with the minute size of the polar nano clusters, which was assumed to lie in the range between 5 nm and 10 nm. Therefore, the lack of pronounced domain contrast in Figure 4.29 suggests that for y={0; 0.01; 0.03} the lateral dimensions of the PNRs are below the resolution limit of the PFM. This finding is in agreement with earlier reports that utilized TEM to investigate the microstructure of materials from the BNT-BT-KNN system. Zhang *et al.*[145] observed a homogeneous microstructure, devoid of any distinct grain boundary contrast in BNT-6BT or compositions with little KNN content. This finding was later on confirmed by Schmitt *et al.*[251,252] as they likewise did not observe pronounced micron-sized domains in BNT-6BT and some KNN-modified compositions. They did, however, observe a grainy contrast that was interpreted as a potential indication for polar nano-regions. Kling *et al.*[148] came to the same conclusion for 91BNT-6BT-3KNN in its initial, unbiased state prior to electric field exposure. In BNT-6BT, Ma and Tan[253] found nano-domains coexisting with ferroelectric domains of approximately 100 nm size.

Compared to PFM, the TEM technique is of limited use in investigating the interplay between nanoscopic and macroscopic properties because TEM is restricted to structural and microstructural measurements. Even though PFM provides a variety of means to probe local electrical properties, it has rarely been applied to lead-free materials. Moreover, reports on PFM measurements in lead-free material systems are almost exclusively on thin films or single crystals. Therefore, it is difficult to compare existing reports with the present PFM investigation, which utilizes polished bulk specimens. Tiruvalam *et al.*[254] measured the switching properties of nanoparticulate BNT-10BT thin films and it was found that particles with sizes above 30 nm existed in multidomain configuration while smaller particles existed in single-domain state. Multidomain structures were likewise measured by Cernea *et al.*[255] on sol-gel derived BNT-11BT thin films that exhibited an effective d_{33} of 29 pm·V^{-1}. Yasuda *et al.*[256] discovered ribbon-shaped irregular antiparallel domains along with nanometer-sized domains in BNT-BT single-crystals with 0.33 % Ba on the

A-site. A nanoscale characterization of the bismuth based perovskite BNT was performed by Rémondière *et al.*.[257] They observed domains with a size close to the grain size of approximately 40 nm but also smaller, nanometer-sized domains, which were explained by the lack of long-range ordering of Na^+ and Bi^{3+}. Wang *et al.*[258] revealed that the microstructure of 0.7BNT-0.2BKT-$0.1Bi_{1/2}Li_{1/2}TiO_3$ features a predominantly single-domain structure. Moreover, no lamellar domains were observed which depicts a clear difference to lead-based materials like PZT or PT. By contrast, BNT single crystals reportedly feature ferroelectric domains with a dimension as small as 0.2 µm.[259] Rogers *et al.*[260] reported recently that domains evolve in BNT-5BT thin films upon application of an electric field. It is important to emphasize that findings obtained from thin film investigations may not be generalized to bulk materials. For example, in-plane strain in strontium titanate thin films is well-known to induce ferroelectricity at room temperature even though the bulk material is paraelectric down to 32 K.[261,262] Still, the reported results on the microstructure in BNT-based ceramics appear to confirm the PFM measurements documented within this work as the majority of the authors found indication for the presence of PNRs.

According to Figure 4.29 there is a faint domain-like contrast for y=0.09 and y=0.18. Compared to PZT the contrast is mainly induced from variations in piezoresponse amplitude, while lateral variation of the phase angle is minute (see appended Figure A.4). Ferroelectric domains contradict the respective large-signal measurements, which exhibit little to no hysteresis and, thus, do not provide evidence for a contribution of domains (see Figure 4.10). Moreover, neither neutron nor X-ray diffraction can confirm the presence of domains as demonstrated later (Figure 5.17 and 5.18). Consequently, the observed contrast might be associated with a surface effect. Unlike PFM, the mentioned diffraction techniques probe a bulk volume. Due to the lack of experimental evidence, it is possible to conjecture, but not to definitely clarify, the underlying physical reason for the apparent domain structure. Using PFM, Kalinin *et al.*[263] reported on the existence of static and dynamic domains in the relaxor PMN-0.1PT, even though X-ray diffraction asserted cubic symmetry. In another case, nominally nonpolar strontium titanate yielded piezoelectric contrast.[264] This surface effect was suggested to be the consequence of the flexoelectric effect.[265] Later on, it was shown in theoretical studies that the locally measured electromechanical response of $SrTiO_3$ is affected by a range of different contributions.[266] On the nanoscale, electrochemical reactivity may yield a polarity that is comparable to the electromechanical response and for this reason, a PFM-like signal can in general be obtained despite the lack of ferroelectric domains.[267,268]

Influence of a DC Tip Bias Voltage

Application of a tip bias voltage induces long-range order with strong piezoelectric response. The induced domains are switchable by a reversal of the electric field. Increasing the compositional disorder inhibits the creation of domains and increases the required electric field to the point where no long-range order can be induced anymore.

Figure 4.30 demonstrates that long-range order can be induced on the microscale in BNT-6BT by the application of an electric bias field, *i.e.*, domains form under negative and positive tip bias of $10\,V_{DC}$. Moreover, the inner and outer square exhibit a phase difference of π, *i.e.*, the respective polarization vectors are antiparallel as schematically presented in Figure 4.43.

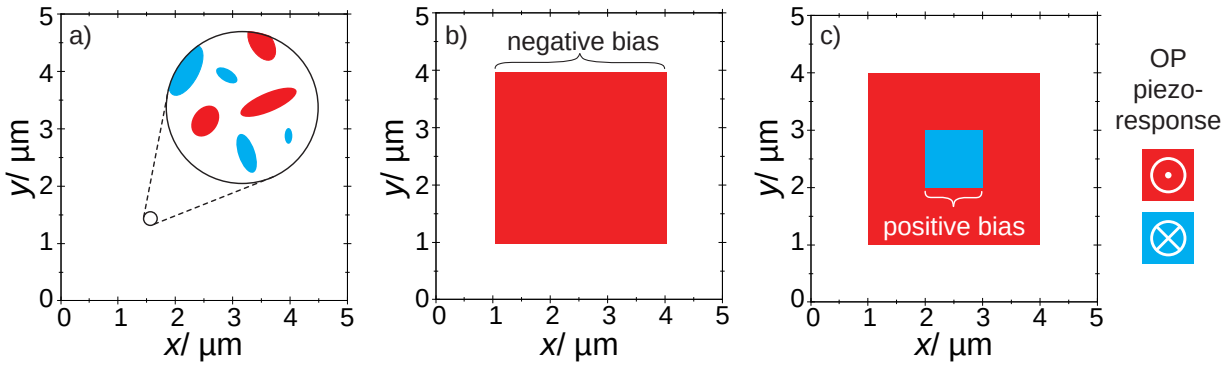

Figure 4.43: Schematic of a) the initial polarization state, b) after application of a negative, and c) a positive tip bias.

As outlined in Chapter 2.1.2, there are two vital elements defining ferroelectricity, namely the existence of a spontaneous polarization and the capability to switch the polarization by an external electric field. More precisely, according to Damjanovic[16], ferroelectricity involves a spontaneous polarization with two equilibrium orientations in the absence of an external field. In particular, it is the spontaneity that gives rise to the debate whether this established long-range order can be referred to as ferroelectric and whether ferroelectricity can actually be induced at all. Although BNT-6BT appears nonpolar on the macroscale, there is a spontaneous polarization within the polar nano-regions, even prior to electric field exposure. The DC bias, however, induces a coalescence and alignment of these PNRs, eventually yielding the formation of micron-sized domains. These domains exist, in agreement with the aforementioned definition, in the absence of an electric field. In addition, it is demonstrated that the polarization vector can be switched by means of an electric field (Figures 4.30 and 4.43). Therefore, it is concluded that the induced long-range order may indeed be ferroelectric in nature.

Macroscopic electrical measurements suggest that small additions of KNN increase the critical threshold field that is required for the creation of long-range order. This observation is reflected also on the microscale as presented by the poling experiment. While 10 V_{DC} suffice for the formation of micron-sized domains in BNT-6BT, higher fields are required for y=0.01 and y=0.03 as evidenced by the dim, incomplete contrast in Figure 4.30. For BNT-6BT-1KNN, the application of 15 V_{DC} (not shown) is sufficient to create a clear box-in-box shape, while a minimum 20 V_{DC} is necessary for BNT-6BT-3KNN. Since no or only little remanence is obtained for the former composition in macroscopic large-signal measurements, it is concluded that the threshold field in these macroscopic measurements is higher than the applied 6 $kV \cdot mm^{-1}$.

Microscopic Switching Loops

Locally measured piezoresponse loops are closed and feature a switchable polarization. Increasing compositional disorder impedes the switching due to enhanced random fields which is reflected in the lateral distribution of the switching voltage U_{sw}.

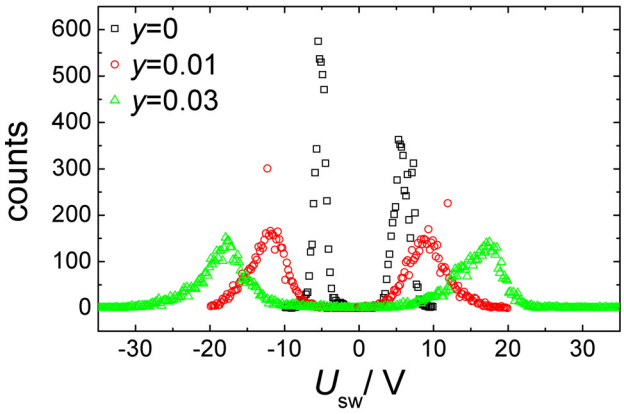

Figure 4.44: Distribution of switching voltages as determined from microscopic piezoresponse loops in a 70x70 grid.

The microscopic piezoresponse hysteresis loops presented in Figure 4.31 provide additional insight into local switching. As outlined above, small additions of KNN increase the threshold field that is required to induce growth of PNRs into micron-sized domains. At the same time, switching is impeded as reflected by the gradually increasing switching voltage, depicted by Figure 4.32. From the measurement of local piezoresponse loops in a dense grid of 70x70 points it is possible to determine the distribution of switching voltages for y={0; 0.01; 0.03} as presented in Figure 4.44. This distribution confirms the finding that the switching voltage increases with KNN-content. Table 4.3 lists the positive and the negative switching voltage $U_{sw,+}$ and $U_{sw,-}$ as calculated by the median of the respective U_{sw} distributions. The averaged switching voltage $\overline{U_{sw}}$ is found to increase notably from 5.5 V_{DC} for y=0 to 10.7 V_{DC} for y=0.01 and 17.1 V_{DC} for y=0.03, respectively. It is apparent that the distribution is broadened with KNN content. In order to quantify this evolution, the full-width at half-maximum (FWHM) was calculated from a peak fit based on the Gaussian model. The base composition BNT-6BT exhibits a small FWHM of 2.2 V_{DC}, increasing to 5.8 V_{DC} in BNT-6BT-1KNN and eventually 7 V_{DC} in BNT-6BT-3KNN. The addition of KNN impedes switching but also broadens the distribution. It is conjectured that the broadness of the U_{sw} distribution may to some extent reflect the variance of the random fields that need to be overcome. The voltage spectroscopy experiments for BNT-6BT-100yKNN with y={0; 0.01; 0.03} were performed on the unbiased sample surface, *i.e.*, without prior treatment with a high DC bias field. Therefore, the observation of closed piezoresponse loops supports the hypothesis that the material is polar on the nanoscale, *i.e.*, PNRs exist although they cannot be imaged for the size is below the resolution limit of the PFM.

Table 4.3: Positive, negative, and averaged switching voltage, calculated from the median of the U_{sw} distribution for BNT-6BT-100yKNN.

y	$U_{sw,+}$/ V_{DC}	$U_{sw,-}$/ V_{DC}	$\overline{U_{sw}}$/ V_{DC}
0	5.7	5.3	5.5
0.01	9.1	12.3	10.7
0.03	16.0	18.2	17.1

It is important to mention that the distribution of U_{sw} and thus also the calculated average value $\overline{U_{sw}}$ as well as the FWHM may be affected by the topography. As the voltage spectroscopy method is not only a highly sophisticated but also time-consuming technique, especially in a dense grid, only one 5x5 µm^2 could be scanned per composition. Therefore, the results obtained from this measurement may not necessarily represent the average behavior of the whole sample surface. The overall trend, however, complies to the results of the voltage spectroscopy in the low-density grids.

Long-Term Relaxation

After poling, random fields may cause a partial or complete relaxation of the piezoresponse. The time-dependent decay can be fit using a stretched exponential function denoting a distribution of relaxation times.

An important factor is the time stability of the induced ferroelectric long-range order. As presented in Figure 4.34, the written domain in BNT-6BT maintains its overall shape and piezoresponse. By contrast, BNT-6BT-1KNN exhibits a partial loss in piezoresponse while the domain in BNT-6BT-3KNN completely vanishes. The averaged piezoresponse of the inner 1x1 µm^2 area is presented for all three compositions as a function of time in Figure 4.45. To compare the stability of the field-induced long-range order, the piezoresponse is normalized to the initial value at t=0 s. To account for tip changes occurring in the process of repeated scanning in BNT-6BT and BNT-6BT-1KNN, the data points for both materials were corrected by adding an offset. The offset was calculated from the peripheral area of the scanned 5x5 µm^2 square, which was not exposed to the electric field and, therefore, is expected to stay constant in piezoresponse. The response of BNT-6BT is demonstrated to slightly increase. This increase, however, cannot be attributed to tip changes since the described correction was applied. Rather, the increase in the signal indicates that the FE phase is apparently stabilized with time. Without further experimental evidence it is not possible to fully clarify the origin for this finding. It can be conjectured that internal fields may alter the strength of the piezoresponse signal. It is known from PZT thin films that internal fields have an influence on the domain stability and, therefore, can increase or decrease the domain size as exemplified by appended Figure A.5. It is also possible that the state of the internal stress has changed with time or repeated scanning. It is well known that the piezoelectric activity may both increase or decrease with stress.[228]

In contrast to BNT-6BT, the piezoresponse in BNT-6BT-3KNN is strongly diminished with time. The induced domain rapidly relaxes back to a domain state that corresponds to the initial situation, *i.e.*, the induced FE phase is not stable as the long-range order vanishes. After 66 min, the average piezoresponse against the background is nearly zero, which suggests that the field-induced transition is reversible. The intermediate composition BNT-6BT-1KNN exhibits a time-dependent decay but it eventually saturates at approximately 50 % of the initial piezoresponse.

The curve progression of the three materials is interpreted as supporting evidence for the coexistence of ergodicity and nonergodicity. BNT-6BT is to a great extent a nonergodic relaxor and for that reason the induced long-range order is stable at room temperature. The increased composi-

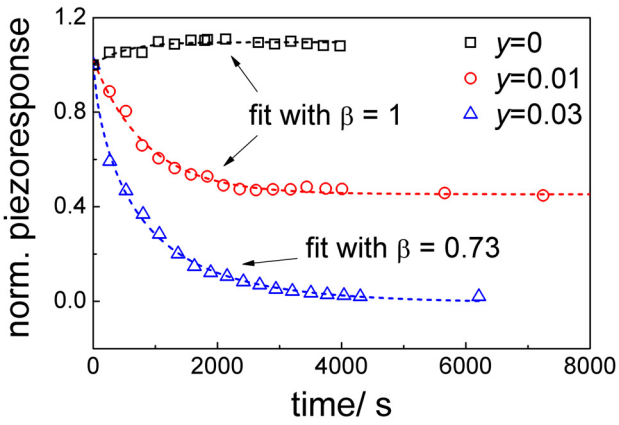

Figure 4.45: Average piezoresponse signal as a function of time for BNT-6BT-100yKNN with y={0; 0.01; 0.03} and respective fit using the stretched exponential function.

tional and charge disorder in BNT-6BT-1KNN results in enhanced random fields. These fields, in turn, increase the ergodic volume fraction and upon removal of the electric field the ferroelectric long-range order collapses in some areas, *i.e.*, the micron-sized domains partially break down into randomly aligned PNRs. As a consequence, the average piezoresponse decreases to a non-zero value. Finally, BNT-6BT-3KNN represents a predominantly ergodic relaxor. For that reason the induced long-range order is not stable and quickly relaxes, causing the piezoresponse to vanish. The PFM signal d_{PFM} presented in Figure 4.45 can be fit to a stretched exponential function according to the following equation.

$$d_{PFM}(t) = y_0 + y_1 \cdot exp(^{-t}/_{\tau})^{\beta} \tag{4.7}$$

In this formula the fitting parameter y_0 describes an offset and y_1 describes an increase or decrease in the PFM signal. Moreover, τ is the relaxation time and β is the stretching exponent. This function, also referred to as Kohlrausch-Williams-Watt function, was initially used to describe the discharging of a capacitor[269] but can describe other relaxation processes in disordered systems.[270,271,272] It is also a commonly accepted function to fit relaxation processes in ferroelectrics, *e.g.*, in retention experiments on PZT thin films,[273] observation of domain nucleation and growth via PFM,[274], and the switching kinetics of fatigued ($Pb_{0.99}[Zr_{0.45}Ti_{0.47}(Ni_{0.33}Sb_{0.67})_{0.08}]O_3$).[275]

The fitting parameters obtained for BNT-6BT-100yKNN are provided by Table 4.4. The parameter y_0 represents the behavior described above, *i.e.*, the time-dependent increase in the response of BNT-6BT, the decay by approximately one half for BNT-6BT-1KNN, and the vanishing of response for BNT-6BT-3KNN. The stretching exponent is unity for BNT-6BT and BNT-6BT-1KNN, *i.e.*, piezoresponse obeys a single exponential decay. In contrast, BNT-6BT-3KNN is best fit with β is 0.73, signifying that the switching kinetics cannot be described with a singular time constant. A stretched exponential behavior had also been found for other relaxor ferroelectrics. For the ergodic relaxor PMN-0.1PT, the stretching exponent was determined as β=0.4 by means of microscopic relaxation experiments.[263] While the observed relaxation is ascribed to the relaxation of dynamic PNRs, the authors also stated the existence of static PNRs, *i.e.*, frozen spatial fluctuations of polarization. For the BNT-6BT-100yKNN material system it is assumed that non-

Table 4.4: Parameters y_0, y_1, β, and τ with the respective uncertainty calculated for BNT-6BT-100yKNN with y={0; 0.01; 0.03} using the stretched exponential function.

parameter	y=0	y=0.01	y=0.03
y_0	1.1	0.46	0
y_1	-0.1	0.55	1
β	1	1	0.73
$\Delta\beta$	0.45	0.1	0.03
τ/ s	491	872	742
$\Delta\tau$/ s	153	63	31

ergodic and ergodic volume fractions may also coexist in a similar manner. It was also concluded from theoretical calculations that a non-Debye relaxation results from a random field distribution. Moreover, β is stated to depend on the concentration of random field sources like electric dipoles.[276] As discussed, the increase in piezoresponse of BNT-6BT is likely to be influenced by some additional, unidentifiable effect and, therefore, the fit might not be as robust as for y=0.01 or y=0.03, indicated by the sizable uncertainty in β and τ.

For BNT-6BT-1KNN the induced FE phase is stable after an initial relaxation with a computed τ=872 s. A similar temporal evolution of piezoresponse has been reported for the uniaxial relaxor SBN:Ce.[249] After approximately 4x10^4 s the signal was found to saturate at approximately 65 % of the initial value. Moreover, the authors found that the stretched exponential function could fit this relaxation with τ=16340 s and β=0.45. The remanent signal is rationalized with a relaxation into a quasistatic domain as a consequence of backswitching on the microscale. The time-dependent decay of the signal in Figure 4.45 suggests a similar process in BNT-6BT-1KNN. It is most important to keep in mind that the induced long-range order does not permeate the whole sample thickness because the field strength decreases with distance to the tip.[277] Therefore, the effective electric field meets the required threshold only in a surface-near sample volume. In SBN:Ce the backswitching occurs mainly at the interface between the unbiased relaxor and the induced superficial domain, suggesting two potential microscopic mechanisms:[249] Either, stray fields due to the induced domain may give rise to depolarization, or nano-domains may form as a result of random fields. In contrast to SBN:Ce, the relaxation in BNT-6BT-1KNN does not take place by means of a strong contraction of the domain. As depicted by the phase angle for BNT-6BT-1KNN in Figure 4.46, the area of the induced long-range order is largely invariant. Minute changes in the domain morphology are observed only at the outermost border of the domain. The amplitude, however, notably decreases and consequently the piezoresponse decays likewise as demonstrated by the piezoresponse profile presented in Figure 4.47 a).

This mechanism of polarization decay is in contrast to the time-dependent relaxation behavior observed in ferroelectrics. For example, in PZT thin films the relaxation takes place via nucleation and growth of domains of converse polarization, which preferentially occur at the domain boundary.[274] By contrast, the decay in piezoresponse for PLZT 9.5/65/35 was reported to exhibit a similar behavior like BNT-6BT-1KNN, *i.e.*, an almost uniform decrease of polarization

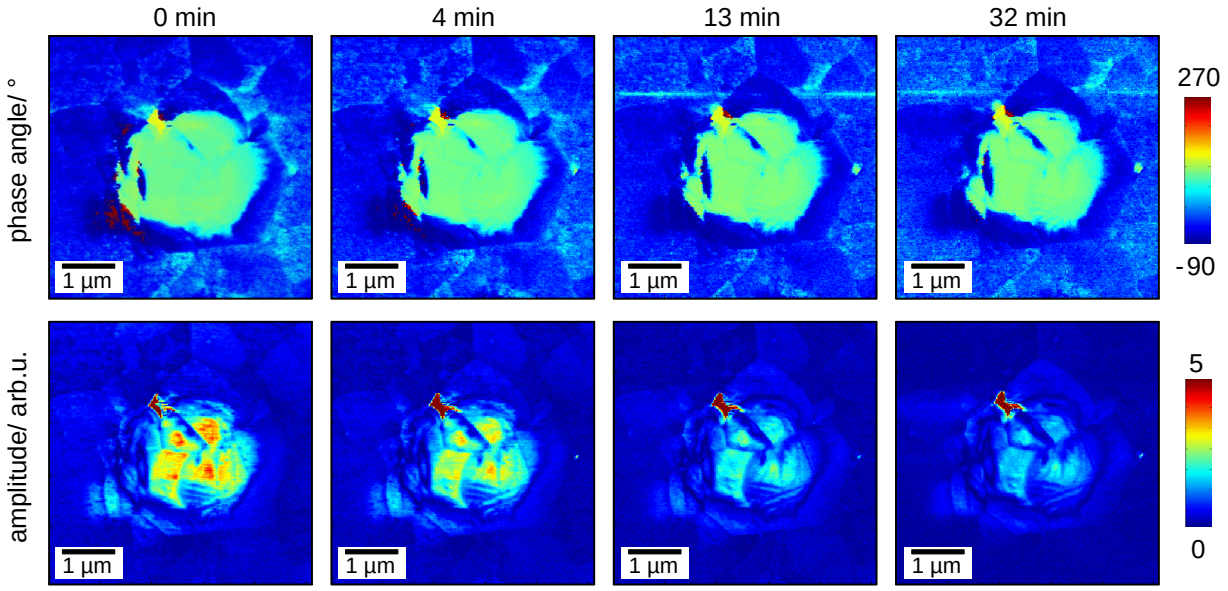

Figure 4.46: Maps of the phase angle and amplitude for the piezoresponse measured on BNT-6BT-1KNN directly after poling and after a period of 4 min, 13 min, and 32 min. Note that green areas in the phase angle maps (top row) correspond to approximately 90 ° while blue areas correspond to approximately -90 °.

instead of a lateral contraction.[77] The authors describe the relaxation process with a 'fading' of the domain, contrasting the mechanism observed in ferroelectrics that is based upon domain wall motion. Furthermore, the time-dependent evolution of the piezoresponse in PLZT reportedly follows a stretched exponential function with β=0.3 and τ=750 s. According to Figure 4.47 both BNT-6BT-1KNN and BNT-6BT-3KNN feature the same 'fading' as PLZT, suggesting that the underlying physical mechanism in BNT-based relaxors is similar to that exhibited by PLZT. Details of this mechanism, however, are not known and thus it can only be conjectured that the domains consecutively break up into PNRs. Due to the small size, these PNRs cannot be imaged in the piezoresponse maps. The increased occurrence of PNRs within the scanned area will eventually cause a decay in the measured signal. Keep in mind that each map in Figure 4.34 spans 5x5 µm^2 with a grid of 256x265 points and, therefore, each point equals an area of 20x20 nm^2, while the PNRs have a size below the resolution limit of the PFM, which is notably smaller than 10 nm. The observed signal per point is therefore the integrated superposition of the contribution from both the induced domain and randomly oriented PNRs. Therefore, it is apparent that PNRs, even though not imaged, may cause a decay in measured polarization.

These findings from the microscopic long-term measurement comply surprisingly well to the macroscopic large-signal measurements. The drop in remanence, which eventually gives rise to the large strain, is qualitatively reflected in the time-dependent decay of piezoresponse. In BNT-6BT, the induced long-range order is stable but diminished with increasing KNN content, *i.e.*, increasing disorder. The establishment and collapse of long-range order as evidenced by macroscopic double-loop polarization hystereses is observed on a time-scale of a few seconds. In the

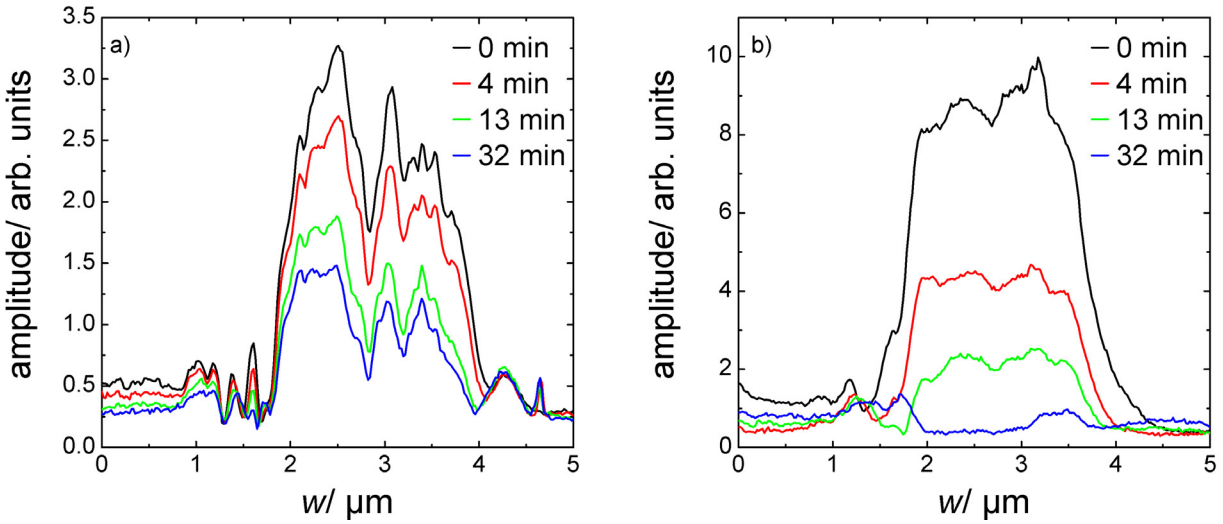

Figure 4.47: Profiles of the PFM-amplitude for a) BNT-6BT-1KNN and b) BNT-6BT-3KNN directly after poling and after a period of 4 min, 13 min, and 32 min, determined from a 5x0.4 µm^2 image section across the poled area.

PFM experiment, on the other hand, a relaxation time of τ=742 s was found for BNT-6BT-3KNN. It is important to note that the experimental results obtained from PFM must not be translated directly to the bulk specimen measurements. The elastic and electrical boundary conditions are notably different in both types of experiments. In the PFM experiment, only a very small portion of the sample is exposed to a locally very high electric field, owing to the fine-scaled tip geometry and poling is performed in a continuous manner by scanning the respective area. By contrast, the whole specimen is exposed to a smaller yet more homogeneous electric field in the macroscopic measurement. Moreover, PFM probes the surface and it is well known that the properties of surfaces may be inherently different from bulk properties. In a comparable PFM study by Kholkin *et al.*[77] a relaxation time τ=750 s was found for PLZT 9.5/65/35 while macroscopic $P(E)$ loops clearly ascertain the pronounced ergodicity.[278]

Areal Effect of Field Application

The bias-induced area is larger than the actually scanned square. Two hypothesis are discussed: electric stray fields and the extension of ferroelectric order from long-range ordered seeds.

The application of an electric field to the sample surface results in the creation of a micron-sized domain with enhanced piezoresponse compared to the initial unbiased state. The area of this induced domain, however, is considerably larger than the area that was scanned with the tip DC bias voltage. In order to investigate this peculiar effect, differently sized sections were scanned in BNT-6BT with -20 V_{DC} tip bias voltage and a scan frequency of 1 Hz, while edge length ranged from 0 µm (tip in punctual contact for <1 s) to 0.5 µm, 1 µm, 2 µm, and 4 µm. In Figure 4.48 the width of the additionally biased border area is plotted against the scanned area.

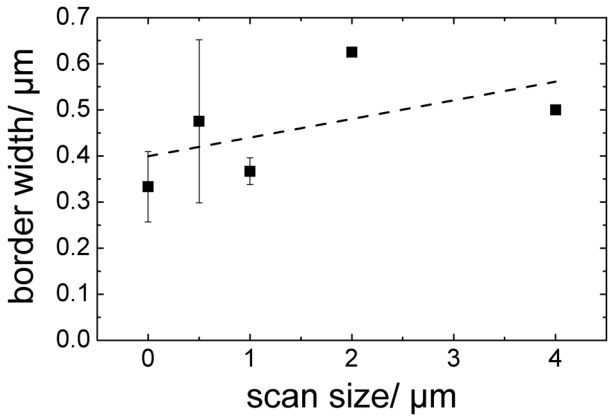

Figure 4.48: Width of additionally biased border area as a function of scan size.

It was found that the width of the induced border area is largely independent of the scan size, *e.g.*, applying a DC voltage to a square of 0.5 µm yields a border of 0.48 µm while scanning 4 µm yields 0.5 µm. Two potential explanations will be briefly discussed. First, it is hypothesized that the field from the tip is strongly inhomogeneous and that the fields extend far beyond the tip. These 'stray fields' could potentially affect the area surrounding the scanned square of 1x1 µm^2, eventually resulting in a larger domain than initially intended. Numerical simulations from Alexander Tselev[279] indicate that the electric field is highly focused and narrow. There is indeed a stray field, but the effect is limited to a few tens of nanometers, as demonstrated by Figure 4.49. Therefore, the additional border width cannot be explained merely by electric stray fields. A color-coded two-dimensional plot of the calculated electric field distribution is provided in the Appendix by Figure A.6. Moreover, in an equivalent measurement on soft PZT, the switched domain is likewise larger than the scanned area but the additional border is only approximately 0.2 µm wide (see Figure A.2) compared to approximately 0.5 µm in the lead-free piezoceramics. Therefore the observed effect is more likely to be related to the material properties rather than the experimental setup.

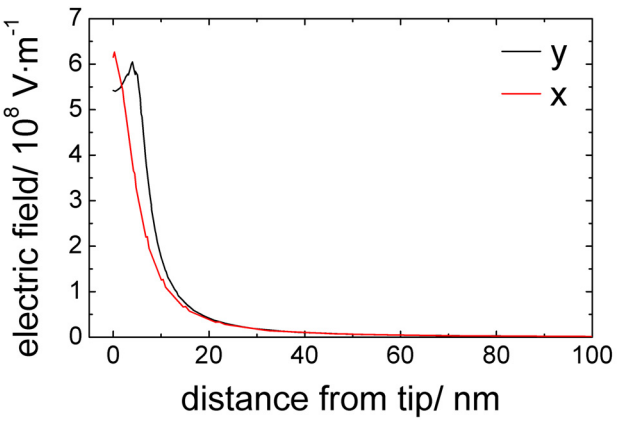

Figure 4.49: Electric field strength as a function of distance from the PFM tip in both the in-plane (y) as well as the out-of plane (x) direction (courtesy of Alexander Tselev, ORNL).

A second hypothesis is that the area beneath the tip, which is directly exposed to the electric field, acts as a nucleus. At first, the polarization is only aligned according to the applied electric field in the immediate sample volume under the tip. Subsequently, the domain grows into the adjacent pseudocubic but easily polarizable volume. A similar mechanism has been recently proposed for $CaZrO_3$-modifed $(K_{0.51}Na_{0.47}Li_{0.02})(Nb_{0.8}Ta_{0.2})O_3$ (KNLNT-CZ), which exhibits a so-called core-shell microstructure.[280] The long-range ordered cores act as 'seeds' and under the influence of an electric field the long-range order is extended into the surrounding, nominally nonpolar shell-volume. In order to verify this hypothesis further experimental effort is required, for example, time-dependent measurements in order to investigate the involved kinetics.

4.5 Summary

Measurements at high electric fields demonstrate that both material systems, BNT-6BT-100yKNN and BNT-100xBKT-100yBZT, are to a great extent equivalent. This finding suggests that, despite different chemistry, the underlying mechanism for large strain is essentially identical and can be discussed simultaneously. This also strongly indicates that other material systems, which utilize the same phenomena, might be found in the future.

The investigated BNT-based materials are relaxor ferroelectrics rather than conventional ferroelectrics. Therefore, they consist of polar nano-regions embedded into a metrically cubic matrix. From BNT-6BT-100yKNN it is found that the composition greatly affects the electromechanical large-signal properties through internal quenched random fields, which are in turn governed by lattice and charge disorder. *In situ* diffraction measurements show that the average structure is initially pseudocubic. Beyond a critical threshold field a transition into a clearly non-cubic phase or phase mixture occurs, thereby developing a domain texture. In addition, PFM measurements demonstrate that not only the ability to induce this transition depends on the composition but also the time stability of the induced phase is strongly affected by the composition.

The suggested different field-dependent evolution of the polar regions and domains is illustrated in Figure 4.50. In the initial state (E_0=0) small PNRs are dispersed in a pseudocubic phase. In nonergodic materials (A) like BNT-6BT or BNT-20BKT these PNRs are correlated. The application of an electric field gives rise to coalescence and growth (E_1). Eventually, a sufficiently high electric field E_2>E_{th} induces a long-range order with micron-sized domains, which are stable even after removal of the electric field. This state can hardly be distinguished from conventional ferroelectrics with respect to functional and structural properties. Ergodic relaxors like BNT-6BT-3KNN (B) show a very similar behavior for small electric fields (E_1), that is, PNRs grow in size. At high electric fields (E_2>E_{th}) ergodic relaxors may also possess micron-sized domains and high piezoelectric constants. In contrast to nonergodic relaxors, however, these domains are fragmented again into PNRs upon removal of the field, resulting in low remanent polarization and strain. As a consequence, the piezoelectric coefficient d_{33} is small but the repeatedly producible strain is large. This mechanism of coalescence and collapse of PNRs naturally entails a pronounced frequency dependence due to the involved kinetics. In likewise ergodic BNT-20BKT-4BZT (C), the required

E_{th} is higher than for BNT-6BT-3KNN, thus, no domains are established at the same electric field E_2 as evidenced by *in situ* XRD. The field-driven coalescence of PNRs, however, gives rise to both large electrostrictive coefficients and high polarization values yielding large attainable strains.

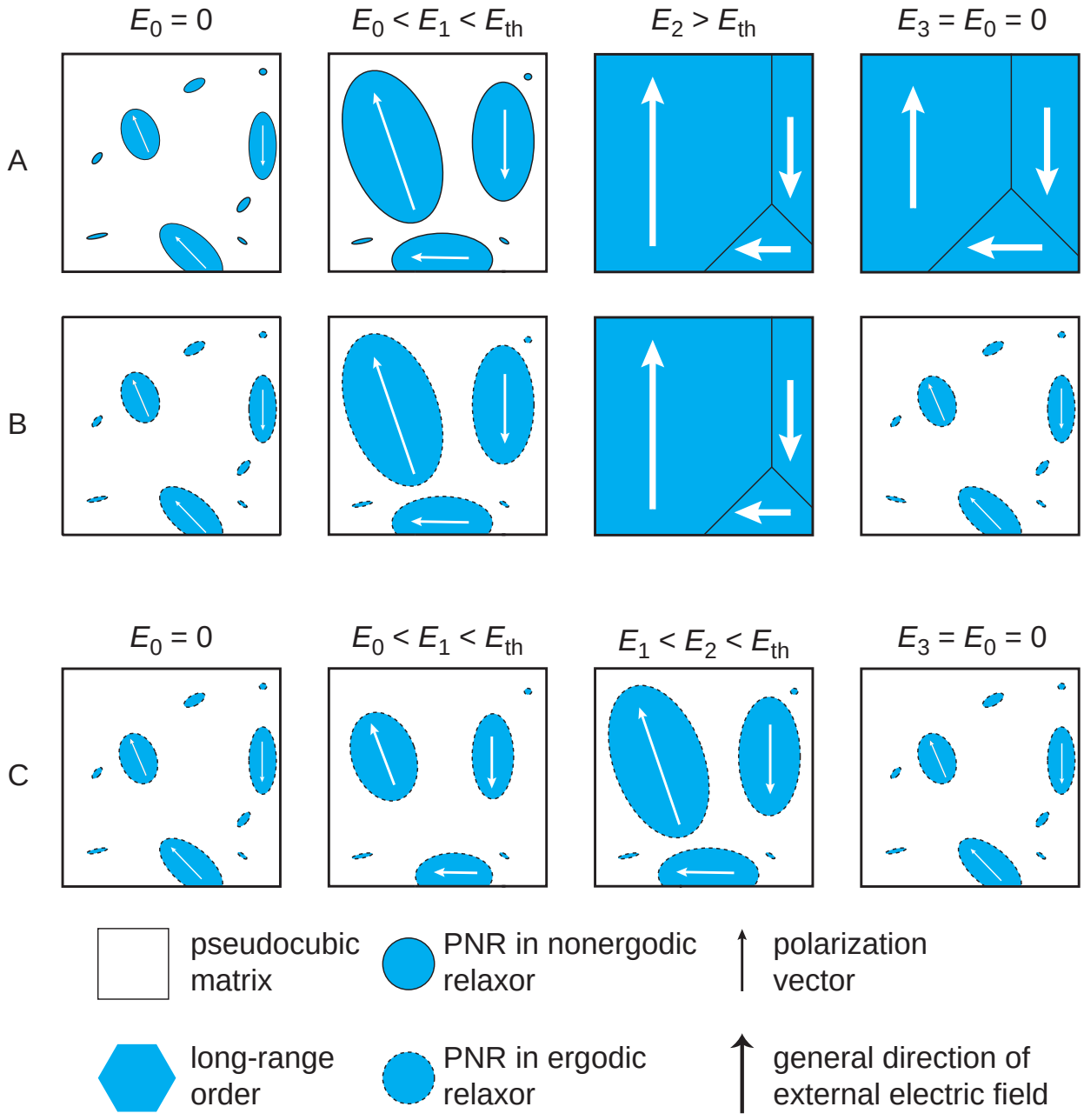

Figure 4.50: Simplified schematic on the proposed evolution of polar regions as a function of electric field in A) nonergodic BNT-6BT, B) ergodic BNT-6BT-3KNN, and C) ergodic BNT-20BKT-4BZT.